

NICMOS Kernel-Phase Interferometry I:  
Catalogue of Brown Dwarfs Observed in F110W and F170M

SAMUEL M. FACTOR<sup>1</sup> AND ADAM L. KRAUS<sup>1</sup>

<sup>1</sup>*Department of Astronomy, The University of Texas at Austin, Austin, TX 78712, USA*

ABSTRACT

Filling out the dearth of detections between direct imaging and radial velocity surveys will test theories of planet formation and (sub)stellar binarity across the full range of semi-major axes, connecting formation of close to wide separation gas giants and substellar companions. Direct detection of close-in companions is notoriously difficult: coronagraphs and point spread function (PSF) subtraction techniques fail near the  $\lambda/D$  diffraction limit. We present a new faint companion detection pipeline called Argus which analyzes kernel phases, an interferometric observable analogous to closure phases from non-redundant aperture masking but utilizing the full unobscured telescope aperture. We demonstrate the pipeline, and the power of interferometry, by performing a companion search on the entire *HST/NICMOS* F110W and F170M image archive of 114 nearby brown dwarfs (observed in 7 different programs). Our pipeline is able to detect companions down to flux ratios of  $\sim 10^2$  at half the classical diffraction limit. We discover no new companions but recover and refine astrometry of 19 previous imaging companions (two with multiple epochs) and confirm two previous kernel-phase detections. We discuss the limitations of this technique with respect to non-detections of previously confirmed or proposed companions. We present contrast curves to enable population studies to leverage non-detections and to demonstrate the strength of this technique at separations inaccessible to classical imaging techniques. The binary fraction of our sample ( $\epsilon_b = 14.4_{-3.0}^{+4.7}\%$ ) is consistent with previous binary surveys, even with sensitivity to much tighter separation companions.

1. INTRODUCTION

The detection of companions to stars—both planets and stellar binaries—has traditionally relied on three methods: radial velocities (RVs), transits/eclipses, and direct imaging. Transits and RVs are both limited in their sensitivity to companions at large semimajor axes; transits are increasingly improbable for companions that are distant from their host star, and RV surveys must extend for at least one orbital period before a detection can be confirmed. In contrast, direct-imaging surveys are more sensitive to objects at larger distances from their host star, and hence they offer a singular view into outer solar systems and the peak of the binary semimajor-axis distribution. However, there is often a gap between these two regimes, inside the inner working angle of direct imaging and outside

the regime where transits and RVs can efficiently survey. Filling this gap would offer a crucial new view of both planet formation/evolution and stellar multiplicity.

Binary systems pose stringent tests for models of star and brown dwarf formation, as binaries are a common outcome. A successful formation theory should replicate the observed frequency, semimajor axis distribution, and mass function (e.g. [Duchêne & Kraus 2013](#)) as well as the detailed orbital parameters ([Dupuy & Liu 2011](#)), all as a function of system mass. The semimajor axis distribution can provide insight into the size/density evolution of the originating prestellar core, while the companion mass function results from the accretion history. However, it is unclear if the peak of the semimajor axis distribution of brown dwarf binaries has even been resolved (e.g. [Burgasser et al. 2006b](#)), particularly among populations of newly forming binaries with known formation environments (e.g. [Kraus & Ireland 2012](#)). Spectral synthesis might indicate that a significant number of binaries remain unresolved ([Bardalez Gagliuffi et al. 2015](#)), an assertion that could be tested with observations at higher spatial resolution.

While the use of coronagraphs and PSF subtraction techniques can improve detection limits, these techniques still do not achieve sufficient resolution. Imperfections in the optical path (and AO correction for ground based telescopes) introduce “speckles” which can be misinterpreted as companions. These speckles can be corrected based on temporal or chromatic behavior (i.e. ADI, SDI, and LOCI) at large angular separations, but those methods fail near  $\lambda/D$ . Interferometric analysis takes advantage of the wave nature of light and can be used to produce a more stable and calibrated PSF, reject speckle noise and detect companions with high contrast at or even below the diffraction limit. Rather than subtracting off the PSF, these techniques use the information contained in it to infer the geometry of the source. The discovery of the candidate newly forming giant planet LkCa15b by [Kraus & Hillenbrand \(2012\)](#); [Sallum et al. \(2015\)](#) demonstrates the power of such techniques.

The most common interferometric analysis technique for single-aperture telescopes, non-redundant aperture masking interferometry (NRM or AMI; [Tuthill et al. 2006](#); [Tuthill 2012](#)), places a mask in the pupil plane, transforming a large single aperture into a sparse interferometer. Such a configuration produces an interferogram, or 2-D fringe pattern, which contains information about phase, in addition to intensity. Rather than simply looking for a companion in the image, an observable called a closure-phase is used to compare to a model image. Closure-phases are independent of the path length errors which cause speckles and thus contain true source phase information. NRM has been used for numerous applications in binary demographics and orbital analyses ([Ireland et al. 2008](#); [Kraus et al. 2008](#); [Dupuy & Liu 2017](#)) and substellar/planetary companion discovery ([Lloyd et al. 2006](#); [Kraus & Hillenbrand 2012](#); [Sallum et al. 2015](#)).

A similar observable can be used with a full, rather than a masked, aperture. This technique models the full aperture as a grid of small apertures corresponding to a redundant set of baselines. Using simple linear algebra outlined below, [Martinache \(2010\)](#) derived an operator which, when applied to the sampled phases, produces observables called kernel phases which are again independent of phase errors in each baseline. Diffraction limited observations are required, either from space or using ground based AO systems, as the phase errors *must* be small in order to properly account for the redundancies in the baselines.

While both methods are powerful tools for super-resolution imaging, NRM faces an observational limit. Since NRM uses a sparse mask, only  $\sim 5\%$  of the light reaches the detector, imposing a flux limit on possible targets. Kernel-phase interferometry (KPI), on the other hand, utilizes the full

telescope aperture. Thus it can achieve similar detection limits in a fraction of the time and can be applied to dimmer sources where NRM is not feasible. As no specialized mask is required, KPI can also be performed on archival data as long as the diffraction pattern is properly sampled. This allows the characterization of a companion’s orbit using standard astrometric comparison of archival and current data.

This technique has been applied only a few times (relative to classical imaging techniques) since the original publication by [Martinache \(2010\)](#). [Pope et al. \(2016\)](#), [Kammerer et al. \(2019\)](#), [Wallace et al. \(2020\)](#), and [Kammerer et al. \(2021\)](#) all analyzed ground based AO imaging datasets (from Palomar/PHARO, VLT/NACO, Keck/NIRC2 and VLT/VISIR-NEAR, respectively) while [Laugier et al. \(2019\)](#) focused on recovering information from saturated *HST/NICMOS* camera 2 images. Analysis by [Pope et al. \(2013\)](#) of *HST/NICMOS* camera 1 images of brown dwarfs from [Reid et al. \(2006, 2008a\)](#) proposed five new candidate companions (and four marginal detections) and recovered all previously known companions. Clearly the technique is underutilized and merits further exploration.

This work analyzes the same two NICMOS data sets as [Pope et al. \(2013\)](#) as well as 5 more sets of archival observations. We introduce a new KPI pipeline named Argus<sup>1</sup> ([Factor 2022](#)) with a careful treatment of phase errors, calibration, model comparison, and detection limits. We recover 19 observations of 17 previously known companions, including one of the new binaries found by [Pope et al. \(2013\)](#) (as well as one more which we marginally recover). We do not confirm any of their marginal detections. We present refined astrometry and photometry for the detected companions and discuss the resulting binary statistics. All sources which we do not recover can be explained by KPI’s insensitivity to wide companions or low SNR imaging.

This work is laid out as follows. Section 2 outlines the instrument and archival observations analyzed in this work. Section 3 details the kernel-phase technique and our new pipeline. Section 4 presents the results of our companion search with discussions of detections and non-detections. In section 5 we discuss the binary fraction of our sample, and put our KPI analysis in context. In Section 6 we summarize our conclusions.

## 2. OBSERVATIONS

### 2.1. NICMOS Data

In this work we reanalyze archival *HST* observations using the Near Infrared Camera and Multi-Object Spectrometer (NICMOS). NICMOS was installed during servicing mission 2 and operated between 1997 and 1999 (Cycle 7 and 7N) when its solid nitrogen coolant ran out. It was restored to service during servicing mission 3B with a replacement cooling system and operated again from 2002 to 2008 (Cycle 11–16). All data sets analyzed in this work were taken during the second block.

NICMOS operates between 0.8 and  $2.5\mu\text{m}$ . This work uses the F110W and F170M filters corresponding to a diffraction limited resolution resolution ( $\lambda/D$ ) of 95 mas and 147 mas, respectively. Thus the 43 mas pixels of NIC1 sample the PSF at 2.2 and 3.4 pixels per resolution element, respectively. The detector is  $256 \times 256$  pixels for a field of view of  $11'' \times 11''$ . The X/Y pixel scale ratio for NIC1 is 1.0030 ( $\sim 0.1$  mas larger in the X direction). Since we only perform astrometry on the scale of a few pixels, we treat them as square.

<sup>1</sup> The open source python pipeline is available on GitHub: <https://github.com/smfactor/Argus>.

**Table 1.** Observations

Prog. ID	P.I.	Cycle	$N_{obj}$	Filters (in addition to F110W, F170M)	$N_{dithers}$	approx. epoch	Publication
9704	Schultz (2002)	11	1	F180M, F222M	0	12/2002	Roye et al. (2003)
9833	Burgasser (2003)	12	22	F090M	3–6	9/2003–7/2004	Burgasser et al. (2006b)
9843	Gizis (2003)	12	2	F110M, F145M, F170W	2	9–11/2003	Burgasser et al. (2011)
10143	Reid (2004)	13	56		2	9/2004–6/2006	Reid et al. (2006)
10247	Cruz (2004)	13	1	F090M, F145M, F160W	4	9/2004	Burgasser et al. (2006b)
10879	Reid (2006)	15	28		2	7/2006–5/2007	Reid et al. (2008a)
11136	Liu (2007)	16	7	F090M, F108N, F110M, F113N, F145M, F160W	3–7	5–8/2008	Dupuy et al. (2010)

NICMOS contains cold masks which block the thermal emission from the primary mirror edge and telescope spiders. This results in an effective primary mirror diameter of 2.388 m, secondary mirror occultation diameter of 0.8928 m, and a spider arm width of 0.1848 m (dimensions taken from TinyTim; Krist et al. 2011). Due to thermal stress on the NICMOS dewar the cold masks are slightly shifted (Krist & Hook 1997). Previous KPI analyses of *HST/NICMOS* data (e.g. Martinache 2010; Pope et al. 2013) do not implement this shift and we do not as well. Calibration should remove most additional phase noise introduced by the imperfect model, though in the future we could use a gray aperture or characterize the aperture more accurately with a much higher resolution model (e.g. Martinache et al. 2020).

## 2.2. Target Sample

In this work we analyze the data sets listed in Table 1. These are all the high resolution (NIC1) brown dwarf imaging programs utilizing the F110W and F170M filters. These filters are the two most commonly used filters for imaging of brown dwarfs, roughly corresponding to the *J* and *H* bands. Observing set-ups differ between programs but generally consist of two or more dithered exposures in each filter.

Table 2 details the properties of the targets analyzed in this work. The sample covers spectral types from late M to T dwarfs at distances ranging from  $\sim 5$ –35 pc. Programs 9833, 10143, and 10879 were general imaging surveys of nearby brown dwarfs while programs 9843, 10247, and 11136 specifically targeted known binary systems. Program 9704 observed a PSF calibrator (spectral type M4V) in F170M to characterize the cold-mask shift and is included since it is a pristine and high SNR PSF. Program 11136 specifically prioritized wavelength coverage in a large number of filters over deep, high SNR, observations.

**Table 2.** Target information

2MASSJ	SpT (ref.)	Parallax [mas] (ref.)	J [mag] (ref.)	H [mag] (ref.)	HST program
2MASS J00043484-4044058	L5+L5 (7)	$82.1 \pm 0.4^{(2)}$	$13.109 \pm 0.024^{(1)}$	$12.055 \pm 0.026^{(1)}$	10143
2MASS J00242463-0158201	M9.5V (31)	$79.97 \pm 0.22^{(2)}$	$11.992 \pm 0.035^{(1)}$	$11.084 \pm 0.022^{(1)}$	10879
2MASS J00250365+4759191	L4: (20)	$23.7 \pm 1.1^{(4)}$	$14.84 \pm 0.04^{(1)}$	$13.667 \pm 0.031^{(1)}$	10143
2MASS J00361617+1821104	L3.5 (28)	$114.42 \pm 0.21^{(2)}$	$12.466 \pm 0.027^{(1)}$	$11.588 \pm 0.030^{(1)}$	10143
2MASS J00452143+1634446	L2beta (24)	$65.02 \pm 0.23^{(2)}$	$13.059 \pm 0.022^{(1)}$	$12.059 \pm 0.035^{(1)}$	10143
2MASS J01075242+0041563	L8 (3)	$64 \pm 5^{(4)}$	$15.82 \pm 0.06^{(1)}$	$14.51 \pm 0.04^{(1)}$	10143

Table 2 continued on next page

Table 2 (continued)

2MASSJ	SpT (ref.)	Parallax [mas] (ref.)	J [mag] (ref.)	H [mag] (ref.)	HST program
2MASS J01092170+2949255	M9.5 <sup>(12)</sup>	62.78 ± 0.24 <sup>(2)</sup>	12.912 ± 0.021 <sup>(1)</sup>	12.158 ± 0.024 <sup>(1)</sup>	10879
2MASS J01235905-4240073	L0.5 <sup>(22)</sup>	38.78 ± 0.16 <sup>(2)</sup>	13.153 ± 0.024 <sup>(1)</sup>	12.470 ± 0.023 <sup>(1)</sup>	10143
2MASS J01443536-0716142	L6.5 <sup>(3)</sup>	79.0 ± 0.6 <sup>(2)</sup>	14.191 ± 0.026 <sup>(1)</sup>	13.008 ± 0.029 <sup>(1)</sup>	10143
2MASS J01473282-4954478	M8+L2 <sup>(7)</sup>	27.9 ± 0.4 <sup>(2)</sup>	13.058 ± 0.027 <sup>(1)</sup>	12.366 ± 0.026 <sup>(1)</sup>	10143
2MASS J01514155+1244300	T0.5 <sup>(8)</sup>	46.7 ± 3.4 <sup>(4)</sup>	16.57 ± 0.13 <sup>(1)</sup>	15.60 ± 0.11 <sup>(1)</sup>	9833
2MASS J01550354+0950003	L4 <sup>(14)</sup>	44.7 ± 0.7 <sup>(2)</sup>	14.82 ± 0.04 <sup>(1)</sup>	13.763 ± 0.034 <sup>(1)</sup>	10143
2MASS J02052940-1159296	L7V <sup>(16)</sup>	50.6 ± 1.5 <sup>(4)</sup>	14.587 ± 0.030 <sup>(1)</sup>	13.57 ± 0.04 <sup>(1)</sup>	11136
2MASS J02074284+0000564	T4.5 <sup>(23)</sup>	35 ± 10 <sup>(4)</sup>	16.730 ± 0.013 <sup>(10)</sup>	16.81 ± 0.04 <sup>(10)</sup>	9833
2MASS J02132880+4444453	L1.5 <sup>(11)</sup>	51.7 ± 0.4 <sup>(2)</sup>	13.494 ± 0.025 <sup>(1)</sup>	12.757 ± 0.024 <sup>(1)</sup>	10143
2MASS J02284243+1639329	M8.7V <sup>(6)</sup>	46.0 ± 0.4 <sup>(2)</sup>	13.166 ± 0.026 <sup>(1)</sup>	12.325 ± 0.030 <sup>(1)</sup>	10879
2MASS J02431371-2453298	T6.0 <sup>(9)</sup>	94 ± 4 <sup>(4)</sup>	15.38 ± 0.05 <sup>(1)</sup>	15.14 ± 0.11 <sup>(1)</sup>	9833
2MASS J02511490-0352459	L3 <sup>(11)</sup>	90.6 ± 3.0 <sup>(36)</sup>	13.059 ± 0.027 <sup>(1)</sup>	12.254 ± 0.024 <sup>(1)</sup>	10879
2MASS J02550357-4700509	L9 <sup>(3)</sup>	205.33 ± 0.25 <sup>(2)</sup>	13.246 ± 0.027 <sup>(1)</sup>	12.204 ± 0.024 <sup>(1)</sup>	10879
2MASS J02572581-3105523	L8.5 <sup>(3)</sup>	102.4 ± 0.6 <sup>(2)</sup>	14.67 ± 0.04 <sup>(1)</sup>	13.520 ± 0.030 <sup>(1)</sup>	10143
2MASS J03140344+1603056	L0 <sup>(7)</sup>	73.43 ± 0.28 <sup>(2)</sup>	12.526 ± 0.024 <sup>(1)</sup>	11.82 ± 0.04 <sup>(1)</sup>	10143
2MASS J03185403-3421292	L7 <sup>(3)</sup>	73 ± 8 <sup>(4)</sup>	15.57 ± 0.05 <sup>(1)</sup>	14.35 ± 0.04 <sup>(1)</sup>	10879
2MASS J03480772-6022270	T7 <sup>(8)</sup>	120.1 ± 1.8 <sup>(45)</sup>	15.32 ± 0.05 <sup>(1)</sup>	15.56 ± 0.14 <sup>(1)</sup>	9833
2MASS J03552337+1133437	L5gamma <sup>(24)</sup>	109.6 ± 0.7 <sup>(2)</sup>	14.050 ± 0.024 <sup>(1)</sup>	12.530 ± 0.030 <sup>(1)</sup>	10143
2MASS J04151954-0935066	T8.0 <sup>(9)</sup>	174.3 ± 2.8 <sup>(4)</sup>	15.69 ± 0.06 <sup>(1)</sup>	15.54 ± 0.11 <sup>(1)</sup>	9833
2MASS J04234858-0414035	L6.5+T2 <sup>(5)</sup>	67.9 ± 1.5 <sup>(2)</sup>	14.465 ± 0.027 <sup>(1)</sup>	13.463 ± 0.035 <sup>(1)</sup>	9833, 11136
2MASS J04291842-3123568	M7.5 <sup>(15)</sup>	59.38 ± 0.20 <sup>(2)</sup>	10.874 ± 0.024 <sup>(1)</sup>	10.211 ± 0.024 <sup>(1)</sup>	10143
2MASS J04390101-2353083	L4.5 <sup>(3)</sup>	80.8 ± 0.5 <sup>(2)</sup>	14.408 ± 0.029 <sup>(1)</sup>	13.409 ± 0.029 <sup>(1)</sup>	10143
2MASS J04433761+0002051	M9.0V <sup>(40)</sup>	47.41 ± 0.19 <sup>(2)</sup>	12.507 ± 0.026 <sup>(1)</sup>	11.804 ± 0.024 <sup>(1)</sup>	10879
2MASS J04455387-3048204	L2 <sup>(11)</sup>	61.97 ± 0.18 <sup>(2)</sup>	13.393 ± 0.026 <sup>(1)</sup>	12.580 ± 0.024 <sup>(1)</sup>	10143
2MASS J05002100+0330501	L4pec <sup>(14)</sup>	76.2 ± 0.4 <sup>(2)</sup>	13.669 ± 0.024 <sup>(1)</sup>	12.683 ± 0.023 <sup>(1)</sup>	10143
2MASS J05160945-0445499	T5.5 <sup>(8)</sup>	44 ± 6 <sup>(4)</sup>	15.98 ± 0.08 <sup>(1)</sup>	15.72 ± 0.17 <sup>(1)</sup>	9833
2MASS J05185995-2828372	L6+T4 <sup>(5)</sup>	48 ± 7 <sup>(4)</sup>	15.98 ± 0.10 <sup>(1)</sup>	14.83 ± 0.07 <sup>(1)</sup>	10247, 11136
2MASS J05233822-1403022	L2.5 <sup>(15)</sup>	78.36 ± 0.19 <sup>(2)</sup>	13.084 ± 0.024 <sup>(1)</sup>	12.220 ± 0.022 <sup>(1)</sup>	10143
2MASS J06244132+2325585	M4V <sup>(30)</sup>	117.74 ± 0.06 <sup>(2)</sup>	8.662 ± 0.020 <sup>(1)</sup>	8.16 ± 0.06 <sup>(1)</sup>	9704
2MASS J06244595-4521548	L6.5 <sup>(3)</sup>	81.6 ± 0.5 <sup>(2)</sup>	14.480 ± 0.029 <sup>(1)</sup>	13.335 ± 0.028 <sup>(1)</sup>	10143
2MASS J06523073+4710348	L3.5+L6.5 <sup>(39)</sup>	109.7 ± 0.4 <sup>(2)</sup>	13.511 ± 0.023 <sup>(1)</sup>	12.384 ± 0.024 <sup>(1)</sup>	10143
2MASS J07003664+3157266	L3+L6.5 <sup>(5)</sup>	88.28 ± 0.35 <sup>(2)</sup>	12.923 ± 0.023 <sup>(1)</sup>	11.947 ± 0.016 <sup>(1)</sup>	10143
2MASS J07271824+1710012	T7.0 <sup>(9)</sup>	110.1 ± 2.3 <sup>(4)</sup>	15.60 ± 0.06 <sup>(1)</sup>	15.76 ± 0.17 <sup>(1)</sup>	9833
2MASS J07554795+2212169	T5.2 <sup>(9)</sup>	58.9 ± 3.3 <sup>(46)</sup>	15.73 ± 0.06 <sup>(1)</sup>	15.67 ± 0.14 <sup>(1)</sup>	9833
2MASS J08251968+2115521	L7.5V <sup>(18)</sup>	92.2 ± 1.2 <sup>(2)</sup>	15.100 ± 0.034 <sup>(1)</sup>	13.792 ± 0.032 <sup>(1)</sup>	10143
2MASS J08300825+4828482	L9.5 <sup>(3)</sup>	76.4 ± 3.4 <sup>(4)</sup>	15.44 ± 0.05 <sup>(1)</sup>	14.34 ± 0.04 <sup>(1)</sup>	10879
2MASS J08354256-0819237	L6.5 <sup>(3)</sup>	138.61 ± 0.28 <sup>(2)</sup>	13.169 ± 0.024 <sup>(1)</sup>	11.938 ± 0.024 <sup>(1)</sup>	10143
SDSS J083717.21-000018.0	T1 <sup>(8)</sup>	34 ± 13 <sup>(4)</sup>	16.989 ± 0.018 <sup>(10)</sup>	16.290 ± 0.018 <sup>(10)</sup>	9833
2MASS J08472872-1532372	L1.5 <sup>(3)</sup>	56.92 ± 0.32 <sup>(2)</sup>	13.513 ± 0.026 <sup>(1)</sup>	12.629 ± 0.027 <sup>(1)</sup>	10143
2MASS J08503593+1057156	L6.5+L8.5 <sup>(5)</sup>	31.4 ± 0.6 <sup>(13)</sup>	16.47 ± 0.11 <sup>(1)</sup>	15.22 ± 0.09 <sup>(1)</sup>	9843
2MASS J08592547-1949268	L8 <sup>(3)</sup>	65 ± 6 <sup>(4)</sup>	15.53 ± 0.05 <sup>(1)</sup>	14.44 ± 0.04 <sup>(1)</sup>	10879
2MASS J09083803+5032088	L8 <sup>(3)</sup>	95.8 ± 0.7 <sup>(2)</sup>	14.549 ± 0.023 <sup>(1)</sup>	13.477 ± 0.030 <sup>(1)</sup>	10143
2MASS J09111297+7401081	L0 <sup>(11)</sup>	40.08 ± 0.17 <sup>(2)</sup>	12.921 ± 0.027 <sup>(1)</sup>	12.205 ± 0.030 <sup>(1)</sup>	10143
2MASS J09153413+0422045	L6 <sup>(3)</sup>	55.9 ± 1.1 <sup>(19)</sup>	14.548 ± 0.030 <sup>(1)</sup>	13.531 ± 0.032 <sup>(1)</sup>	10143
2MASS J09211410-2104446	L1 <sup>(3)</sup>	79.31 ± 0.23 <sup>(2)</sup>	12.779 ± 0.024 <sup>(1)</sup>	12.152 ± 0.022 <sup>(1)</sup>	10143
2MASS J09261537+5847212	T3.5+T5 <sup>(5)</sup>	43.7 ± 1.1 <sup>(5)</sup>	15.90 ± 0.06 <sup>(1)</sup>	15.31 ± 0.09 <sup>(1)</sup>	9833
2MASS J10210969-0304197	T1+T4 <sup>(17)</sup>	33.7 ± 1.2 <sup>(13)</sup>	16.25 ± 0.09 <sup>(1)</sup>	15.35 ± 0.10 <sup>(1)</sup>	9833

Table 2 continued on next page

Table 2 (continued)

2MASSJ	SpT (ref.)	Parallax [mas] (ref.)	J [mag] (ref.)	H [mag] (ref.)	HST program
2MASS J10224821+5825453	L0.6V <sup>(6)</sup>	54.33 ± 0.31 <sup>(2)</sup>	13.499 ± 0.026 <sup>(1)</sup>	12.640 ± 0.030 <sup>(1)</sup>	10879
2MASS J10255227+3212349	L9 <sup>(3)</sup>	37.3 ± 1.2 <sup>(41)</sup>	16.89 ± 0.05 <sup>(37)</sup>	15.59 ± 0.17 <sup>(1)</sup>	10879
2MASS J10430758+2225236	L8.5 <sup>(3)</sup>	52.4 ± 2.9 <sup>(46)</sup>	15.97 ± 0.06 <sup>(1)</sup>	14.73 ± 0.04 <sup>(1)</sup>	10879
2MASS J10452400-0149576	L1 <sup>(21)</sup>	58.66 ± 0.24 <sup>(2)</sup>	13.160 ± 0.024 <sup>(1)</sup>	12.352 ± 0.025 <sup>(1)</sup>	10143
2MASS J10484281+0111580	L1 <sup>(3)</sup>	66.46 ± 0.21 <sup>(2)</sup>	12.924 ± 0.023 <sup>(1)</sup>	12.140 ± 0.022 <sup>(1)</sup>	10143
2MASS J10511900+5613086	L2 <sup>(7)</sup>	64.00 ± 0.19 <sup>(2)</sup>	13.244 ± 0.026 <sup>(1)</sup>	12.420 ± 0.030 <sup>(1)</sup>	10143
2MASS J10584787-1548172	L3V <sup>(16)</sup>	54.6 ± 0.5 <sup>(2)</sup>	14.155 ± 0.035 <sup>(1)</sup>	13.226 ± 0.025 <sup>(1)</sup>	10879
2MASS J11040127+1959217	L4 <sup>(3)</sup>	55.9 ± 0.4 <sup>(2)</sup>	14.380 ± 0.026 <sup>(1)</sup>	13.476 ± 0.034 <sup>(1)</sup>	10143
2MASS J11083081+6830169	L1e <sup>(12)</sup>	61.35 ± 0.20 <sup>(2)</sup>	13.120 ± 0.020 <sup>(25)</sup>	12.240 ± 0.020 <sup>(25)</sup>	10143
2MASS J11101001+0116130	T5.5 <sup>(23)</sup>	52.1 ± 1.2 <sup>(32)</sup>	16.161 ± 0.008 <sup>(10)</sup>	16.197 ± 0.021 <sup>(10)</sup>	9833
2MASS J11553952-3727350	L2e <sup>(21)</sup>	84.57 ± 0.19 <sup>(2)</sup>	12.811 ± 0.024 <sup>(1)</sup>	12.040 ± 0.026 <sup>(1)</sup>	10879
2MASS J12035812+0015500	L5.0V <sup>(6)</sup>	67.2 ± 0.6 <sup>(2)</sup>	14.006 ± 0.026 <sup>(1)</sup>	13.056 ± 0.024 <sup>(1)</sup>	10879
2MASS J12130336-0432437	L4.2V <sup>(6)</sup>	59.5 ± 1.0 <sup>(2)</sup>	14.68 ± 0.04 <sup>(1)</sup>	13.648 ± 0.025 <sup>(1)</sup>	10143
2MASS J12171110-0311131	T7.5 <sup>(8)</sup>	90.8 ± 2.2 <sup>(4)</sup>	15.86 ± 0.06 <sup>(1)</sup>	15.75 ± 0.12 <sup>(1)</sup>	9833
2MASS J12212770+0257198	L0.5 <sup>(3)</sup>	53.95 ± 0.25 <sup>(2)</sup>	13.169 ± 0.023 <sup>(1)</sup>	12.410 ± 0.025 <sup>(1)</sup>	10143
2MASS J12545393-0122474	T2e: <sup>(35)</sup>	74.2 ± 2.3 <sup>(2)</sup>	14.891 ± 0.035 <sup>(1)</sup>	14.090 ± 0.025 <sup>(1)</sup>	9833
2MASS J13004255+1912354	L1.7V <sup>(6)</sup>	71.68 ± 0.20 <sup>(2)</sup>	12.717 ± 0.022 <sup>(1)</sup>	12.080 ± 0.023 <sup>(1)</sup>	10879
2MASS J14213145+1827407	M8.9V <sup>(6)</sup>	52.67 ± 0.26 <sup>(2)</sup>	13.231 ± 0.021 <sup>(1)</sup>	12.428 ± 0.021 <sup>(1)</sup>	10879
2MASS J14252798-3650229	L4 <sup>(14)</sup>	84.52 ± 0.34 <sup>(2)</sup>	13.747 ± 0.028 <sup>(1)</sup>	12.575 ± 0.022 <sup>(1)</sup>	10879
2MASS J14283132+5923354	L4.4V <sup>(6)</sup>	45.4 ± 0.5 <sup>(2)</sup>	14.78 ± 0.04 <sup>(1)</sup>	13.88 ± 0.04 <sup>(1)</sup>	10143
2MASS J14392836+1929149	L1V <sup>(16)</sup>	69.6 ± 0.5 <sup>(4)</sup>	12.759 ± 0.019 <sup>(1)</sup>	12.041 ± 0.019 <sup>(1)</sup>	10879
2MASS J14482563+1031590	L5.5 <sup>(3)</sup>	71.3 ± 0.7 <sup>(2)</sup>	14.556 ± 0.034 <sup>(1)</sup>	13.433 ± 0.033 <sup>(1)</sup>	10143
2MASS J15031961+2525196	T5.5 <sup>(34)</sup>	154.9 ± 1.1 <sup>(2)</sup>	13.937 ± 0.024 <sup>(1)</sup>	13.856 ± 0.031 <sup>(1)</sup>	9833
2MASS J15065441+1321060	L3 <sup>(12)</sup>	85.58 ± 0.29 <sup>(2)</sup>	13.365 ± 0.023 <sup>(1)</sup>	12.380 ± 0.021 <sup>(1)</sup>	10879
2MASS J15074769-1627386	L5V <sup>(18)</sup>	135.23 ± 0.33 <sup>(2)</sup>	12.830 ± 0.027 <sup>(1)</sup>	11.895 ± 0.024 <sup>(1)</sup>	10143
2MASS J15150083+4847416	L6.5 <sup>(15)</sup>	102.6 ± 0.6 <sup>(19)</sup>	14.111 ± 0.029 <sup>(1)</sup>	13.099 ± 0.031 <sup>(1)</sup>	10879
2MASS J15341711+1615463	T1.5+T5.5 <sup>(17)</sup>	24.9 ± 1.1 <sup>(5)</sup>	16.75 ± 0.13 <sup>(1)</sup>	16.08 ± 0.16 <sup>(1)</sup>	11136
2MASS J15394189-0520428	L4.2V <sup>(6)</sup>	58.8 ± 0.4 <sup>(2)</sup>	13.922 ± 0.029 <sup>(1)</sup>	13.060 ± 0.026 <sup>(1)</sup>	10143
2MASS J15525906+2948485	L0e <sup>(42)</sup>	49.00 ± 0.20 <sup>(2)</sup>	13.478 ± 0.026 <sup>(1)</sup>	12.606 ± 0.026 <sup>(1)</sup>	10143
2MASS J15530228+1532369	T6.5+T7.5 <sup>(5)</sup>	75.1 ± 0.9 <sup>(5)</sup>	15.82 ± 0.07 <sup>(1)</sup>	15.94 ± 0.16 <sup>(1)</sup>	9833
2MASS J16241436+0029158	T6V <sup>(9)</sup>	90.9 ± 1.2 <sup>(4)</sup>	15.49 ± 0.05 <sup>(1)</sup>	15.52 ± 0.10 <sup>(1)</sup>	9833
2MASS J16580380+7027015	L1(e) <sup>(12)</sup>	54.12 ± 0.21 <sup>(2)</sup>	13.288 ± 0.024 <sup>(1)</sup>	12.470 ± 0.032 <sup>(1)</sup>	10143
2MASS J17054834-0516462	L1 <sup>(3)</sup>	52.67 ± 0.35 <sup>(2)</sup>	13.309 ± 0.030 <sup>(1)</sup>	12.552 ± 0.024 <sup>(1)</sup>	10143
2MASS J17072343-0558249	M9+L3 <sup>(7)</sup>	89.26 ± 2.2 <sup>(47)</sup>	12.052 ± 0.023 <sup>(1)</sup>	11.260 ± 0.027 <sup>(1)</sup>	10143
2MASS J17210390+3344160	L5.3:V <sup>(6)</sup>	61.32 ± 0.20 <sup>(2)</sup>	13.625 ± 0.023 <sup>(1)</sup>	12.952 ± 0.026 <sup>(1)</sup>	10879
2MASS J17281150+3948593	L5+L6.5 <sup>(17)</sup>	36.4 ± 0.6 <sup>(13)</sup>	15.99 ± 0.08 <sup>(1)</sup>	14.76 ± 0.07 <sup>(1)</sup>	9843
2MASS J17312974+2721233	L0 <sup>(7)</sup>	83.74 ± 0.12 <sup>(2)</sup>	12.094 ± 0.027 <sup>(1)</sup>	11.391 ± 0.030 <sup>(1)</sup>	10143
2MASS J17503293+1759042	T3.5 <sup>(8)</sup>	36 ± 5 <sup>(4)</sup>	16.34 ± 0.10 <sup>(1)</sup>	15.95 ± 0.13 <sup>(1)</sup>	9833
2MASS J17534518-6559559	L4 <sup>(26)</sup>	63.82 ± 0.32 <sup>(2)</sup>	14.095 ± 0.028 <sup>(1)</sup>	13.108 ± 0.027 <sup>(1)</sup>	10143
2MASS J18071593+5015316	L1 <sup>(3)</sup>	68.33 ± 0.13 <sup>(2)</sup>	12.934 ± 0.024 <sup>(1)</sup>	12.127 ± 0.031 <sup>(1)</sup>	10143
2MASS J19360187-5502322	L4 <sup>(26)</sup>	45.0 ± 0.5 <sup>(2)</sup>	14.49 ± 0.04 <sup>(1)</sup>	13.628 ± 0.035 <sup>(1)</sup>	10143
2MASS J20025073-0521524	L5.5 <sup>(3)</sup>	56.7 ± 1.5 <sup>(2)</sup>	15.32 ± 0.05 <sup>(1)</sup>	14.28 ± 0.05 <sup>(1)</sup>	10879
2MASS J20282035+0052265	L2.5 <sup>(3)</sup>	35.2 ± 0.7 <sup>(2)</sup>	14.298 ± 0.035 <sup>(1)</sup>	13.380 ± 0.030 <sup>(1)</sup>	10879
2MASS J20360316+1051295	L2 <sup>(3)</sup>	42.4 ± 0.4 <sup>(2)</sup>	13.950 ± 0.026 <sup>(1)</sup>	13.018 ± 0.022 <sup>(1)</sup>	10143
SDSS J205235.31-160929.8	L8.5+T1.5 <sup>(5)</sup>	33.7 ± 0.7 <sup>(13)</sup>	16.040 ± 0.030 <sup>(4)</sup>	15.450 ± 0.030 <sup>(4)</sup>	11136
2MASS J20575409-0252302	L1 <sup>(3)</sup>	64.47 ± 0.24 <sup>(2)</sup>	13.121 ± 0.024 <sup>(1)</sup>	12.268 ± 0.024 <sup>(1)</sup>	10143
2MASS J21041491-1037369	L2 <sup>(3)</sup>	58.2 ± 0.4 <sup>(2)</sup>	13.841 ± 0.029 <sup>(1)</sup>	12.975 ± 0.025 <sup>(1)</sup>	10143

Table 2 continued on next page

**Table 2** (*continued*)

2MASSJ	SpT (ref.)	Parallax [mas] (ref.)	J [mag] (ref.)	H [mag] (ref.)	HST program
2MASS J21392676+0220226	L8.5+T3.5 <sup>(38)</sup>	101.5 ± 2.0 <sup>(27)</sup>	15.26 ± 0.05 <sup>(1)</sup>	14.16 ± 0.05 <sup>(1)</sup>	10143
2MASS J21481633+4003594	L7 <sup>(3)</sup>	123.3 ± 0.5 <sup>(2)</sup>	14.147 ± 0.029 <sup>(1)</sup>	12.780 ± 0.030 <sup>(1)</sup>	10879
2MASS J21522609+0937575	L6+L6 <sup>(7)</sup>	40.9 ± 6.9 <sup>(46)</sup>	15.190 ± 0.032 <sup>(1)</sup>	14.08 ± 0.04 <sup>(1)</sup>	10143
2MASS J22041052-5646577	T1V+T6V <sup>(33)</sup>	275.8 ± 0.7 <sup>(29)</sup>	11.908 ± 0.022 <sup>(1)</sup>	11.306 ± 0.024 <sup>(1)</sup>	11136
2MASS J22244381-0158521	L4.5V <sup>(18)</sup>	86.6 ± 0.7 <sup>(2)</sup>	14.073 ± 0.027 <sup>(1)</sup>	12.818 ± 0.026 <sup>(1)</sup>	10879
2MASS J22282889-4310262	T6.5 <sup>(8)</sup>	92.1 ± 2.6 <sup>(27)</sup>	15.66 ± 0.07 <sup>(1)</sup>	15.36 ± 0.12 <sup>(1)</sup>	9833
2MASS J22373255+3922398	M9.5 <sup>(11)</sup>	47.61 ± 0.20 <sup>(2)</sup>	13.343 ± 0.022 <sup>(1)</sup>	12.691 ± 0.021 <sup>(1)</sup>	10879
2MASS J22490917+3205489	L5 <sup>(20)</sup>	49.7 ± 3.2 <sup>(46)</sup>	15.48 ± 0.06 <sup>(1)</sup>	14.35 ± 0.05 <sup>(1)</sup>	10143
2MASS J22521073-1730134	L4.5+T3.5 <sup>(5)</sup>	59.1 ± 0.8 <sup>(2)</sup>	14.313 ± 0.029 <sup>(1)</sup>	13.360 ± 0.030 <sup>(1)</sup>	10143, 11136
2MASS J22541892+3123498	T5.0 <sup>(9)</sup>	72 ± 3 <sup>(48)</sup>	15.26 ± 0.05 <sup>(1)</sup>	15.02 ± 0.08 <sup>(1)</sup>	9833
2MASS J22551861-5713056	L6:+L8 <sup>(7)</sup>	58.9 ± 0.6 <sup>(2)</sup>	14.083 ± 0.030 <sup>(1)</sup>	13.189 ± 0.032 <sup>(1)</sup>	10879
2MASS J23254530+4251488	L8 <sup>(11)</sup>	67.6 ± 2.1 <sup>(2)</sup>	15.49 ± 0.05 <sup>(1)</sup>	14.45 ± 0.05 <sup>(1)</sup>	10143
2MASS J23391025+1352284	T5.4 <sup>(9)</sup>	62.7 ± 4.4 <sup>(46)</sup>	16.24 ± 0.11 <sup>(1)</sup>	15.82 ± 0.15 <sup>(1)</sup>	9833
2MASS J23515044-2537367	M9e <sup>(22)</sup>	49.1 ± 0.4 <sup>(2)</sup>	12.471 ± 0.026 <sup>(1)</sup>	11.725 ± 0.022 <sup>(1)</sup>	10143

**References**—Reference Key 1: [Cutri et al. \(2003\)](#), 2: [Gaia Collaboration et al. \(2018\)](#), 3: [Faherty et al. \(2012\)](#), 4: [Schneider et al. \(2014\)](#), 5: [Skrzypek et al. \(2016\)](#), 6: [Dupuy & Liu \(2012\)](#), 7: [Bardalez Gagliuffi et al. \(2015\)](#), 8: [Schmidt et al. \(2007\)](#), 9: [Burgasser et al. \(2002\)](#), 10: [Gagné et al. \(2015\)](#), 11: [Dupuy & Liu \(2017\)](#), 12: [Reid et al. \(2008b\)](#), 13: [Faherty et al. \(2009\)](#), 14: [Marocco et al. \(2013\)](#), 15: [Kirkpatrick et al. \(2000\)](#), 16: [Gelino et al. \(2014\)](#), 17: [Smart et al. \(2013\)](#), 18: [Burgasser et al. \(2003b\)](#), 19: [Cruz et al. \(2003\)](#), 20: [Konopacky et al. \(2010\)](#), 21: [Burgasser et al. \(2000\)](#), 22: [Aller et al. \(2016\)](#), 23: [Lodieu et al. \(2005\)](#), 24: [Liu et al. \(2006\)](#), 25: [Burgasser et al. \(2003a\)](#), 26: [Leggett et al. \(2001\)](#), 27: [Timney et al. \(2014\)](#), 28: [Reid et al. \(2000\)](#), 29: [Perryman et al. \(1997\)](#), 30: [Kirkpatrick et al. \(1991\)](#), 31: [Faherty et al. \(2016\)](#), 32: [Reid et al. \(2006\)](#), 33: [Burgasser et al. \(2005\)](#), 34: [Chiu et al. \(2006\)](#), 35: [Burgasser et al. \(2006a\)](#), 36: [Cardoso et al. \(2015\)](#), 37: [West et al. \(2008\)](#), 38: [Metchev et al. \(2008\)](#), 39: [Reylé et al. \(2010\)](#), 40: [Burgasser et al. \(2010\)](#), 41: [Deshpande et al. \(2012\)](#), 42: [Kirkpatrick et al. \(2016\)](#), 43: [Liu et al. \(2016\)](#), 44: [Marocco et al. \(2015\)](#), 45: [Kirkpatrick et al. \(2019\)](#), 46: [Best et al. \(2020\)](#), 47: [Smart et al. \(2018\)](#), 48: [Manjavacas et al. \(2013\)](#)

While previous studies of these data sets have found tight companions, we analyzed all images with no prior knowledge other than a visual inspection for obvious secondary sources. KPI produces improved astrometric precision and searches for tighter and fainter companions around targets previously thought to be single. While [Pope et al. \(2013\)](#) previously analyzed the [Reid et al. \(2006, 2008a\)](#) observations using KPI, this work uses a new code-base with a detailed treatment of phase errors, calibration, model comparison, and detection limits in addition to analyzing data from 5 more *HST* programs. There are also a few more subtle differences in the analysis which are discussed further below.

### 3. METHODS

#### 3.1. Kernel-phase Analysis

The kernel phase derivation was first presented by [Martinache \(2010\)](#) and is summarized here for clarity since the technique is still relatively obscure. KPI works by modeling the full telescope aperture as a grid of sub-apertures. From this grid, a set of baselines (vectors in  $uv$  space) can be generated by pairing apertures. [Figure 1](#) shows our model of the *HST/NICMOS* aperture and the baselines it samples. Phases (or more generally, complex visibilities) are then sampled from the Fourier transform of the image at each of these points in  $uv$  space. Kernel phases can then be constructed based on the geometry of the model aperture using linear algebra outlined below.

Each measured phase ( $\Phi$ ) is made up of the true source phase ( $\Phi_0$ ) and a combination of phase errors ( $\phi$ ) introduced by pupil path length differences from each of the apertures contributing to the

baseline:

$$\Phi = \text{Arg} \left[ \sum_{(j,k)} e^{i(\Phi_0 + \phi_j - \phi_k)} \right], \quad (1)$$

where the pair  $(j, k)$  denotes the baselines contributing to the specific visibility. The complex interferometric visibility is thus a superposition of vectors (i.e. the *phases* do not strictly add). If we assume these error terms are small, we can approximate each complex phasor as a linear sum,  $e^{i(\phi_j - \phi_k)} \approx 1 + i(\phi_j - \phi_k)$ , allowing us to write the measured phase as a linear combination:

$$\Phi \approx \Phi_0 + \frac{1}{r} \sum_{(j,k)} (\phi_j - \phi_k), \quad (2)$$

where  $r$  is the number of  $(j, k)$  pairs for that specific phase measurement (i.e. number of redundant baselines contributing to the visibility). If we stack these equations for each sampled point in  $uv$  space, we can write the vector of all measured phase information as

$$\Phi = \Phi_0 + \mathbf{R}^{-1} \cdot \mathbf{A} \cdot \phi, \quad (3)$$

where the matrix  $\mathbf{R}$  is a diagonal matrix with  $1/r$  for each visibility, encoding the redundancies in the baselines. The matrix  $\mathbf{A}$  is a transfer matrix assembled from 1's and -1's in each row encoding the apertures contributing to each (redundant) baseline (any apertures not involved are 0 and apertures contributing multiple times to a single baseline are summed). For  $\phi$  of length  $n$  (the number of sub-apertures), and  $\Phi$  of length  $m$  (the number of unique visibilities), the shape of  $\mathbf{R}$  is  $m \times m$  and  $\mathbf{A}$  is  $m \times n$ .

Since our goal is to derive a quantity which does not involve the phase error term, we then construct the kernel,  $\mathbf{K}$ , of  $\mathbf{A}$  such that  $\mathbf{K} \cdot \mathbf{A} = \mathbf{0}$ . The matrix  $\mathbf{K}$  can be calculated using singular value decomposition (SVD, [Press et al. 2002](#)). This algorithm gives

$$\mathbf{A} = \mathbf{U} \cdot \mathbf{W} \cdot \mathbf{V}^T, \quad (4)$$

where the matrix  $\mathbf{W}$  is a diagonal matrix of positive or zero ‘singular values.’ The rows of  $\mathbf{K}$  are then the *columns* of  $\mathbf{U}$  corresponding to zero elements of  $\mathbf{W}$ . After multiplying equation 3 by  $\mathbf{R}$  and then  $\mathbf{K}$  we have

$$\mathbf{K} \cdot \mathbf{R} \cdot \Phi = \mathbf{K} \cdot \mathbf{R} \cdot \Phi_0. \quad (5)$$

This results in a set of phase-like observables ( $\mathbf{K} \cdot \mathbf{R} \cdot \Phi$ ), called kernel phases, which are free of instrumental phase errors.

### 3.2. Kernel-Phase Pipeline

The pipeline can be divided into four steps: aperture characterization, kernel-phase calculation, calibration, and model fitting. During aperture characterization we create a model interferometer that approximates the full aperture of the telescope, measure the associated baselines, and construct the transfer matrices. We then ingest the images and calculate the kernel phases. These kernel phases must then be calibrated to remove systematic errors. Once calibrated, we can then fit a single and binary model to the data and compare the results.



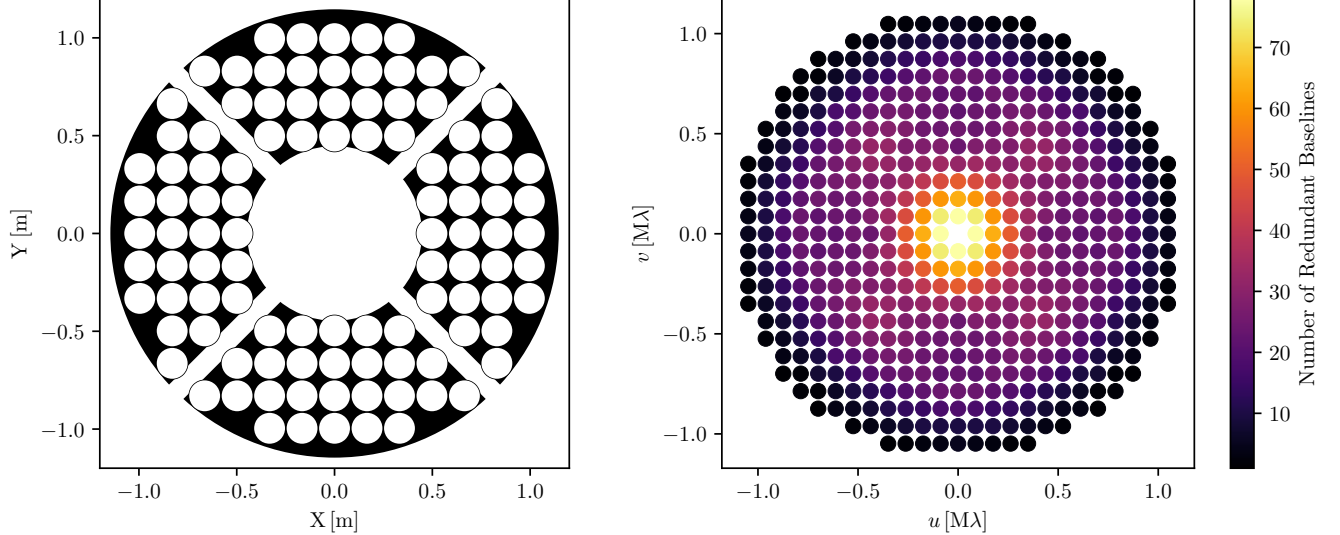


**Figure 1.** *Left:* HST aperture in black with simulated subapertures on top in white. *Right:* The corresponding baselines (at  $1.7 \mu\text{m}$ ), color coded by the number of distinct pairs of sub-apertures which contribute to the point. The 104 sub-apertures sample 258 spatial frequencies and generate 206 kernel phases.

### 3.2.1. Aperture Characterization

First we must construct a set of subapertures that models the full aperture of the telescope. Dimensions of the primary mirror and its obstructions were taken from the TinyTim software package (Krist et al. 2011) and are outlined in section 2.1. The model used in this work, shown in the left panel of Figure 1, was chosen by balancing a few characteristics: the fraction of the total aperture covered by subapertures ( $F_{\text{cov}}$ ), the length of the longest baseline ( $D_{\text{max}}$ ), the phase coverage or number of kernel phases relative to number of phases sampled ( $N_{\text{ker}}/N_{\text{B}}$ ), and the number of long baselines relative to the total number of baselines ( $N_{\text{long}}/N_{\text{B}}$ ). In general,  $F_{\text{cov}}$  and  $D_{\text{max}}$  trend larger with smaller subaperture size while  $N_{\text{ker}}/N_{\text{B}}$  and  $N_{\text{long}}/N_{\text{B}}$  trend smaller. The total number of kernel phases must also be kept to a reasonable number to keep fitting fast and such that we do not try to extract more information than is contained in the image. The theoretical minimum spacing of apertures is set by the size of the image, or in our case the super-Gaussian windowing function (see Section 3.2.2). The field of view, and therefore the smallest spacial frequency sampled by the image, is  $25\lambda/D$  and thus the minimum aperture spacing must be at least  $D/25$  or 0.096 m. Our chosen spacing is  $D/14.4$  or 0.166 m.

From the model of the aperture, the pipeline measures the baselines (right panel of Figure 1), constructs the  $\mathbf{A}$  matrix, and then calculates the kernel-phase transfer matrix  $\mathbf{K}$ . This step is only based on the telescope and sub-aperture geometry, and thus does not need to be repeated for each target.

### 3.2.2. Kernel-Phase calculation

The second step is to calculate kernel phases for each target. The pipeline reads in the images and interpolates over bad pixels. Bad pixels are identified from the data-quality flags associated with the individual images. Bad pixels are then iteratively replaced with the median of the 8 neighboring pixels. Other methods of dealing with bad pixels which avoid interpolation may be incorporated in

future releases and are discussed further in Section 6. The pipeline then finds the flux centroid of the target  $(x_{\text{cen}}, y_{\text{cen}})$  and windows the data with a super-Gaussian ( $e^{-(r/\sigma)^4}$ ) of width  $\sigma = 25\lambda/D$  ( $\sim 2.4$  and  $\sim 3.7$  arc sec in F110W and F170M, respectively) to limit sensitivity to readout noise (as done in Kraus et al. 2008). The images are then Fourier transformed using the basic `numpy` FFT routines. We then divided the complex visibilities by the position offset of the centroid:  $e^{i(x_{\text{cen}}*u+y_{\text{cen}}*v)}$ . Shifting in the Fourier domain avoids any pixel interpolation which may distort the phase information encoded in the image.

The phase at each point defined by the aperture model is then measured, along with the local dispersion. The errors associated with kernel phases are derived from the dispersion of the phases measured from the Fourier transform of the image. First, we define the scale on which the  $uv$  plane is sampled:  $\Delta f = d/2\lambda$ . This spatial frequency scale  $\Delta f$  is set by the grid spacing of the aperture model  $d$  (the diameter of the simulated sub-apertures), and the wavelength  $\lambda$ . This defines a circle of radius  $\Delta f$  around each point in the  $uv$  plane corresponding to all possible vectors from any point within the first sub aperture to any point within the second. The phase and associated error are then the mean and standard deviation of all points inside this circle given by the fast Fourier transform. These phases and associated errors are then propagated through the kernel-phase transfer matrix generated in the previous step to obtain the kernel phases and associated errors.

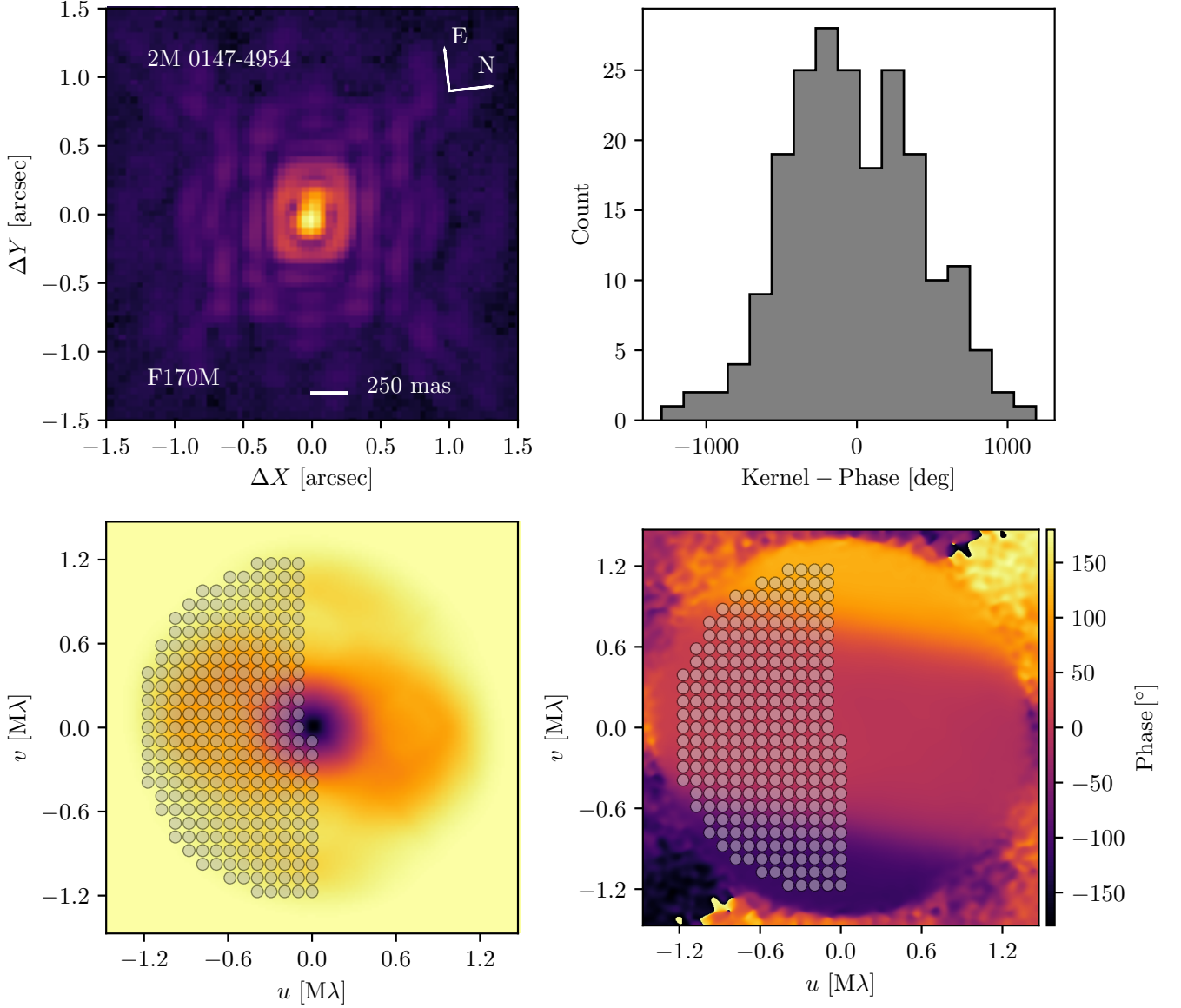
Sampling a number of phases around the baseline (rather than at a single point) appropriately captures the local dispersion of each phase, but not any systematic phase errors. Many previous applications of this analysis technique have introduced a global systematic error term, added in quadrature to the individual errors, to account for this and bring reduced  $\chi^2$  values of the best fit models closer to one. We fit this error term (iteratively, using a basic `python` fitting routine, e.g. `scipy.optimize.curve_fit` Virtanen et al. 2020) for each image since, for constant aberration, phase errors scale with  $\lambda$  and may vary over the detector.

Figure 2 shows intermediate steps for 2MASS J0147-4954 at this stage of the analysis: the bad pixel corrected and windowed image, the Fourier transform of the image (amplitude and phase) along with the modeled baselines, and the measured kernel phases. This target is marginally resolved at this wavelength, and a step function, characteristic of a binary, can clearly be seen in the Fourier-phase. The large dispersion of kernel phases in the upper right panel further indicates the presence of a companion. Figure 3 show the same plots but for 2MASS J1221+0257, a target with no companion. The flat phase and  $\sim 100\times$  smaller kernel phases indicate that this target does not have a companion.

### 3.2.3. Calibration

The third step is calibration. The phase signal of a single centered point source should be zero everywhere, producing all zero kernel phases. However, path-length offsets in the telescope and instrument produce non-zero phases and kernel phases (as seen in Figure 3). If these offsets are stable, which they are for similar observing setups (and for inherently stable space based observatories), they can be calibrated out. Subtracting off the (non-zero) kernel phases of an observed point source sets the zero-point in the science target such that a single source would now have all zero kernel phases.

Since no dedicated PSF calibrators were observed in these archival datasets, we use the science targets themselves as calibrators. To create kernel phases which can be used to calibrate science targets, a preliminary fit is run on each target to reject binaries and remove any small centroid offset error. As part of the data “onboarding” procedure, any images with visual signs of a companion are noted and rejected at this step. The best fit single point source model (x,y position offset) is



**Figure 2.** The progression from image to kernel phase for an observation of 2MASS J0147-4954, a brown dwarf with a companion at  $\sim 140$  mas ( $\sim 1\lambda/D$ ) and 2:1 contrast in F170M. *Top-left:* *HST/NICMOS* NIC1 image (fourth root scaling). *Bottom row:* Fourier-amplitude (left), and Fourier-phase (right). Gray circles show the spatial frequencies sampled by the model aperture shown in Figure 1. *Top-right* Histogram of measured kernel phases. A point source would have kernel phases of  $0^\circ$  (with some noise) which is clearly not the case.

then subtracted from the kernel phases of each point source to create calibrators. These are then used to calibrate science targets before fitting for binary parameters. Each science target is paired with 5 calibrators, balancing the increased confidence of a detection in multiple calibrators with the increased computation time of fitting multiple times. The results from these 5 independent fits are then used to characterize if a companion is present according to the metric discussed in Section 3.3.

We experimented with multiple calibrators chosen from the most singular sources (those which favored the single point source model over the double model the most), the closest on the detector, and

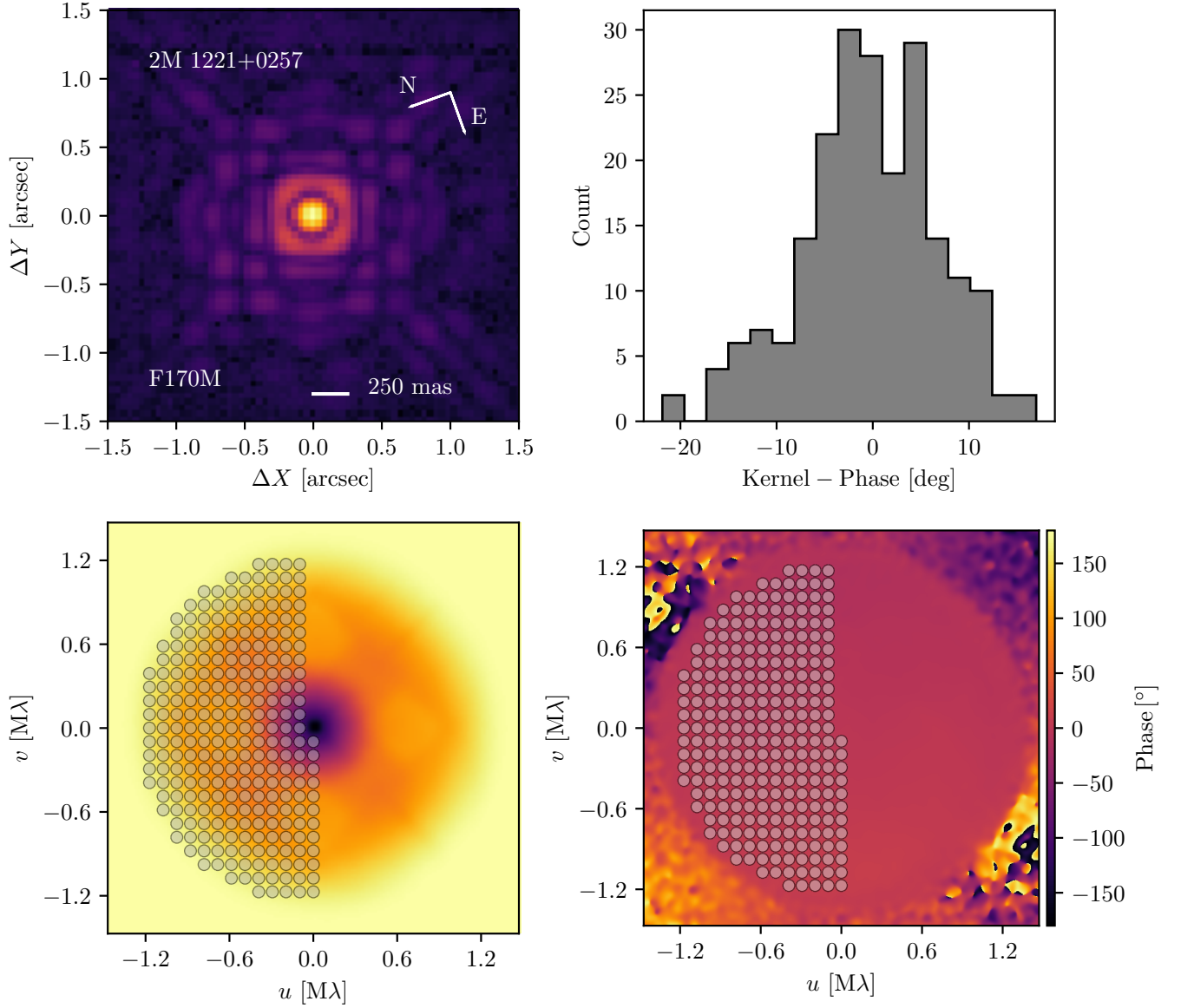


**Figure 3.** Similar to Figure 2 but for 2MASS J1221+0257, a brown dwarf with no companion. *Top-left:* *HST/NICMOS* NIC1 image (fourth root scaling). *Bottom row:* Fourier-amplitude (left), and Fourier-phase (right). Gray circles show the spatial frequencies sampled by the model aperture shown in Figure 1. *Top-right* Histogram of measured kernel phases. A point source would have kernel phases of  $0^\circ$  (with some noise) as is the case with this target.

a combination of the two metrics. We chose to use the calibrators located closest to the science target on the detector, as the detection limits (see Section 3.3) using those calibrators were significantly more sensitive. Targets which are co-located on the detector calibrate each other well since they accumulate similar phase offsets from passing through or reflecting off of the same region of optical elements within the telescope and instrument.

#### 3.2.4. Model Fitting

The fourth and final step is to pass the calibrated kernel phases to a Bayesian inference algorithm which fits a single and a double point source model to the data. The free parameters of the model are a small position offset (to allow for sub-pixel refinement of the centroid) and binary separation, position angle, and contrast ratio. We have chosen to use a Gaussian prior on the centroid (centered at 0 with a standard deviation of 10 mas), log-uniform priors on separation and contrast, and a uniform prior on position angle (the code we use allows a “wrapped” prior which we turn on for position angle). The log-uniform prior is commonly used as an uninformative prior on scaling parameters like separation and contrast as it allows for a wide range of values with equal probability over each power of 10.

The fitting routine used in this work, PyMultiNest (Buchner et al. 2014) uses a nested sampling algorithm which samples the entire prior volume, probabilistically constricting that volume down to the best fit(s) (Feroz & Hobson 2008; Feroz et al. 2009, 2019). Since it samples the entire (allowed) parameter space, it also allows the calculation of the Bayesian evidence which can then be used to calculate Bayes factors, comparing the single and double point source models (see Section 3.4).

Figure 4 shows the 1D and 2D posterior distributions along with the calibrated kernel phases generated from the data plotted against the best fit binary model for an binary system with a separation well below the diffraction limit, 2MASS J2351-2537. This test case, where the image does not clearly show a companion but the kernel phases plainly indicate the presence of a binary, demonstrates the power of this interferometric analysis, detecting an unresolved binary with a contrast ratio of  $\sim 2.5 : 1$  at  $\sim 0.3\lambda/D$ . Similar figures for all of our detected companions are shown in Figure Set 4.

### 3.3. Detection Limits

Detection limits were calculated in a similar manner to applications of NRM (Kraus et al. 2008, 2011). For each source-calibrator pair, the best fit single point-source model is subtracted from the calibrated kernel phases leaving behind noise (assuming no companion is present). The indices of these kernel phases are then scrambled, creating a new realization of the noise with the same properties. A single point source is then added back in to the scrambled kernel phases at the position of the single point source originally subtracted to replicate the signal of the centroid offset.

We then fit for contrast on a 100x100 grid in separation–PA space. Posteriors from these fits are then combined, marginalizing over PA. Since the indices have been scrambled, these fits are to kernel phases containing no real companions and thus the posteriors indicate what regions of parameter space produce spurious detections due to noise.

The confidence levels are then drawn such that the  $X\%$  confidence contour contains  $100 - X\%$  of the posterior moving from least dense to most dense areas. This is done using a Kernel Density Estimate of the posterior as a function of separation and contrast. Example detection limits are shown in Figures 5, 6, and 7 for a target with no companion, a confident detection, and a notable non-detection, respectively. Corresponding figures for the rest of the sources are shown in Figure Sets 5, 6, and 7, respectively with Marginal and Spurious detections shown in Figure Set 9.

We also run an injection/recovery grid to verify the NRM style scramble-and-fit detection limits which is overlaid in those figures. This mainly serves as a check to confirm that the scramble-and-fit detection limits are correctly positioned with respect to the companions that the pipeline is able to recover.

A fit companion is considered a confident detection if it is detected at  $> 5\sigma$  confidence in at least four of the five calibrators and the binary companion parameters are consistent between every pair

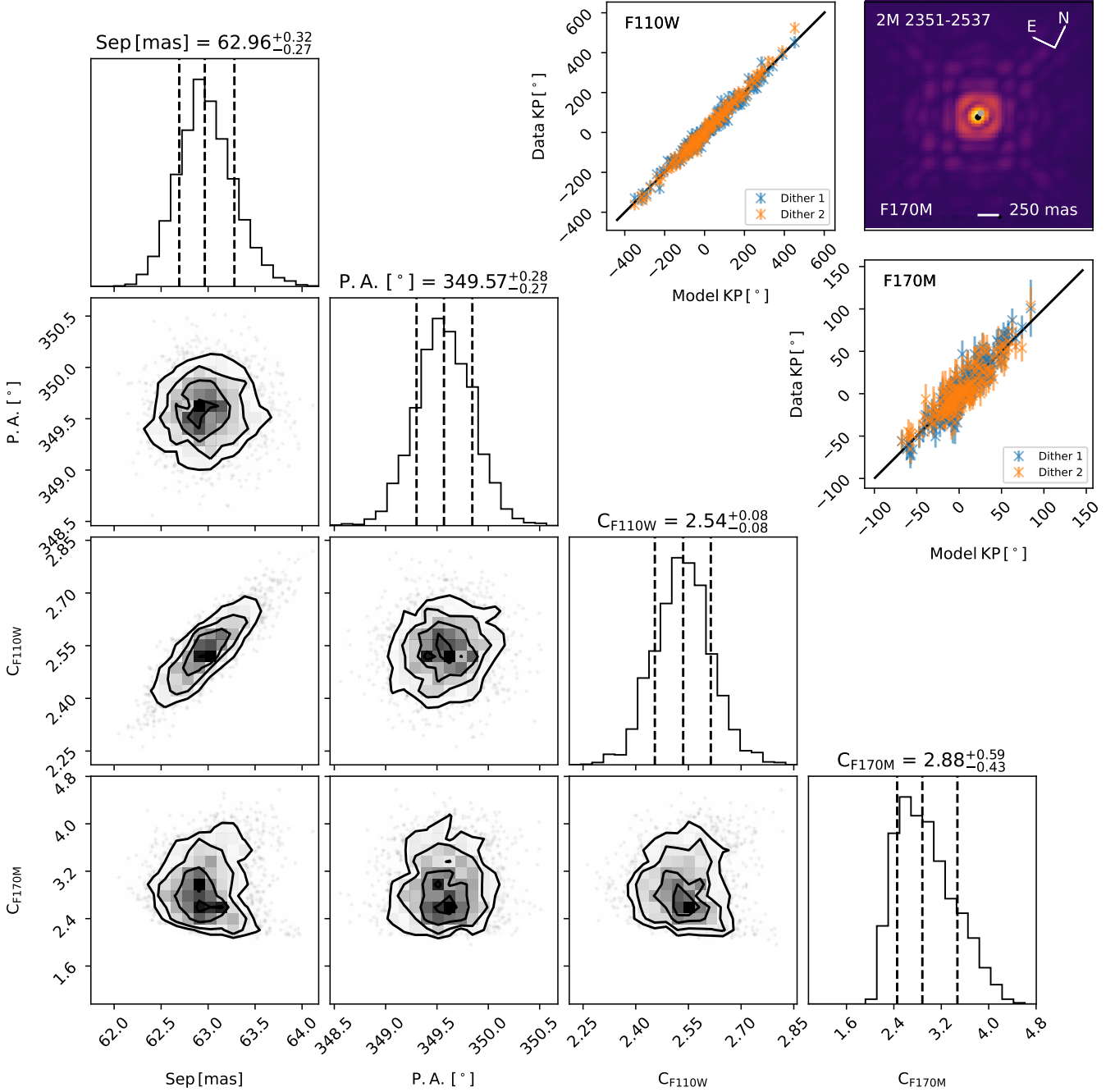


**Figure 4.** Results of fitting a double point source model to observations of 2MASS 2351-2537 (example image shown in the upper right corner with dots showing the position and contrast ratio of the two sources). *Lower Left:* Corner plot showing the posteriors of the four-parameter fit. Dashed lines indicate the median and  $\pm 1\sigma$  values (16th, 50th, and 86th percentiles). Top Right: Data kernel phases plotted against the best-fit model kernel phases indicating a good fit. Detection limits for this fit show it is significant at the  $> 5\sigma$  level and is consistent over multiple calibrators, while the Bayes-factors also indicate a preference for the binary model. Similar figures for each of our detections are shown in Figure Set 4 while marginal and spurious detections are shown and discussed in Sections 4.2 and 4.3, respectively. The complete figure set (19 images) is available online at [Factor & Kraus \(2022\)](#).

of calibrators (with significant detections) in position and contrast within 5 and 1 times the  $1\sigma$  error bars in the fits, respectively. These limits were selected in order to maximize the number of known companions we recover while minimizing the number of spurious detections. Decreasing the number of calibrators which a companion must be significantly detected in adds spurious detections, all of which are detections in only a single filter. Increasing the precision with which fits using different calibrators must be consistent with each other eliminates detections which we know are real from the literature. The fact that the positional error bars must be inflated while the contrast error bars do not suggests that the calibration uncertainty is much larger with respect to the statistical uncertainty in position than in contrast. [Ceau et al. \(2019\)](#) also discuss a hypothesis testing framework which we discuss further in Section 5.3.

### 3.4. Bayesian Model Comparison

Since we are using PyMultiNest to fit our data, we also calculate the Bayesian evidence for the single and double point source models. This value can be used to compare the two models in a purely Bayesian manner, irrelevant of the best fit parameter values. Bayes’s theorem (including the hypothesis along with the parameters) states

$$P(\theta|D, H) = \frac{P(D|\theta, H)P(\theta|H)}{P(D|H)}, \quad (6)$$

where  $\theta$  is the model parameters,  $D$  is the data,  $H$  is the hypothesis (or specific model),  $P(\theta|D, H)$  is the posterior,  $P(D|\theta, H)$  is the likelihood,  $P(\theta|H)$  is the prior, and  $P(D|H)$  is the Bayesian evidence. The Bayesian evidence can be thought of as a normalization factor for the numerator, since the posterior distribution must integrate to 1. The Bayesian evidence is ignored by typical MCMC routines, since the integral (over all parameter values) is difficult to perform, and thus the equality is reduced to a proportionality. Since nested sampling algorithms (e.g. [Buchner et al. 2014](#)) sample the entire prior volume, they can calculate the Bayesian evidence. The ratio of the Bayesian evidence for two different models, called the Bayes factor, can then be used to compare two different models.

A histogram of Bayes factors (represented by the symbol  $K$ ) for all of our targets is shown in Figure 8 color coded by our detection method described in Section 3.3. We distinguish between single targets, confident detections, confident detections in only one filter, a marginal detection, and undetected targets with wide separation companions (which KPI is insensitive to).

[Jeffreys \(1961\)](#) set out guidelines for how to interpret  $K$  ranging from  $K < 1$  supporting the single model to  $K > 100$  indicating “decisive” evidence for a binary. This scale does not match well with our calculated values as all but one source strongly supports the binary model. While we do see a significant difference in  $K$  between binaries and single sources, the differentiating value is much larger than [Jeffreys \(1961\)](#) set out. This may be due to the large number of data-points we are fitting.

A few sources which we designated as binaries had small  $K$  values and a few which we designated as single had large  $K$  values. These sources are discussed further in Section 5.3 and are known shortcomings of the available datasets and KP analysis in general.

## 4. RESULTS

We have detected companions in 21 observations corresponding to 19 binaries (two targets were observed twice) in our sample of 114 targets. We confirm one of the new kernel-phase detections presented in [Pope et al. \(2013\)](#), and marginally recover a second, but none of their other “confident”

## 2M 0144-0716 (Prog. ID: 10143)

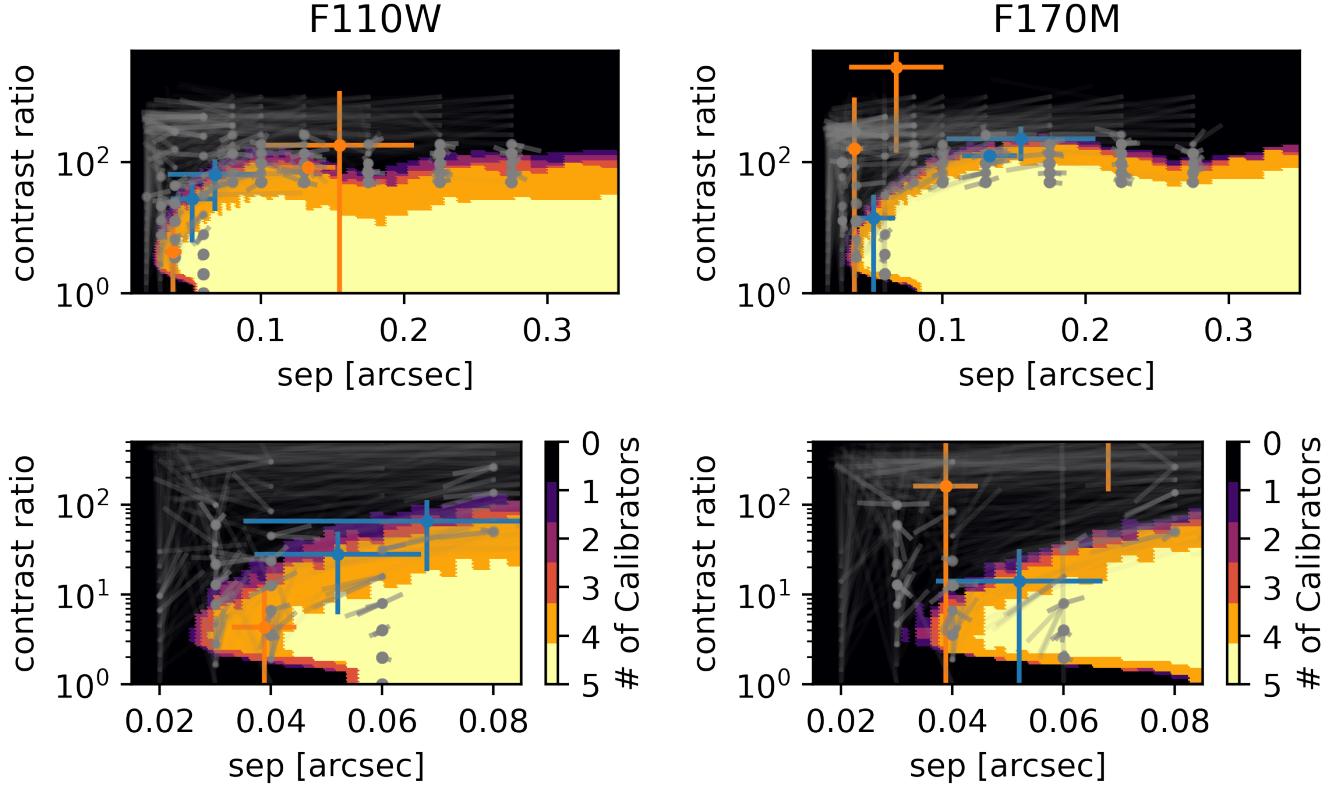


**Figure 5.** Example detection limits on a source with no companion detected. The color scale is the number of calibrators which would significantly ( $> 5\sigma$ ) detect a companion as a function of separation and contrast ratio in the two filters (*left* and *right* columns). The *top row* shows the full range of separation, while the *bottom row* zooms in on the extremely close separation regime where there is a decrease in sensitivity to equal brightness companions (due to a decrease in asymmetry). Best fit companion parameters are plotted (with error bars) for the 5 calibrators in blue, if significantly detected, and in orange, if not significantly detected. In this case  $< 4$  calibrators produce a significant detection and the parameters (including PA) are not consistent with each other so no companion is detected. Overlaid in gray are the results of an injection-recovery test. The injected source is indicated by a circle and is connected to the recovered parameters by a line. Symbol size and opacity is scaled by the proximity of the injected and recovered parameters. Similar plots for the other single sources are shown in Figure Set 5. The complete figure set (83 images) is available online at [Factor & Kraus \(2022\)](#).

or “marginal” detections. Even with our increased sensitivity at extremely close separations, we do not detect any new companions. Astrometry and photometry for the companions is presented in Table 3. Posteriors, kernel-phase correlation plots, and postage stamp images for each target are shown in Figure 4 and the corresponding Figure Set. Our sample also includes 2 wide binaries which KPI is not sensitive to and thus we do not recover, as well as two observations of a suspected extremely tight binary which we do not recover a companion in (see Section 4.4).

## 4.1. Known Binaries



## 2M 2351-2537 (Prog. ID: 10143)

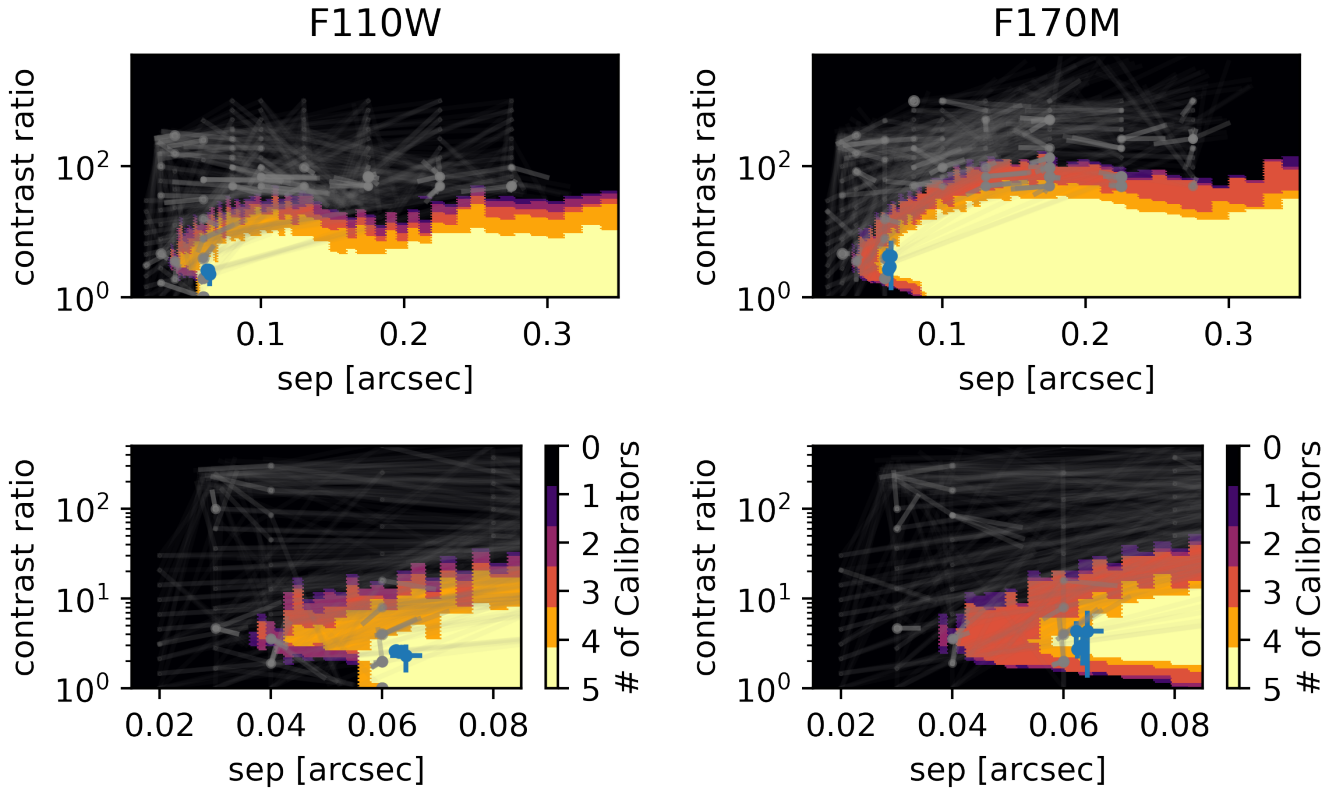


**Figure 6.** Similar to Figure 5 but for a significantly detected source. In this case all calibrators produce significant detections and the best fit parameters are consistent with each other. Similar plots for significant detections are shown in Figure Set 6. The complete figure set (19 images) is available online at [Factor & Kraus \(2022\)](#).

We find that 12 sources agree well with previously published astrometry and photometry. This includes **2M 2351-2537**, one of the new extremely tight ( $62.7$  mas,  $0.4\lambda/D$  in F110W and  $0.66\lambda/D$  in F170M) binaries discovered using KPI by [Pope et al. \(2013\)](#). We discuss the remaining sources below, which have some discrepancy. No previously published astrometry and photometry could be found for the NICMOS imaging of **2M 1534+1615** from program 11136 ([Liu 2007](#)) though our fits visually agree with the position of the companion in the images.

The companion to **2M 0004-4044** is not detected in the F170M filter. This target is a tight ( $\sim 0.5\lambda/D$ ) equal brightness target which KPI is less sensitive to (since the system lacks asymmetry). The companion is however detected in the F110W filter where the diffraction limit is smaller. [Pope et al. \(2013\)](#) fit the full visibilities (rather than just the kernel phases) for this target to increase the sensitivity to the low-contrast companion. Our best fit parameters are slightly tighter and fainter than those of [Pope et al. \(2013\)](#), perpendicular to the contrast-separation degeneracy seen in tight-separation fits.

**2M 0025+4759** is slightly wider than the best fit parameters from [Pope et al. \(2013\)](#). Our contrast in F110W is consistent but our F170M contrast ( $C_{F170M} = 1.25 \pm 0.02$ ) is slightly higher than both

## 2M 0314+1603 (Prog. ID: 10143)

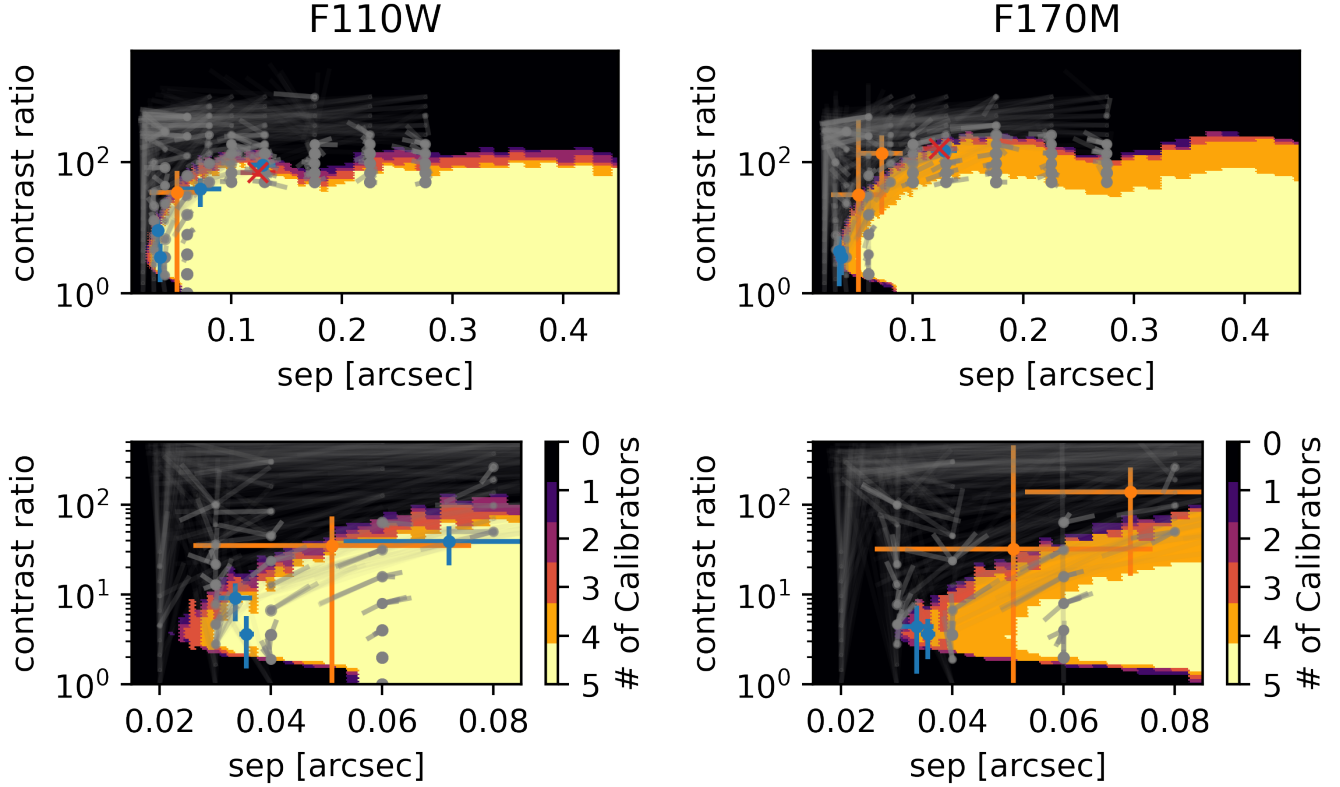


**Figure 7.** Similar to Figure 5 but for a notable non-detection. In this case 2M 0314+1603 was marginally detected by Pope et al. (2013). Their best fit parameters are indicated by the red X. One of our calibrators roughly recovers their values but they are not consistent between enough calibrators to consider this detection significant. Similar plots for notable non-detections are shown in Figure Set 7. The complete figure set (11 images) is available online at Factor & Kraus (2022).

Pope et al. (2013) ( $C_{F170M} = 1.03 \pm 0.04$ ) and Reid et al. (2006) ( $C_{F170M} = 1.11$ ). Pope et al. (2013) also fit the visibilities of this roughly equal brightness source rather than the kernel phases since they knew it was a low-contrast companion.

**2M 0423-0414** was observed by both Burgasser et al. (2006b) and Liu (2007). We detect the companion in F170M in both epochs but in F110W in only one epoch. The companion is much tighter in the second epoch and the observations are much lower SNR so it is not surprising that we do not detect it in the shorter wavelength filter. Our astrometry and photometry is consistent with that presented by Dupuy & Liu (2017) though we do pick up some separation-contrast degeneracy in the later, close-separation epoch (our separation is slightly tighter and contrast slightly higher). Dupuy & Liu (2017) also derived a dynamical mass for this system from its orbital motion in these and other *HST/ACS* observations.

**2M 0429-3123** is just wider than the upper edge of our detection limit grid but the best fit parameters are consistent between calibrators and agree with literature values. We thus consider this a significant detection. Our best fit separation ( $534 \pm 4$  mas) splits the difference in separation

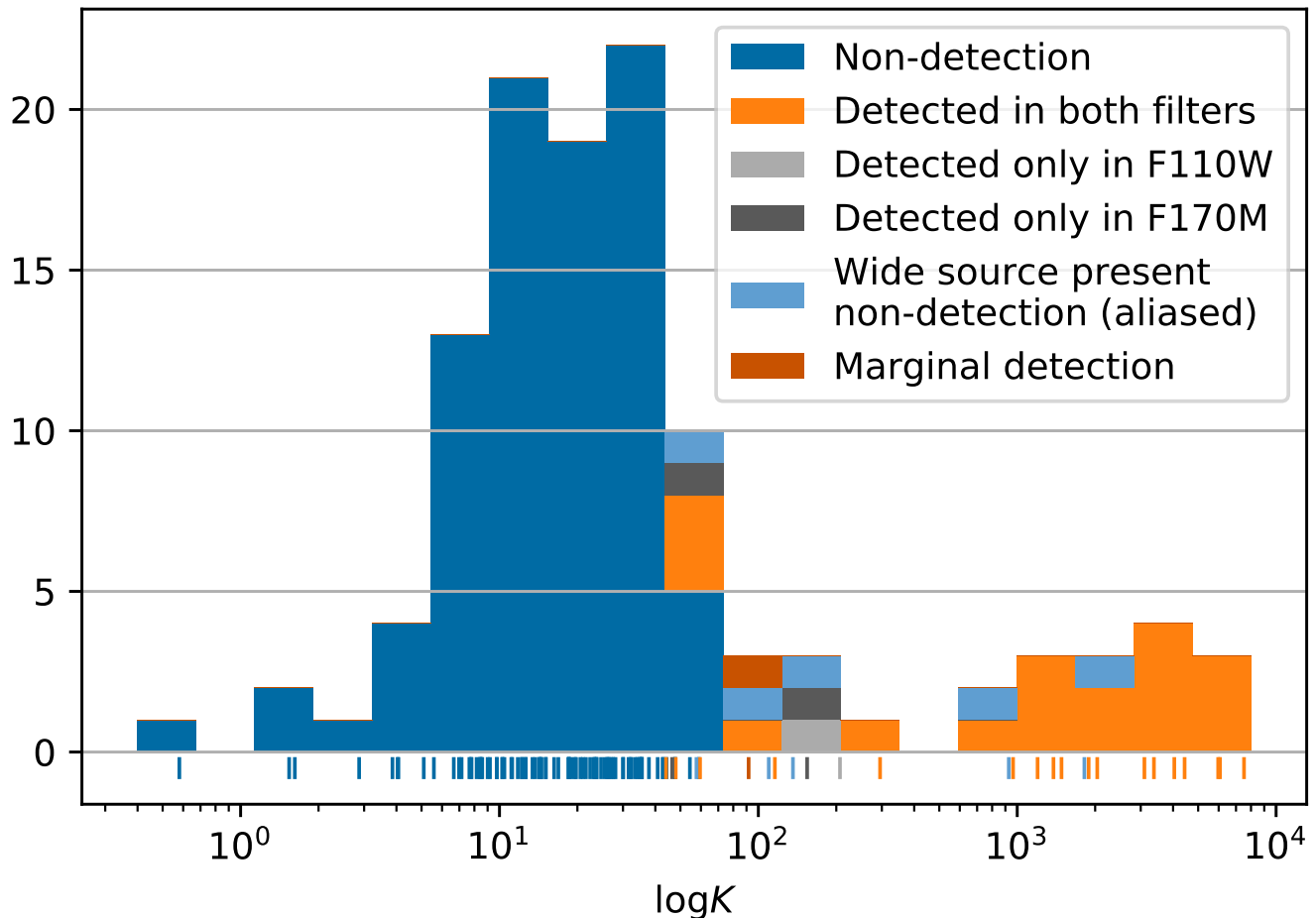


**Figure 8.** Histogram of Bayes factors (median value for the 5 calibrators) for the 117 observations in our sample, color coded by the assessment from our scramble and fit detection method. True (un-binned) positions are indicated with dashes under the histogram. Individual targets are discussed in Section 5.3.

between Reid et al. (2006) (550 mas) and Pope et al. (2013) ( $525.2 \pm 1.2$  mas) while our contrast is consistent.

**2M 0926+5847** is consistent with Burgasser et al. (2006b) with the exception of F170M (they report  $C_{F170M} = 1.4 \pm 0.4$  while we report  $C_{F170M} = 2.70 \pm 0.28$ ). Our F170M contrast value is more consistent with Dupuy & Liu (2017,  $C_{F170} = 2.2 \pm 0.2$ ), though still slightly higher contrast. KPI is much more precise than PSF fitting at the separation of this companion ( $67.22 \pm 0.14$  mas) and our contrast values are consistent with the color/spectral type relations of T dwarfs (Leggett et al. 2002).

**SDSS 2052-1609** was observed at low SNR in program 11136 (Liu 2007). Our separation and position angle agree with Dupuy & Liu (2017) with higher precision though our best fit F110W contrast ( $C_{F110W} = 4.4 \pm 0.7$ ) is significantly higher than theirs ( $C_{F110W} = 1.2 \pm 0.4$ ). Our high contrast F110W fit does not seem consistent with the images even though this target should be easily recovered by KPI. It is possible that the super-Gaussian window we used to exclude noise far away from the target is too wide ( $\sigma = 25\lambda/D$ ) for these low SNR observations where the wings of

**Table 3.** Binary astrometry & photometry

Source	Sep. [mas]	$\sigma_{\text{sys,sep}}$ [mas]	PA [deg]	$\sigma_{\text{sys,PA}}$ [deg]	F110W contrast	$\sigma_{\text{sys,F110W}}$	F170M contrast	$\sigma_{\text{sysF170M}}$
2M 0004-4044	$83.2 \pm 0.5$	0.12	$44.3 \pm 0.6$	0.4	$1.126 \pm 0.018$	0.004		
2M 0025+4759	$334.5 \pm 0.9$	0.05	$232.79 \pm 0.13$	0.005	$1.353 \pm 0.033$	0.0030	$1.251 \pm 0.023$	0.0010
2M 0147-4954	$138.8 \pm 0.4$	0.9	$72.64 \pm 0.14$	0.20	$2.345 \pm 0.030$	0.22	$2.022 \pm 0.016$	0.08
2M 0423-0414 <sup>1</sup>	$159.11 \pm 0.24$	0.15	$19.77 \pm 0.08$	0.05	$1.655 \pm 0.011$	0.015	$2.124 \pm 0.010$	0.007
2M 0423-0414 <sup>2</sup>	$83.1 \pm 0.7$	0.8	$183.1 \pm 0.8$	0.4			$2.06 \pm 0.23$	0.25
2M 0429-3123 <sup>3</sup>	$534 \pm 4$	0.17	$285.2 \pm 0.4$	0.016	$3.50 \pm 0.23$	0.010	$2.77 \pm 0.13$	0.004
2M 0700+3157	$179.4 \pm 0.7$	0.8	$105.68 \pm 0.18$	0.23	$4.43 \pm 0.12$	0.28	$3.809 \pm 0.033$	0.06
2M 0850+1057	$132.2 \pm 0.7$	0.4	$128.11 \pm 0.20$	0.16	$2.93 \pm 0.05$	0.023	$2.423 \pm 0.031$	0.018
2M 0926+5847	$67.22 \pm 0.14$	0.4	$134.26 \pm 0.28$	0.5	$1.522 \pm 0.018$	0.005	$2.70 \pm 0.28$	0.06
2M 1021-0304	$166.4 \pm 0.5$	1.4	$244.83 \pm 0.13$	0.19	$1.104 \pm 0.014$	0.006	$2.516 \pm 0.015$	0.07
2M 1534+1615	$114 \pm 4$	1.3	$310.6 \pm 1.6$	0.6	$2.96 \pm 0.35$	0.09	$2.55 \pm 0.27$	0.07
2M 1553+1532	$345.7 \pm 0.7$	0.7	$189.69 \pm 0.13$	0.13	$1.363 \pm 0.034$	0.014	$1.408 \pm 0.027$	0.004
2M 1728+3948	$157.75 \pm 0.28$	0.13	$66.73 \pm 0.10$	0.05	$1.390 \pm 0.018$	0.0011	$1.535 \pm 0.007$	0.0031
SDSS 2052-1609	$102.1 \pm 0.9$	0.11	$48.5 \pm 1.1$	0.6	$4.4 \pm 0.7$	0.14	$1.72 \pm 0.09$	0.04
2M 2152+0937	$254.2 \pm 0.6$	0.034	$94.31 \pm 0.18$	0.009	$1.157 \pm 0.019$	0.0007	$1.126 \pm 0.012$	0.0005
2M 2252-1730 <sup>4</sup>	$126.7 \pm 0.7$	0.9	$353.96 \pm 0.17$	0.6	$2.568 \pm 0.028$	0.027	$3.21 \pm 0.04$	0.32
2M 2252-1730 <sup>5</sup>	$91.9 \pm 1.9$	2.0	$172.9 \pm 0.6$	0.7	$5.8 \pm 0.7$	0.14	$3.3 \pm 0.4$	0.5
2M 2255-5713	$178.3 \pm 0.8$	0.27	$172.64 \pm 0.22$	0.24	$5.16 \pm 0.14$	0.19	$4.53 \pm 0.06$	0.10
2M 2351-2537	$62.65 \pm 0.34$	0.5	$348.74 \pm 0.28$	0.8	$2.58 \pm 0.09$	0.13	$2.9 \pm 0.9$	0.7
Marginal (see section 4.2)								
2M 2028+0052	$39.0 \pm 3.3$	4	$118.3 \pm 1.0$	7	$1.7 \pm 3.2$	3.5		
Spurious (see section 4.3)								
2M 0024-0158	$202 \pm 9$	10	$33.4 \pm 1.3$	1.8			$121 \pm 11$	8
2M 0205-1159	$106.0 \pm 0.6$	0.07	$349.8 \pm 1.0$	0.32	$1.75 \pm 0.09$	0.012	$1.122 \pm 0.023$	0.008
2M 2204-5646	$127.9 \pm 2.3$	0.34	$310.7 \pm 2.1$	1.8	$3.02 \pm 0.28$	0.14	$5.2 \pm 0.4$	0.4

NOTE—1: Observations from program 9833 (7/2004) 2: Observations from program 11136 (8/2008) 3: 2M 0429-3123 is just wider separation than the grid used for detection limits but fitted parameters agree with literature values (see discussion of this source in Section 4.1). 4: Observations from program 10143 (6/2005) 5: Observations from program 11136 (5/2008)

the PSF are not present. Orbital motion is seen between this and other observations and was fit by Dupuy & Liu (2017).

**2M 2252-1730** was observed by Reid et al. (2006) and later by Liu (2007). Our best fit parameters are consistent with the Reid et al. (2006) and Pope et al. (2013) epoch while we pick up some separation-contrast degeneracy in the later Liu (2007) epoch. Our values (sep =  $91.9 \pm 1.9$  mas,  $C_{\text{F110W}} = 5.8 \pm 0.7$ ) are slightly wider and significantly higher contrast than those presented by Dupuy & Liu (2017) (sep =  $87 \pm 3$  mas,  $C_{\text{F110W}} = 1.9 \pm 0.7$ ). As with **SDSS 2052-1609**, our high contrast F110W fit is likely caused by too wide of a super-Gaussian window. Orbital motion is seen between the two epochs and was fit by Dupuy & Liu (2017).

#### 4.2. Marginal Detection

**2M 2028+0052** is not detected in F170M and just barely fails to pass our confidence test in F110W. While four of five calibrators produce fits which are well grouped, one pair of calibrators is inconsistent with each other in position at  $5.16\sigma$  (just above our  $5\sigma$  cutoff) and another pair is inconsistent with each other in contrast at  $1.07\sigma$  (just above our  $1\sigma$  cutoff). This target also has a slightly elevated Bayes Factor with respect to sources we categorize as single. We thus present this as a marginal detection. Adding more calibrators and a more careful treatment of bad pixels, thus

## 2M 2028+0052 (Prog. ID: 10879)

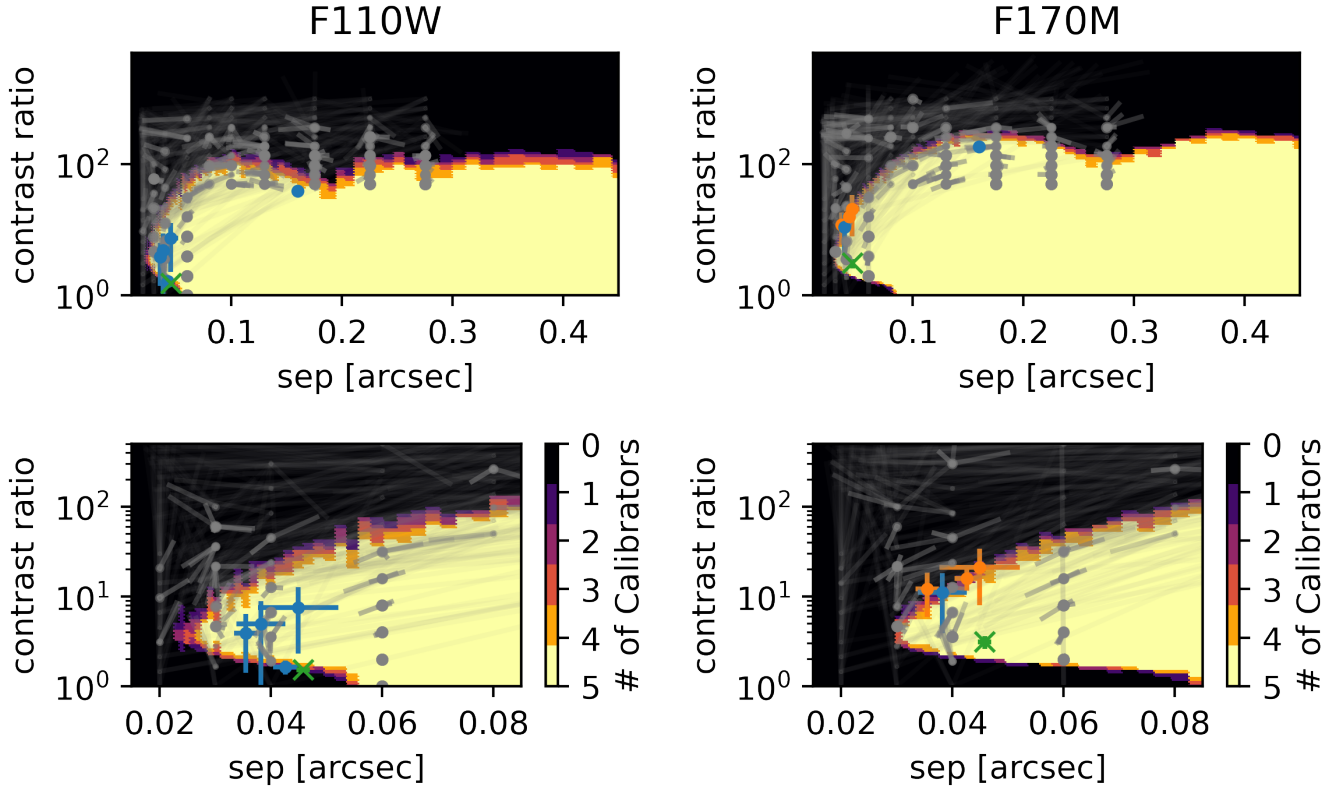


**Figure 9.** Similar to Figure 5 but for the marginal detection of 2M 2028+0052. The best fit parameters from Pope et al. (2013) are indicated by the green X. Similar plots for the spurious detections are shown in Figure Set 9. The full figure set (4 images) is available online at Factor & Kraus (2022).

reducing the noise, will help to refine this determination. It also has an elevated RUWE (1.418; Gaia Collaboration 2020), even when fitting for the astrometric color (Lindgren et al. 2021), suggesting the presence of a companion. Dahn et al. (2017) also notes elevated and periodic ( $\lesssim 2$  years) residuals in their parallax solution.

Our best fit parameters are consistent with those of Pope et al. (2013), when considering the intercalibrator systematic error-bars. Our best fit parameters are heavily weighted toward a single higher precision fit, while the fits using the other calibrators are much lower precision (as can be seen in the detection limit plot shown in Figure 9. Figure 10 shows the corner plot for the high precision fit. There appears to be a small bump in the posterior at a lower contrast in F170M which may be consistent with the Pope et al. (2013) contrast.

#### 4.3. Spurious Detections

We detect a high contrast “companion” around 2M 0024-0158 in F170M but with no detection in F110W. Figure 11 shows the corner plot, kernel-phase correlation plots, and a representative image for this target. Visual inspection of the images and associated data-quality frames demonstrates that this detection is spurious. The position of the detection almost exactly lines up with bad pixels

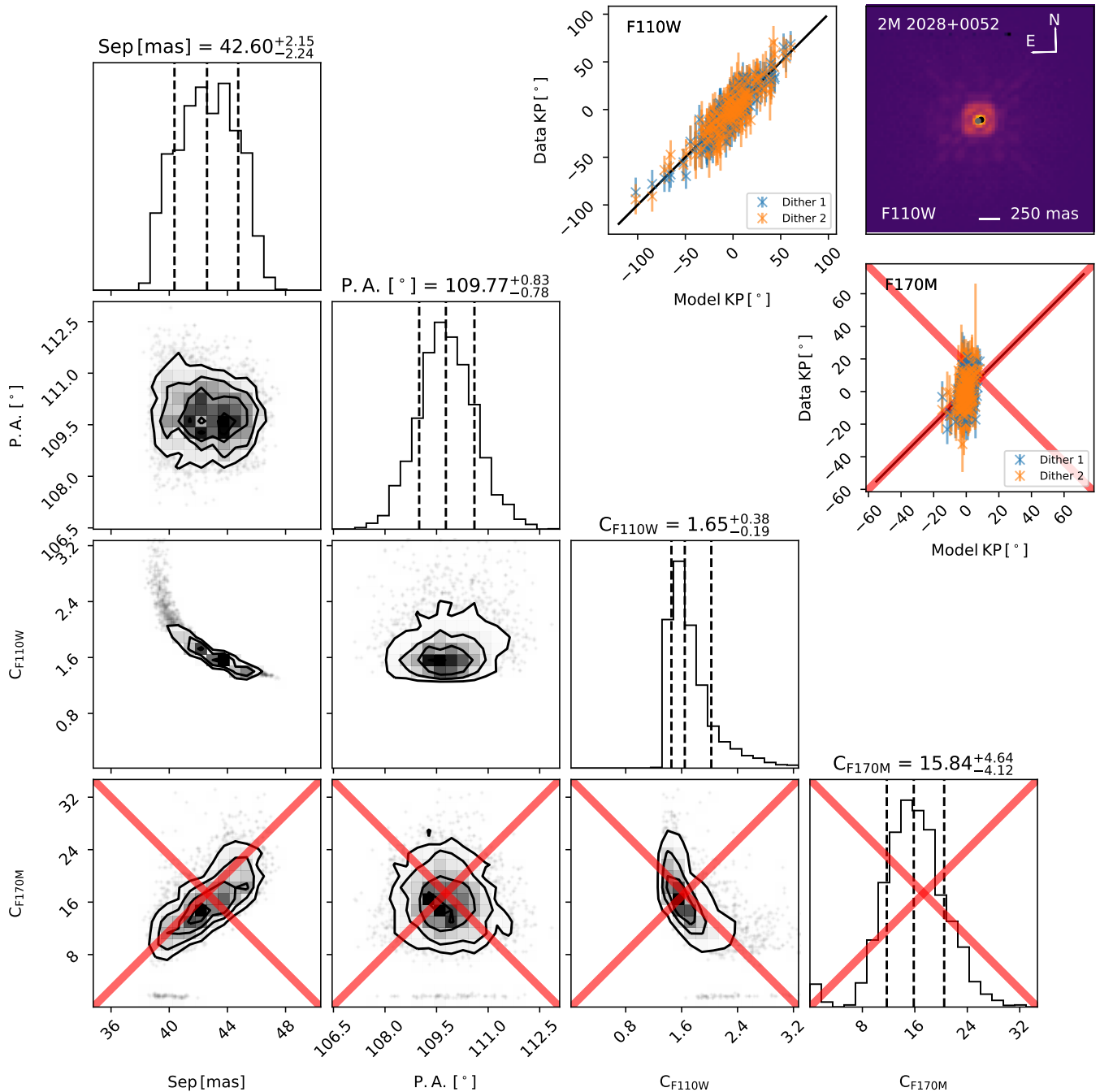


**Figure 10.** Similar to Figure 4 but for the marginal detection of 2MASS 2028+0052. Red X's indicate no detection in F170M.

which were coincidentally located at the same position, relative to the target, in both dither positions. Our bad-pixel correction technique (replacing the pixel with the median of the 8 surrounding pixels) injected a brighter than expected pixel in the F170M images, since it fell in the first dark airy ring. This pixel was then interpreted as a companion. In the F110W images the bad pixel fell in the first bright airy ring and did not inject the signal of a companion. This can be seen in Figure 12. We present this case as a cautionary tale to show how image-plane based bad-pixel rejection routines can

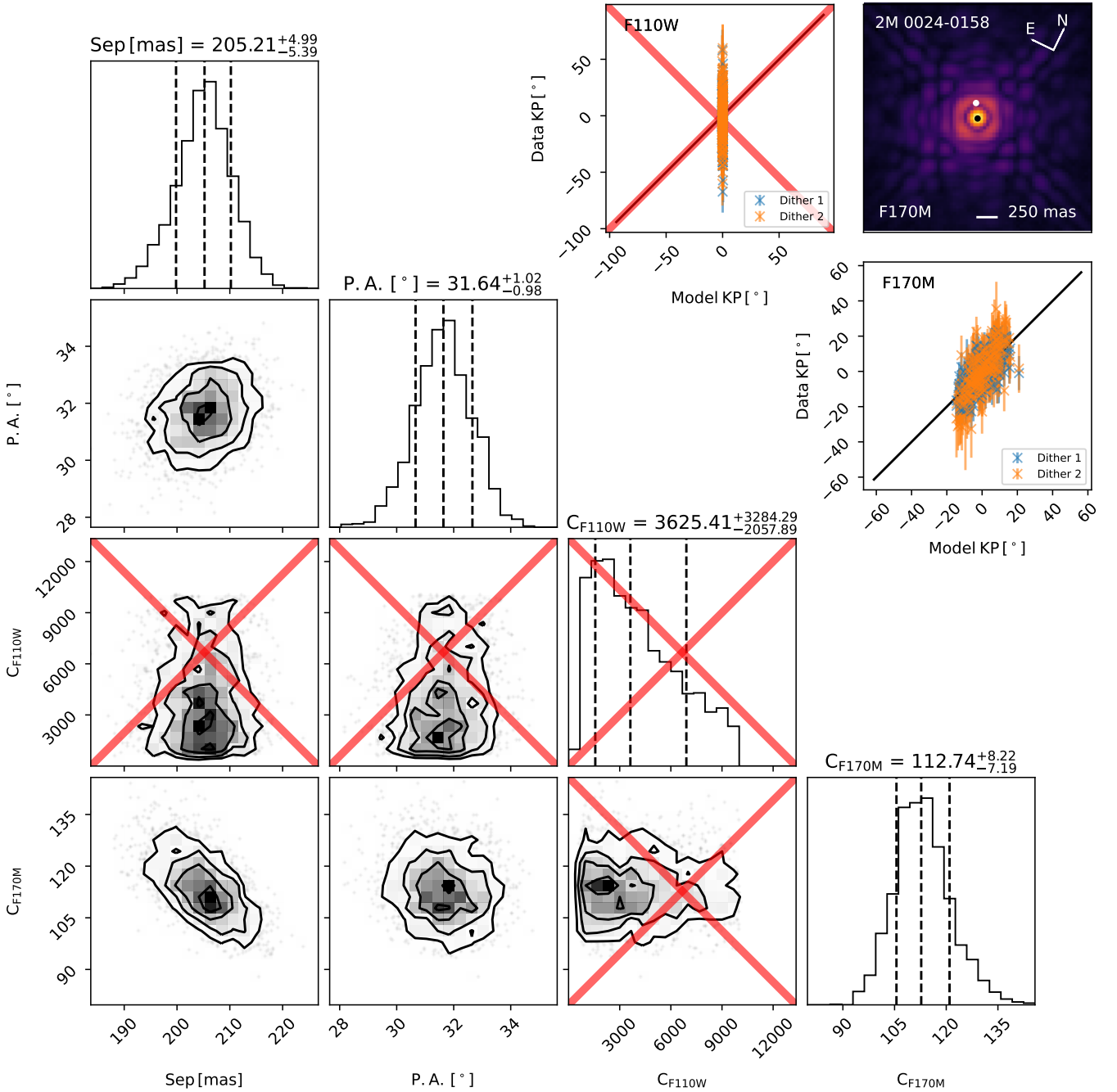


**Figure 11.** Similar to Figure 4 but for 2MASS 0024-0158. Large red X's over the 1- and 2D histograms indicate no detection in the F110W filter. This fit locked onto the signal produced by a bad pixel.

inject signals in the Fourier plane. In the future, bad-pixel rejection techniques in the Fourier plane should be used as described by Ireland (2013) and implemented in Kammerer et al. (2019).

A simple visual inspection of the fits to **2M 0205-1159** and **2M 2204-5646**, shown in Figures 13 and 14, shows a clear discrepancy between the visually obvious companion and the best fit parameters. Both of these targets were observed in program 11136 which observed using a large number of filters, sacrificing SNR for more wavelength coverage. Therefore, while the core of the PSFs are clear, little

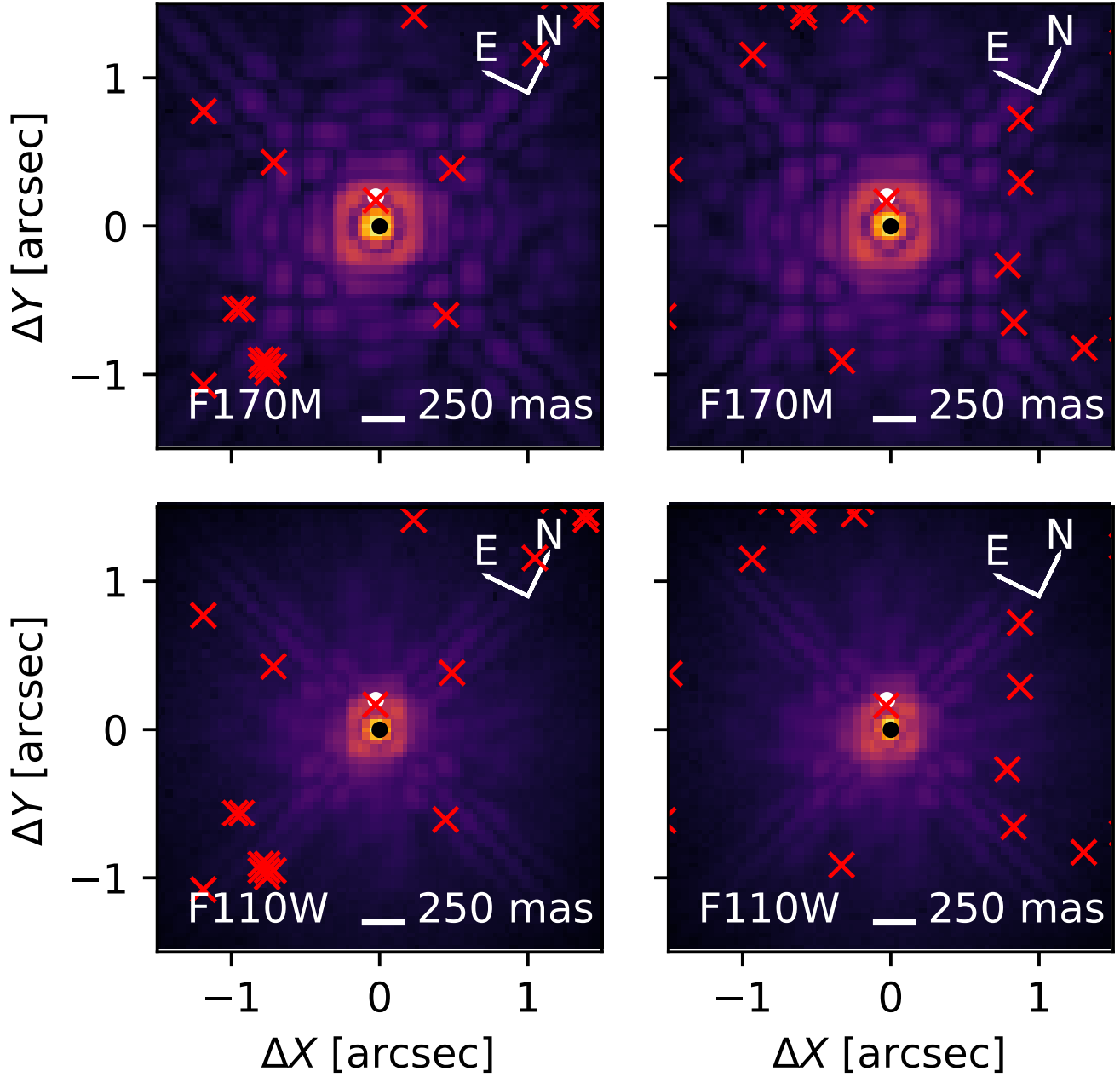


**Figure 12.** Both filter and dither position images of 2M 0024-0158. The location of the primary is indicated by a black circle and the location of the best fit “companion” is shown by a white circle. The locations of bad pixels are indicated with red X’s. Note that in both dither positions there is a bad pixel at almost exactly the same location relative to the target and that in F170M the bad pixel is located in the first dark ring while in F110W it is located in the first bright ring. Our bad-pixel rejection imperfectly replaced the bad pixel on the dark ring and yielded a spurious faint detection in F170M.



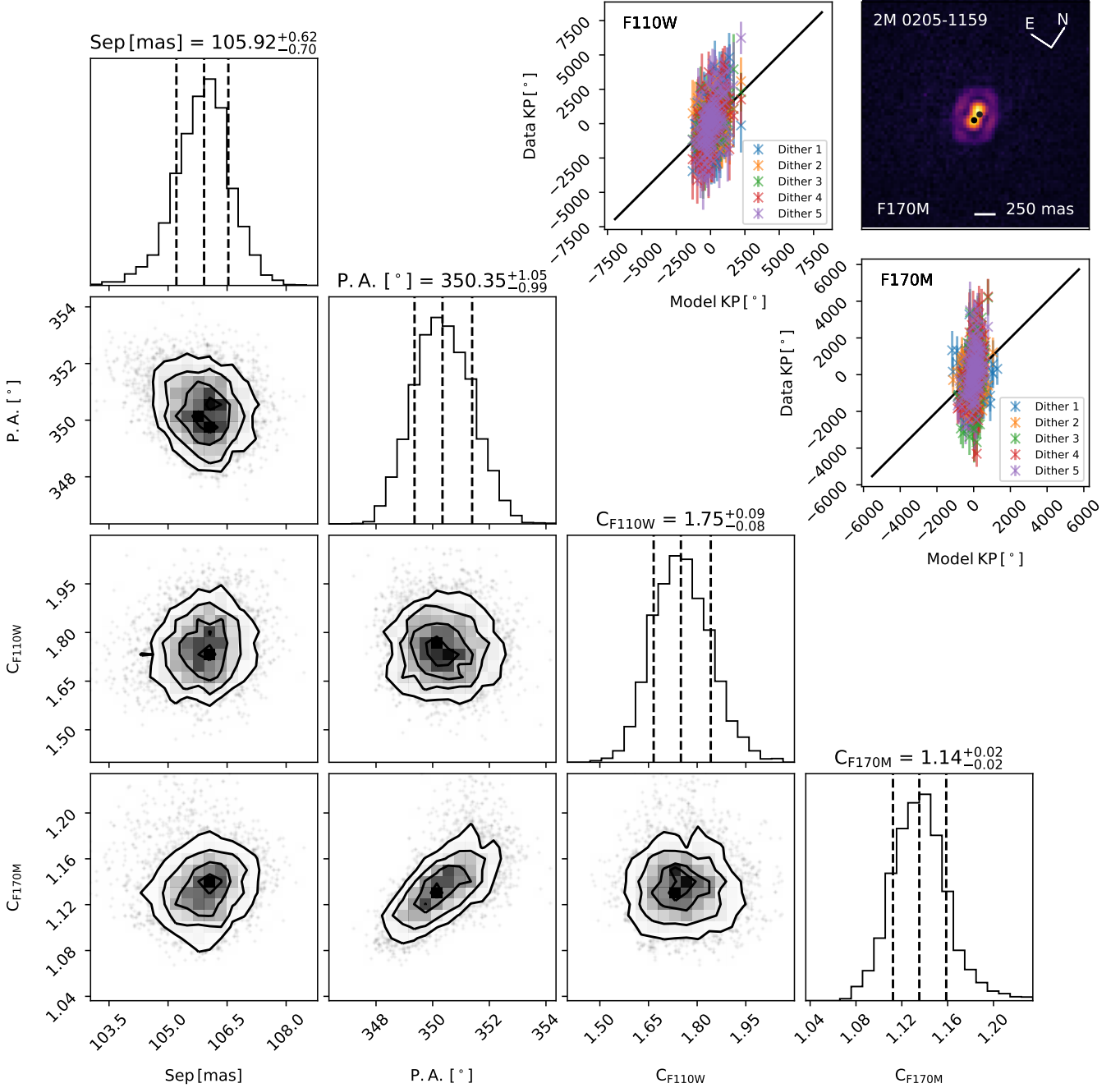


**Figure 13.** Similar to Figure 4 but for the spurious fit to 2MASS 0205-1159. This source is a triple system and thus is not well fit with a binary model.

to none of the wings of the diffraction pattern is recovered. While we present our best fit parameters for completeness of the survey, we will give these sources a more careful treatment in a future letter. In addition, **2M 0205-1159** is a previously known triple system (Bouy et al. 2005). The position and contrast of our best fit companion is likely a combination of the B and C components. Fitting this system with a triple point source model will be done in a future letter as the addition of a third source adds nontrivial degeneracies in the model.

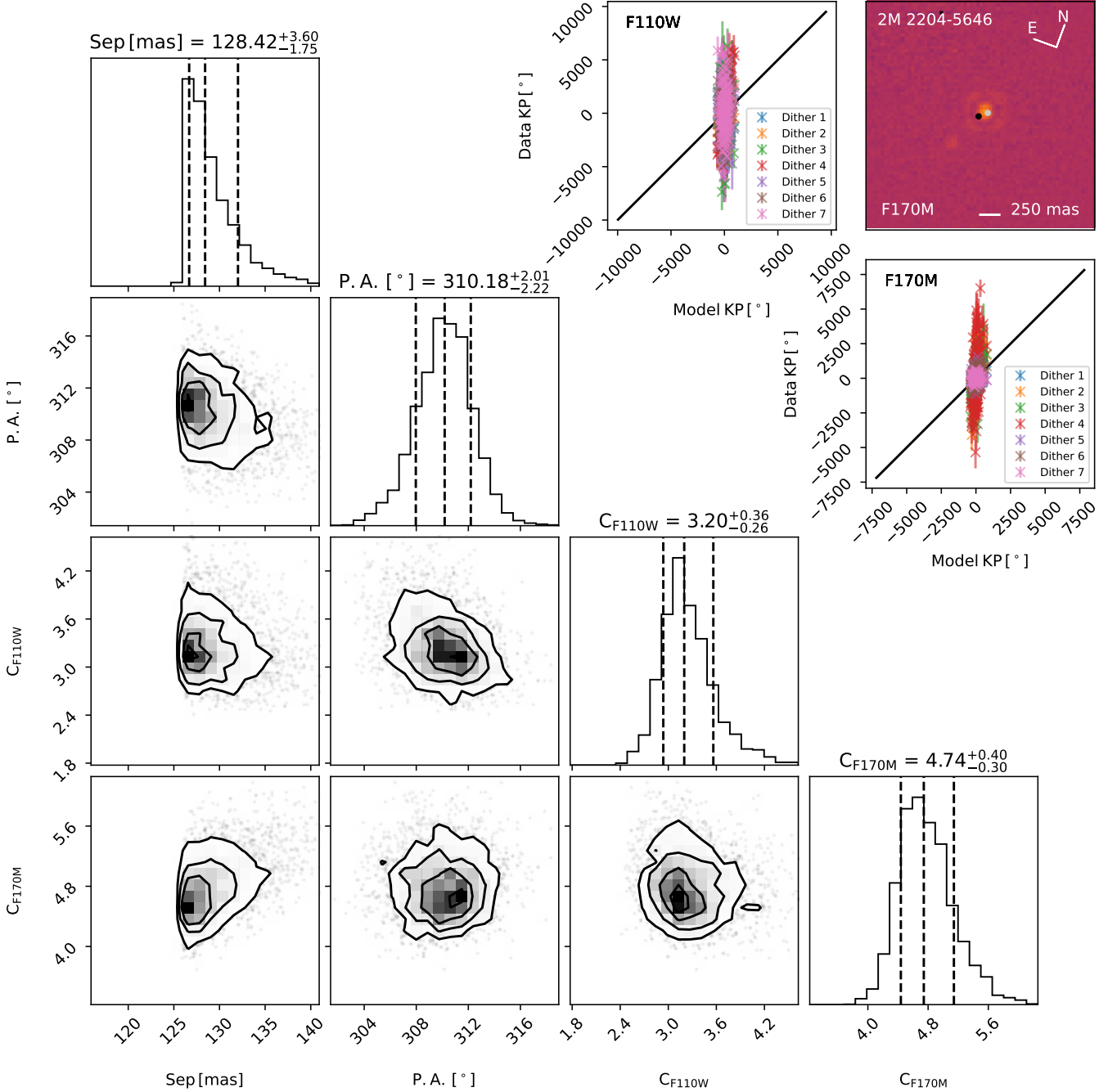


**Figure 14.** Similar to Figure 4 but for 2MASS 2204-5646. Our binary model did not recover the true values of the wide companion in this low SNR observation.

#### 4.4. Notable Non-detections

We do not significantly detect any of the marginal detections presented in Pope et al. (2013) and only detect two of their five confident detections (2M 2351-2537 significantly and 2M 2028+0052 marginally, discussed above). While some of our best fit parameters with a *single* calibrator are consistent with their results and that single fit may be significant (e.g. 2M 0314+1603 and 2M 1936-5502), they are not consistent between multiple calibrators (see Figure 7 and the relevant figure in

Figure Set 7) and we therefore do not classify them as detections. This demonstrates the strength of and need for a robust calibration strategy. Due to the extreme separation of these proposed companions, a ground-truth validation of these companions is difficult though not impossible. Possible techniques include LGSAO on a large ground based telescope or astrometry (e.g. future work of [Gaia Collaboration et al. 2021](#); [Dahn et al. 2017](#)). While binary fits are still not part of Gaia data releases, RUWE can be used as a proxy for the presence of a companion ([Lindgren et al. 2018](#); [Belokurov et al. 2020](#); [Lindgren et al. 2021](#), Kraus et al. in prep.). All of the marginal and confident detections (with the exception of the two sources we recover) have RUWE of  $\sim 1$  ([Gaia Collaboration 2020](#)). If these companions are real we would expect them to have an elevated RUWE like **2M 2351-2537** (RUWE = 5.417), though equal brightness companions have less of an astrometric signal and faint targets have inherently more noise.

It is also difficult for our implementation of KPI to recover wide companions at separations greater than  $\sim 0.6$  arcsec accurately. These companions suffer from aliasing in the Fourier plane as sampled by our aperture model and do not require high resolution where KPI excels. Since these companions are generally noticeable under visual inspection, one could tune the prior to isolate the true signal from aliases but it would be more straightforward to use classical PSF fitting techniques.

**2M 0915+0422** is a wide separation companion ( $738.6 \pm 0.15$  mas [Pope et al. 2013](#)) and thus our pipeline is strongly affected by aliasing in the Fourier plane. Our fits do not recover the literature values for this companion. We do detect a significant companion but at an alias of the known companion.

**2M 1707-0558** is also a wide separation companion ( $1009.5 \pm 1$  mas; [Pope et al. 2013](#)) and again our pipeline is strongly affected by aliasing in the Fourier plane. We do recover the companion in two of five calibrators but the aliasing is strongly affecting our best fit parameters so we do not present them here. Our best fit separation is slightly wider than both [Reid et al. \(2006\)](#) and [Pope et al. \(2013\)](#) though our contrasts are more consistent with [Reid et al. \(2006\)](#).

**2M 1705+0516** and **2M 1731+2721** both have wide objects in the images that, based on color and follow up observations (Dupuy, private communication), appear to be background sources.

We do not detect a companion to **2M 0518-2828** in either of the two epochs (programs 10247 and 11136). [Cruz et al. \(2004\)](#) published the near infrared spectrum of this object which had features of both an L and T dwarf, suggesting that it was an unresolved binary. [Burgasser et al. \(2006b\)](#) then published *HST/NICMOS* images of this target and found that the PSF was “slightly elongated”, more so in the shorter wavelength filters. The elongation is extremely small in F110W and absent in F170M so our non-detection is not unexpected. [Burgasser et al. \(2006b\)](#) measured a separation of  $51 \pm 12$  mas and a contrast of  $C_{F110W} = 2.1 \pm 1.0$  ( $0.8 \pm 0.5$  mag) and  $C_{F170M} = 2.3 \pm 1.3$  ( $0.9 \pm 0.6$  mag). The separation is what is limiting us in this case as, for context, it is roughly 10 mas tighter than **2M 2351-2537** at slightly lower contrast. If KPI can be done in F090M (larger pixel scale relative to  $\lambda/D$  and larger aberrations relative to  $\lambda$ ) a detection may be possible.

#### 4.5. Survey Detection Limits

A superposition of all detection limits is shown in [Figure 15](#). Detection limits for each target are shown in [Figures 5, 6, and 7](#) and the corresponding Figure Sets, and are summarized in [Tables 4–6](#) at a set of separations. In the best cases, significant detections of companions can be achieved up to a contrast of  $\sim 100 : 1$  and down to a separation of  $\sim 0''.1$ . Below  $\sim 0''.1$  the contrast limit drops steeply and becomes bimodal, with KPI becoming insensitive to equal-brightness companions at extremely

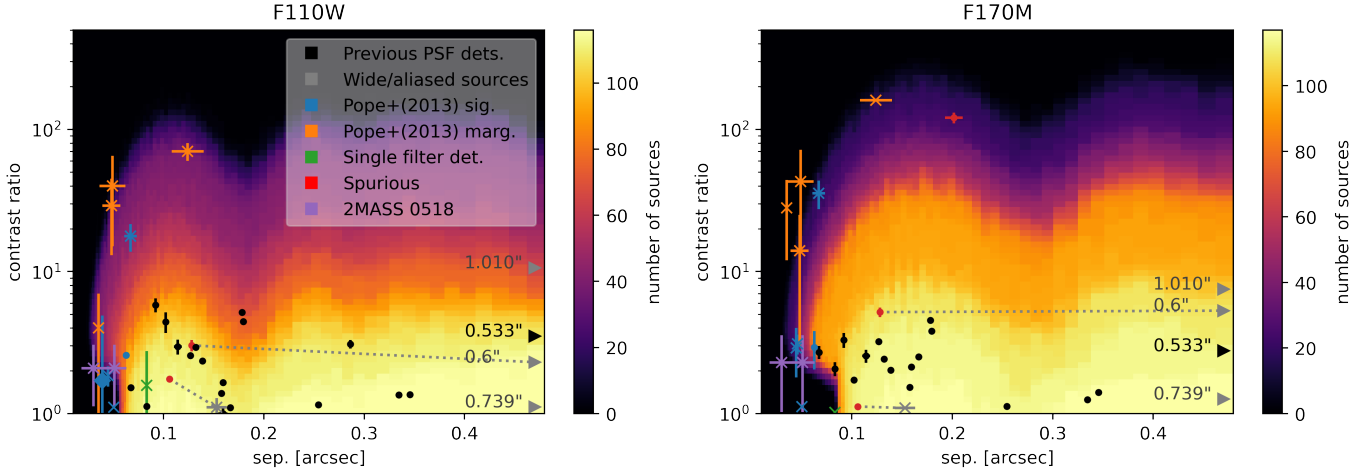


**Figure 15.** Stacked  $5\sigma$  detection limits as a function of separation for all sources in the survey. Filled circles indicate the positions of detected companions, the diamond is our one marginal detection, and X’s indicate literature values for non-detections. Points are color coded by type of detection and are outlined in the legend. Black symbols indicate companions previously found by PSF fitting. Blue and orange symbols indicate the “significant” and “marginal” detections from [Pope et al. \(2013\)](#), respectively. Green X’s indicate the literature contrast values of the two sources (one in each filter) which we only detected in one filter. Red points indicate the positions of “spurious” detections (see Section 4.3) with dotted lines to gray X’s indicating the literature values. Purple symbols indicate the position of 2MASS 0518-2828 (see Section 4.4). Two sources were extremely wide and were not recovered due to strong aliasing and are shown by gray arrows, at a separation given by the labeled text. The survey detection limits in both filters, in units of number of sources, are available as the Data behind the Figure online at [Factor & Kraus \(2022\)](#) or in the .tar.gz file available on arXiv (see README.txt for info on the .fits files).

tight separations due to the loss of asymmetry. A full treatment of the covariance matrix could increase the contrast limits at large separations due to the consideration of photon noise ([Ireland 2013](#)).

Comparing the difference in sensitivity between the two filters, as shown in Figure 16, reveals some clear takeaways. At close separation the shorter wavelength F110W filter is more sensitive since the diffraction limit is smaller. At wider separations observations in the longer wavelength F170M filter are more sensitive since optical aberrations are smaller with respect to the wavelength of light. These two filters also work in harmony by canceling out the dips in sensitivity as the brightness of the airy pattern fluctuates. A detection in two filters is also helpful to discern between real detections and spurious detections (such as for **2M 0024-00158**, caused by a bad pixel).

## 5. DISCUSSION

### 5.1. Binary Frequency

While we present astrometry and photometry for all detections, we must restrict our analysis of binary populations to targets in programs 9833 ([Burgasser et al. 2006b](#)), 10143 ([Reid et al. 2006](#)), and 10879 ([Reid et al. 2008a](#)) and we must exclude programs specifically targeting binaries (9843, 10247, 11136). This removes any bias in our sample toward binarity and enables a study of binary demographics. This brings the total number of objects in our sample down to 106 (from 114). The

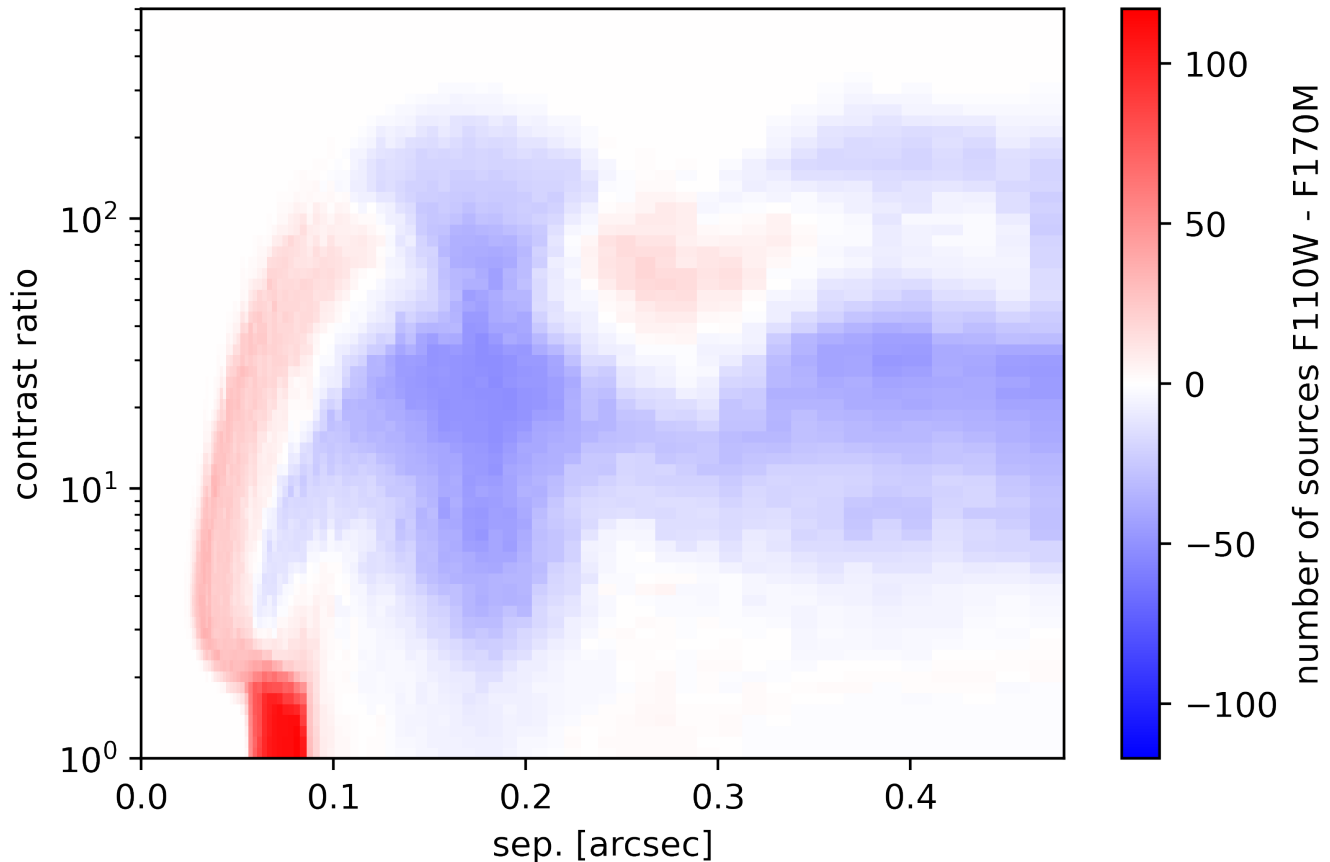


**Figure 16.** The difference in sensitivity between F110W and F170M (given in number of observations our analysis was sensitive to out of a total of 117) as a function of separation and contrast. F110W is more sensitive at close separations where the diffraction limit dominates, while F170M is more sensitive globally since aberrations are smaller with respect to the longer wavelength.

number of binary systems in our statistical sample drops to 15 (from 21) when also accounting for the 2 wide companions which KPI is not sensitive to.

To compare our binary fraction with Reid et al. (2008a) and Pope et al. (2013) we restrict our sample to 20 pc. This is much more straightforward than in the previous studies due to recent parallax surveys (e.g. Gaia Collaboration et al. 2018, 2021; Best et al. 2020). Our total number of sources then drops to 83, including 10 binaries while excluding 5. If we include **2M 0036+1821** and **2M 0355+1133**, which we do not detect companions around but were observed to have companions by Bernat et al. (2010), this number rises to 12/83. Estimating the uncertainty using binomial statistics (Burgasser et al. 2003c) gives a binary fraction of  $\epsilon_b = 14.4^{+4.7}_{-3.0}\%$ . This binary fraction is slightly lower than the number presented in Pope et al. (2013) ( $\epsilon_b = 17.2^{+5.7}_{-3.7}\%$ ) though they are consistent within the quoted errors.

The typical mass of a brown dwarf is significantly lower than the Jeans mass of a collapsing protostellar cloud. Thus two theories for the formation mechanism of brown dwarfs have been proposed: gravoturbulent collapse and embryo ejection (Basu 2012). Since embryo ejection is an energetic event, the binary fraction it produces is small:  $< 5 - 8\%$  (Bate et al. 2002; Bate 2012). Our significantly higher binary fraction, and that of Pope et al. (2013) and other observational studies

(e.g. Reid et al. 2006, 2008a), supports the conclusion that embryo ejection plays a minimal role in brown dwarf formation. A more detailed demographic analysis of the full unbiased sample (not distance limited but still excluding programs targeting binaries) will be presented in a future work using a Bayesian population analysis similar to Allen (2007). The semimajor-axis and mass-ratio distributions will be important to quantify in establishing the companion frequency, especially since all of these quantities are covariant when considering typical detection limits.

### 5.2. Implications for Dynamical Mass Measurements

Our sample includes three targets which were observed twice. We detect companions around two of these sources and see orbital motion between the two epochs. Our astrometry for these two sources and six other sources with only one epoch is consistent with Dupuy & Liu (2017) though our fits are much higher precision. Two other sources are listed in Table 3 of Dupuy & Liu (2017) which have *HST/NICMOS* imaging, though in filters other than F110W and F170M. These sources, along with others with relevant imaging in other filters will be analyzed in a future letter. Since no specific observing set up is required for KPI (unlike NRM observations), KPI is a particularly powerful tool for resolving binary orbits since it allows precovery of relative astrometry and photometry from archival observations of known binaries even when the binary was undetected or had much larger uncertainties when studied with image-plane analysis techniques.

### 5.3. Scramble and fit detection limits vs. Bayes factors

One caveat of our scramble and fit method of measuring detection limits is that it does not recover the deepest possible contrast limit when the target has a strong binary signal. When the kernel phases are scrambled to generate a new realization of the noise, we want no signal to be present, so we subtract off the best fit model. In this survey where we treated all sources the same, we simply subtracted the best fit single point source model to remove any small position offset. When a binary is present, subtracting off only a signal source leaves signal behind, raising the measured noise threshold. To properly characterize the sensitivity around a non-single source, the proper model (with the correct parameter values) must be subtracted. This is particularly difficult when triple sources are possible (e.g. **2M 0205-1159**). For this source, our fitting routine failed to produce the companion fit that appears to match under visual inspection (because it is a triple) though it was characterized as significant. On the other hand, Bayes Factors are agnostic of the best fit parameters as they consider the entire volume of parameter space. They are however difficult to interpret if there are unmodeled systematics. For example, a few wide binaries which are aliased and thus difficult to recover with KPI are not considered significant detections by our scramble-and-fit method but do show high Bayes factors, indicating that a binary model is preferred even if our best fit parameters are clearly incorrect.

As seen in Figure 8, there are a few sources with high Bayes factors which did not pass our criteria for a detection and *visa versa*. The three sources with the highest Bayes factors (which suggest binarity), but for which we do not find a successful KPI fit, are **2M 0429-3123**, **2M 1707-0558**, and **2M 0915+0422** (in order by descending Bayes factor). These are all wide binaries that are aliased by our aperture model and KPI struggles to accurately recover. We do characterize **2M 0429-3123** as a binary as its best fit parameters match with literature values while the companion was just outside our grid for detection limits. On the other hand our fits to **2M 1707-0558**, and **2M 0915+0422** both picked up on aliases and failed to recover the visually obvious companion. Similarly

**2M 1705-0516** and **2M 1731+2721** both have high Bayes factors and a wide (aliased) secondary source in the images that is a background source. A more careful treatment of the Bayesian prior could encourage the fits to converge on the non-aliased signal, though it is clear from the Bayes factor that these sources prefer the binary model over the single one. Since Bayes factors are independent of best fit parameters, they allow us to infer the presence of a companion even if our best fit parameters are clearly aliased and thus incorrect.

Our marginal detection of **2M 2028+0052** is also supported by its elevated Bayes factor with respect to other single sources. This source is discussed further in Section 4.2.

Conversely the companions which we characterized as detections which had the lowest Bayes factors include **2M 0205-1159** and **2M 2204-5646**, two of our “spurious” detections (one is a low SNR wide binary and the other is a triple). Detections with relatively low SNR observations, including **2M 1534+1615**, **SDSS 2052-1609**, and **2M 2252-1730**, also had low Bayes factors. In fact, all of these targets were observed in program 11136, which traded exposure time in the main filters for wider wavelength coverage in more filters. This indicates that high SNR observations, which significantly recover the wings of the PSF, are key to confident and accurate KPI detections.

We have also examined a modified version of the likelihood ratio test discussed in [Ceau et al. \(2019\)](#). Instead of the null hypothesis being all 0 kernel-phases we have replaced it with our single source model, allowing for a small centroid offset. This test gives similar results to the Bayes Factors though with slightly more overlap between significant detections and non-detections.

#### 5.4. KPI In Context

Since our detection significance is determined on a source-specific basis, our survey wide stacked detection limit is as close as we can come to a pipeline-specific contrast curve similar to Figure 2 and 3 of [Pope et al. \(2013\)](#) (calculated using an injection-recovery grid with a noise term representative of the sample as a whole). We also use a  $5\sigma$  (99.99994%) detection threshold and separate out the two filters while [Pope et al. \(2013\)](#) presents only a single 99.9% contrast curve. With the aforementioned caveats, the detection limits of our two KPI surveys are fairly similar. Both show a cutoff to equal-brightness companions at around 55 mas (in F110W for our survey, our cut-off in F170M is closer to 80 mas) with slightly higher contrast detections possible down to roughly 30 mas. Our high-contrast limits at wider separations are more difficult to compare given the difference in confidence threshold but appear qualitatively similar, with high confidence detections up to contrast values of roughly 100:1.

Comparing our KPI contrast limits to imaging surveys (e.g. [Reid et al. 2006, 2008a](#)) shows the power of KPI at close separations. Imaging sensitivity significantly drops at separations below  $\sim 0''.5$  while ours is flat down to less than  $\sim 0''.1$ . At wide separations KPI suffers from aliasing in the Fourier plane and is ineffective at detecting sources without prior knowledge. In this wide separation domain PSF fitting performs well and KPI is not necessary. [Sallum & Skemer \(2019\)](#) showed, using simulated *JWST* observations that NRM/AMI outperforms KPI at separations below the diffraction limit by 0.5–1 mag while KPI is comparable to or better than NRM/AMI outside the diffraction limit.

## 6. CONCLUSIONS

We have presented a new pipeline named Argus for super-resolution detection of companions using KPI. The pipeline generates, calibrates, and fits kernel phases from high resolution images. The

pipeline uses a scramble and fit method (similar to previous NRM pipelines) to determine the detection significance, though it can also use Bayes factors to determine if the source is non-singular. Our multi-calibrator method for determining if a detection is real is much more strict than previous KPI pipelines, though it finds roughly similar contrast limits. The pipeline is open source and is available on GitHub (see Footnote 1).

We have demonstrated the pipeline on the entire *HST/NICMOS* F110W and F170M image archive of nearby brown dwarfs (observed in 7 different programs). We recover 19 known companions (including two targets with two epochs) from our sample of 114 targets. We confirm one of the four new companions discovered by Pope et al. (2013) and marginally recovered a second, but we recover none of their marginal detections. We conclude that robust calibration with multiple well-matched calibrators is critical for determining the validity of a candidate companion, especially in the super-resolution regime where no spatially distinct PSF is present.

We report a binary fraction of  $\epsilon_b = 14.4_{-3.0}^{+4.7}\%$ , consistent with previous studies. We will perform a more detailed population level analysis of the catalogue presented here in a future paper. This work will simultaneously characterize the binary fraction, semimajor axis distribution, and mass ratio distributions using a Bayesian framework similar to Allen (2007) to better understand how these low mass objects form. Future upgrades to the pipeline could include more robust bad pixel rejection techniques (Ireland 2013) and triple point source models. It also should be straightforward to make the code easily adaptable to other space based cameras amenable to KPI such as the high resolution channel of *HST/ACS* and the imaging instruments aboard *JWST*.

We thank Trent Dupuy, Will Best, and Michael Ireland for useful discussions about this work, and many others who have offered their thoughts at conferences. We also thank the anonymous referee for their helpful feedback which improved the manuscript. This work was funded by *HST* program AR-14561. This work has benefited from The UltracoolSheet, maintained by Will Best, Trent Dupuy, Michael Liu, Rob Siverd, and Zhoujian Zhang, and developed from compilations by Dupuy & Liu (2012), Dupuy & Kraus (2013), Liu et al. (2016), Best et al. (2018), and Best et al. (2021). This work has made use of data from the European Space Agency (ESA) mission *Gaia* (<https://www.cosmos.esa.int/gaia>), processed by the *Gaia* Data Processing and Analysis Consortium (DPAC, <https://www.cosmos.esa.int/web/gaia/dpac/consortium>). Funding for the DPAC has been provided by national institutions, in particular the institutions participating in the *Gaia* Multilateral Agreement.

*Facility:* HST(NICMOS)

*Software:* Argus (Factor2022) <https://github.com/smfactor/Argus>, astropy (Astropy Collaboration et al. 2013, 2018), PyMultiNest (Buchner et al. 2014), MultiNest (Feroz & Hobson 2008; Feroz et al. 2009, 2019), corner (Foreman-Mackey 2016), numpy (Harris et al. 2020), SciPy (Virtanen et al. 2020)

## REFERENCES

- Allen, P. R. 2007, ApJ, 668, 492. <https://ui.adsabs.harvard.edu/abs/2007ApJ...668..492A>
- Aller, K. M., Liu, M. C., Magnier, E. A., et al. 2016, ApJ, 821, 120. <https://ui.adsabs.harvard.edu/abs/2016ApJ...821..120A>



- Astropy Collaboration, Robitaille, T. P., Tollerud, E. J., et al. 2013, *A&A*, 558, A33. <https://ui.adsabs.harvard.edu/abs/2013A&A...558A..33A>
- Astropy Collaboration, Price-Whelan, A. M., Sipőcz, B. M., et al. 2018, *AJ*, 156, 123. <https://ui.adsabs.harvard.edu/abs/2018AJ...156..123A>
- Bardalez Gagliuffi, D. C., Gelino, C. R., & Burgasser, A. J. 2015, *AJ*, 150, 163. <https://ui.adsabs.harvard.edu/abs/2015AJ....150..163B>
- Basu, S. 2012, *Science*, 337, 43. <https://ui.adsabs.harvard.edu/abs/2012Sci...337...43B>
- Bate, M. R. 2012, *MNRAS*, 419, 3115. <https://ui.adsabs.harvard.edu/abs/2012MNRAS.419.3115B>
- Bate, M. R., Bonnell, I. A., & Bromm, V. 2002, *MNRAS*, 332, L65. <https://ui.adsabs.harvard.edu/abs/2002MNRAS.332L..65B>
- Belokurov, V., Penoyre, Z., Oh, S., et al. 2020, *MNRAS*, 496, 1922. <https://ui.adsabs.harvard.edu/abs/2020MNRAS.496.1922B>
- Bernat, D., Bouchez, A. H., Ireland, M., et al. 2010, *ApJ*, 715, 724. <https://ui.adsabs.harvard.edu/abs/2010ApJ...715..724B>
- Best, W. M. J., Liu, M. C., Magnier, E. A., & Dupuy, T. J. 2020, *AJ*, 159, 257. <https://ui.adsabs.harvard.edu/abs/2020AJ....159..257B>
- . 2021, *AJ*, 161, 42. <https://ui.adsabs.harvard.edu/abs/2021AJ....161...42B>
- Best, W. M. J., Magnier, E. A., Liu, M. C., et al. 2018, *ApJS*, 234, 1. <https://ui.adsabs.harvard.edu/abs/2018ApJS...234....1B>
- Bouy, H., Martín, E. L., Brandner, W., & Bouvier, J. 2005, *AJ*, 129, 511. <https://ui.adsabs.harvard.edu/abs/2005AJ....129..511B>
- Buchner, J., Georgakakis, A., Nandra, K., et al. 2014, *A&A*, 564, A125. <https://ui.adsabs.harvard.edu/abs/2014A&A...564A.125B>
- Burgasser, A. 2003, *T Dwarf Companions: Searching for the Coldest Brown Dwarfs*, HST Proposal, , . <https://ui.adsabs.harvard.edu/abs/2003hst..prop.9833B>
- Burgasser, A. J., Bardalez-Gagliuffi, D. C., & Gizis, J. E. 2011, *AJ*, 141, 70. <https://ui.adsabs.harvard.edu/abs/2011AJ....141...70B>
- Burgasser, A. J., Cruz, K. L., Cushing, M., et al. 2010, *ApJ*, 710, 1142. <https://ui.adsabs.harvard.edu/abs/2010ApJ...710.1142B>
- Burgasser, A. J., Geballe, T. R., Leggett, S. K., Kirkpatrick, J. D., & Golimowski, D. A. 2006a, *ApJ*, 637, 1067. <https://ui.adsabs.harvard.edu/abs/2006ApJ...637.1067B>
- Burgasser, A. J., Kirkpatrick, J. D., Cruz, K. L., et al. 2006b, *ApJS*, 166, 585. <https://ui.adsabs.harvard.edu/abs/2006ApJS..166..585B>
- Burgasser, A. J., Kirkpatrick, J. D., Liebert, J., & Burrows, A. 2003a, *ApJ*, 594, 510. <https://ui.adsabs.harvard.edu/abs/2003ApJ...594..510B>
- Burgasser, A. J., Kirkpatrick, J. D., & Lowrance, P. J. 2005, *AJ*, 129, 2849. <https://ui.adsabs.harvard.edu/abs/2005AJ....129.2849B>
- Burgasser, A. J., Kirkpatrick, J. D., McElwain, M. W., et al. 2003b, *AJ*, 125, 850. <https://ui.adsabs.harvard.edu/abs/2003AJ....125..850B>
- Burgasser, A. J., Kirkpatrick, J. D., Reid, I. N., et al. 2003c, *ApJ*, 586, 512. <https://ui.adsabs.harvard.edu/abs/2003ApJ...586..512B>
- Burgasser, A. J., Kirkpatrick, J. D., Cutri, R. M., et al. 2000, *ApJL*, 531, L57. <https://ui.adsabs.harvard.edu/abs/2000ApJ...531L..57B>
- Burgasser, A. J., Kirkpatrick, J. D., Brown, M. E., et al. 2002, *ApJ*, 564, 421. <https://ui.adsabs.harvard.edu/abs/2002ApJ...564..421B>
- Cardoso, C. V., Burningham, B., Smart, R. L., et al. 2015, *MNRAS*, 450, 2486. <https://ui.adsabs.harvard.edu/abs/2015MNRAS.450.2486C>
- Ceau, A., Mary, D., Greenbaum, A., et al. 2019, *A&A*, 630, A120. <https://ui.adsabs.harvard.edu/abs/2019A&A...630A.120C>
- Chiu, K., Fan, X., Leggett, S. K., et al. 2006, *AJ*, 131, 2722. <https://ui.adsabs.harvard.edu/abs/2006AJ....131.2722C>
- Cruz, K. 2004, *Resolving a Binary System that Straddles the L/T Transition*, HST Proposal, , . <https://ui.adsabs.harvard.edu/abs/2004hst..prop10247C>
- Cruz, K. L., Burgasser, A. J., Reid, I. N., & Liebert, J. 2004, *ApJL*, 604, L61. <https://ui.adsabs.harvard.edu/abs/2004ApJ...604L..61C>
- Cruz, K. L., Reid, I. N., Liebert, J., Kirkpatrick, J. D., & Lowrance, P. J. 2003, *AJ*, 126, 2421. <https://ui.adsabs.harvard.edu/abs/2003AJ...126.2421C>
- Cutri, R. M., Skrutskie, M. F., van Dyk, S., et al. 2003, *VizieR Online Data Catalog*, 2246. <https://ui.adsabs.harvard.edu/abs/2003yCat.2246....0C>

- Dahn, C. C., Harris, H. C., Subasavage, J. P., et al. 2017, *AJ*, 154, 147. <https://ui.adsabs.harvard.edu/abs/2017AJ....154..147D>
- Deshpande, R., Martín, E. L., Montgomery, M. M., et al. 2012, *AJ*, 144, 99. <https://ui.adsabs.harvard.edu/abs/2012AJ....144..99D>
- Duchêne, G., & Kraus, A. 2013, *ARA&A*, 51, 269. <https://ui.adsabs.harvard.edu/abs/2013ARA&A..51..269D>
- Dupuy, T. J., & Kraus, A. L. 2013, *Science*, 341, 1492. <https://ui.adsabs.harvard.edu/abs/2013Sci...341.1492D>
- Dupuy, T. J., & Liu, M. C. 2011, *ApJ*, 733, 122. <https://ui.adsabs.harvard.edu/abs/2011ApJ...733..122D>
- . 2012, *ApJS*, 201, 19. <https://ui.adsabs.harvard.edu/abs/2012ApJS..201...19D>
- Dupuy, T. J., & Liu, M. C. 2017, *ApJS*, 231, 15. <https://ui.adsabs.harvard.edu/abs/2017ApJS..231...15D>
- Dupuy, T. J., Liu, M. C., Bowler, B. P., et al. 2010, *ApJ*, 721, 1725. <https://ui.adsabs.harvard.edu/abs/2010ApJ...721.1725D>
- Factor, S. M. 2022, *smfactor/Argus: Version 1.0* for publication in *AJ*, v1.0, Zenodo, doi:10.5281/zenodo.6842148. <https://doi.org/10.5281/zenodo.6842148>
- Factor, S. M., & Kraus, A. L. 2022, *Figure Sets and Data Associated with AJ Publication: "NICMOS Kernel-Phase Interferometry I: Catalogue of Brown Dwarfs Observed in F110W and F170M"*, Zenodo, doi:10.5281/zenodo.6986242. <https://doi.org/10.5281/zenodo.6986242>
- Faherty, J. K., Burgasser, A. J., Cruz, K. L., et al. 2009, *AJ*, 137, 1. <https://ui.adsabs.harvard.edu/abs/2009AJ....137....1F>
- Faherty, J. K., Burgasser, A. J., Walter, F. M., et al. 2012, *ApJ*, 752, 56. <https://ui.adsabs.harvard.edu/abs/2012ApJ...752...56F>
- Faherty, J. K., Riedel, A. R., Cruz, K. L., et al. 2016, *ApJS*, 225, 10. <https://ui.adsabs.harvard.edu/abs/2016ApJS..225...10F>
- Feroz, F., & Hobson, M. P. 2008, *MNRAS*, 384, 449. <https://ui.adsabs.harvard.edu/abs/2008MNRAS.384..449F>
- Feroz, F., Hobson, M. P., & Bridges, M. 2009, *MNRAS*, 398, 1601. <https://ui.adsabs.harvard.edu/abs/2009MNRAS.398.1601F>
- Feroz, F., Hobson, M. P., Cameron, E., & Pettitt, A. N. 2019, *The Open Journal of Astrophysics*, 2, 10. <https://ui.adsabs.harvard.edu/abs/2019OJAp....2E..10F>
- Foreman-Mackey, D. 2016, *The Journal of Open Source Software*, 1, 24. <https://ui.adsabs.harvard.edu/abs/2016JOSS....1...24F>
- Gagné, J., Faherty, J. K., Cruz, K. L., et al. 2015, *ApJS*, 219, 33. <https://ui.adsabs.harvard.edu/abs/2015ApJS..219...33G>
- Gaia Collaboration. 2020, *VizieR Online Data Catalog*, I/350. <https://ui.adsabs.harvard.edu/abs/2020yCat.1350....0G>
- Gaia Collaboration, Brown, A. G. A., Vallenari, A., et al. 2018, *A&A*, 616, A1. <https://ui.adsabs.harvard.edu/abs/2018A&A...616A...1G>
- . 2021, *A&A*, 649, A1. <https://ui.adsabs.harvard.edu/abs/2021A&A...649A...1G>
- Gelino, C. R., Smart, R. L., Marocco, F., et al. 2014, *AJ*, 148, 6. <https://ui.adsabs.harvard.edu/abs/2014AJ....148....6G>
- Gizis, J. 2003, *NICMOS Observations of Cool Brown Dwarf Doubles*, *HST Proposal*, , . <https://ui.adsabs.harvard.edu/abs/2003hst.prop.9843G>
- Harris, C. R., Millman, K. J., van der Walt, S. J., et al. 2020, *Nature*, 585, 357. <https://doi.org/10.1038/s41586-020-2649-2>
- Ireland, M. J. 2013, *MNRAS*, 433, 1718. <https://ui.adsabs.harvard.edu/abs/2013MNRAS.433.1718I>
- Ireland, M. J., Kraus, A., Martinache, F., Lloyd, J. P., & Tuthill, P. G. 2008, *ApJ*, 678, 463. <https://ui.adsabs.harvard.edu/abs/2008ApJ...678..463I>
- Jeffreys, H. 1961, *The Theory of Probability*, Oxford Classic Texts in the Physical Sciences (OUP Oxford), p. 432. <https://books.google.com/books?id=vh9Act9rtzQC>
- Kammerer, J., Ireland, M. J., Martinache, F., & Girard, J. H. 2019, *MNRAS*, 486, 639. <https://ui.adsabs.harvard.edu/abs/2019MNRAS.486..639K>
- Kammerer, J., Kasper, M., Ireland, M. J., et al. 2021, *A&A*, 646, A36. <https://ui.adsabs.harvard.edu/abs/2021A&A...646A..36K>
- Kirkpatrick, J. D., Henry, T. J., & McCarthy, Donald W., J. 1991, *ApJS*, 77, 417. <https://ui.adsabs.harvard.edu/abs/1991ApJS...77..417K>

- Kirkpatrick, J. D., Reid, I. N., Liebert, J., et al. 2000, *AJ*, 120, 447. <https://ui.adsabs.harvard.edu/abs/2000AJ....120..447K>
- Kirkpatrick, J. D., Kellogg, K., Schneider, A. C., et al. 2016, *ApJS*, 224, 36. <https://ui.adsabs.harvard.edu/abs/2016ApJS..224...36K>
- Kirkpatrick, J. D., Martin, E. C., Smart, R. L., et al. 2019, *ApJS*, 240, 19. <https://ui.adsabs.harvard.edu/abs/2019ApJS..240...19K>
- Konopacky, Q. M., Ghez, A. M., Barman, T. S., et al. 2010, *ApJ*, 711, 1087. <https://ui.adsabs.harvard.edu/abs/2010ApJ...711.1087K>
- Kraus, A. L., & Hillenbrand, L. A. 2012, *ApJ*, 757, 141. <https://ui.adsabs.harvard.edu/abs/2012ApJ...757..141K>
- Kraus, A. L., & Ireland, M. J. 2012, *ApJ*, 745, 5. <https://ui.adsabs.harvard.edu/abs/2012ApJ...745....5K>
- Kraus, A. L., Ireland, M. J., Martinache, F., & Hillenbrand, L. A. 2011, *ApJ*, 731, 8. <http://adsabs.harvard.edu/abs/2011ApJ...731....8K>
- Kraus, A. L., Ireland, M. J., Martinache, F., & Lloyd, J. P. 2008, *ApJ*, 679, 762. <https://ui.adsabs.harvard.edu/abs/2008ApJ...679..762K>
- Krist, J. E., & Hook, R. N. 1997, in *The 1997 HST Calibration Workshop with a New Generation of Instruments*, ed. S. Casertano, R. Jędrzejewski, T. Keyes, & M. Stevens, 192. <https://ui.adsabs.harvard.edu/abs/1997hstc.work..192K>
- Krist, J. E., Hook, R. N., & Stoehr, F. 2011, in *Society of Photo-Optical Instrumentation Engineers (SPIE) Conference Series*, Vol. 8127, *Optical Modeling and Performance Predictions V*, ed. M. A. Kahan, 81270J. <https://ui.adsabs.harvard.edu/abs/2011SPIE.8127E..0JK>
- Laugier, R., Martinache, F., Ceau, A., et al. 2019, *A&A*, 623, A164. <https://ui.adsabs.harvard.edu/abs/2019A&A...623A.164L>
- Leggett, S. K., Allard, F., Geballe, T. R., Hauschildt, P. H., & Schweitzer, A. 2001, *ApJ*, 548, 908. <https://ui.adsabs.harvard.edu/abs/2001ApJ...548..908L>
- Leggett, S. K., Golimowski, D. A., Fan, X., et al. 2002, *ApJ*, 564, 452. <https://ui.adsabs.harvard.edu/abs/2002ApJ...564..452L>
- Lindgren, L., Hernández, J., Bombrun, A., et al. 2018, *A&A*, 616, A2. <https://ui.adsabs.harvard.edu/abs/2018A&A...616A...2L>
- Lindgren, L., Klioner, S. A., Hernández, J., et al. 2021, *A&A*, 649, A2. <https://ui.adsabs.harvard.edu/abs/2021A&A...649A...2L>
- Liu, M. 2007, *Resolving Ultracool Astrophysics with Brown Dwarf Binaries*, HST Proposal, . <https://ui.adsabs.harvard.edu/abs/2007hst.prop11136L>
- Liu, M. C., Dupuy, T. J., & Allers, K. N. 2016, *ApJ*, 833, 96. <https://ui.adsabs.harvard.edu/abs/2016ApJ...833...96L>
- Liu, M. C., Leggett, S. K., Golimowski, D. A., et al. 2006, *ApJ*, 647, 1393. <https://ui.adsabs.harvard.edu/abs/2006ApJ...647.1393L>
- Lloyd, J. P., Martinache, F., Ireland, M. J., et al. 2006, *ApJL*, 650, L131. <https://ui.adsabs.harvard.edu/abs/2006ApJ...650L.131L>
- Lodieu, N., Scholz, R. D., McCaughrean, M. J., et al. 2005, *A&A*, 440, 1061. <https://ui.adsabs.harvard.edu/abs/2005A&A...440.1061L>
- Manjavacas, E., Goldman, B., Reffert, S., & Henning, T. 2013, *A&A*, 560, A52. <https://ui.adsabs.harvard.edu/abs/2013A&A...560A..52M>
- Marocco, F., Andrei, A. H., Smart, R. L., et al. 2013, *AJ*, 146, 161. <https://ui.adsabs.harvard.edu/abs/2013AJ....146..161M>
- Marocco, F., Jones, H. R. A., Day-Jones, A. C., et al. 2015, *MNRAS*, 449, 3651. <https://ui.adsabs.harvard.edu/abs/2015MNRAS.449.3651M>
- Martinache, F. 2010, *ApJ*, 724, 464. <https://ui.adsabs.harvard.edu/abs/2010ApJ...724..464M>
- Martinache, F., Ceau, A., Laugier, R., et al. 2020, *A&A*, 636, A72. <https://ui.adsabs.harvard.edu/abs/2020A&A...636A..72M>
- Metchev, S. A., Kirkpatrick, J. D., Berriman, G. B., &Looper, D. 2008, *ApJ*, 676, 1281. <https://ui.adsabs.harvard.edu/abs/2008ApJ...676.1281M>
- Perryman, M. A. C., Lindgren, L., Kovalevsky, J., et al. 1997, *A&A*, 323, L49. <https://ui.adsabs.harvard.edu/abs/1997A&A...323L..49P>
- Pope, B., Martinache, F., & Tuthill, P. 2013, *ApJ*, 767, 110. <https://ui.adsabs.harvard.edu/abs/2013ApJ...767..110P>
- Pope, B., Tuthill, P., Hinkley, S., et al. 2016, *MNRAS*, 455, 1647. <https://ui.adsabs.harvard.edu/abs/2016MNRAS.455.1647P>

- Press, W. H., Teukolsky, S. A., Vetterling, W. T., & Flannery, B. P. 2002, Numerical recipes in C++ : the art of scientific computing (Cambridge University Press). <https://ui.adsabs.harvard.edu/abs/2002nrca.book.....P>
- Reid, I. 2004, Ultracool companions to the nearest L dwarfs, HST Proposal, , . <https://ui.adsabs.harvard.edu/abs/2004hst..prop10143R>
- . 2006, A search for planetary-mass companions to the nearest L dwarfs - completing the survey, HST Proposal, , . <https://ui.adsabs.harvard.edu/abs/2006hst..prop10879R>
- Reid, I. N., Cruz, K. L., Burgasser, A. J., & Liu, M. C. 2008a, AJ, 135, 580. <https://ui.adsabs.harvard.edu/abs/2008AJ....135..580R>
- Reid, I. N., Cruz, K. L., Kirkpatrick, J. D., et al. 2008b, AJ, 136, 1290. <https://ui.adsabs.harvard.edu/abs/2008AJ....136.1290R>
- Reid, I. N., Kirkpatrick, J. D., Gizis, J. E., et al. 2000, AJ, 119, 369. <https://ui.adsabs.harvard.edu/abs/2000AJ....119..369R>
- Reid, I. N., Lewitus, E., Allen, P. R., Cruz, K. L., & Burgasser, A. J. 2006, AJ, 132, 891. <https://ui.adsabs.harvard.edu/abs/2006AJ....132..891R>
- Reyl e, C., Delorme, P., Willott, C. J., et al. 2010, A&A, 522, A112. <https://ui.adsabs.harvard.edu/abs/2010A&A...522A.112R>
- Roye, E., Krist, J., Schultz, A. B., & Wiklund, T. 2003, Measuring the Cold Mask Offset, Tech. rep. <https://ui.adsabs.harvard.edu/abs/2003nicm.rept....4R>
- Sallum, S., & Skemer, A. 2019, Journal of Astronomical Telescopes, Instruments, and Systems, 5, 018001. <https://ui.adsabs.harvard.edu/abs/2019JATIS...5a8001S>
- Sallum, S., Follette, K. B., Eisner, J. A., et al. 2015, Nature, 527, 342. <https://ui.adsabs.harvard.edu/abs/2015Natur.527..342S>
- Schmidt, S. J., Cruz, K. L., Bongiorno, B. J., Liebert, J., & Reid, I. N. 2007, AJ, 133, 2258. <https://ui.adsabs.harvard.edu/abs/2007AJ...133.2258S>
- Schneider, A. C., Cushing, M. C., Kirkpatrick, J. D., et al. 2014, AJ, 147, 34. <https://ui.adsabs.harvard.edu/abs/2014AJ....147...34S>
- Schultz, A. 2002, NICMOS Deep PSF for Determining Cold Mask Offsets, HST Proposal, , . <https://ui.adsabs.harvard.edu/abs/2002hst..prop.9704S>
- Skrzypek, N., Warren, S. J., & Faherty, J. K. 2016, A&A, 589, A49. <https://ui.adsabs.harvard.edu/abs/2016A&A...589A..49S>
- Smart, R. L., Tinney, C. G., Bucciarelli, B., et al. 2013, MNRAS, 433, 2054. <https://ui.adsabs.harvard.edu/abs/2013MNRAS.433.2054S>
- Smart, R. L., Bucciarelli, B., Jones, H. R. A., et al. 2018, MNRAS, 481, 3548. <https://ui.adsabs.harvard.edu/abs/2018MNRAS.481.3548S>
- Tinney, C. G., Faherty, J. K., Kirkpatrick, J. D., et al. 2014, ApJ, 796, 39. <https://ui.adsabs.harvard.edu/abs/2014ApJ...796...39T>
- Tuthill, P., Lloyd, J., Ireland, M., et al. 2006, in Society of Photo-Optical Instrumentation Engineers (SPIE) Conference Series, Vol. 6272, Society of Photo-Optical Instrumentation Engineers (SPIE) Conference Series, ed. B. L. Ellerbroek & D. Bonaccini Calia, 62723A. <https://ui.adsabs.harvard.edu/abs/2006SPIE.6272E.103T>
- Tuthill, P. G. 2012, in Society of Photo-Optical Instrumentation Engineers (SPIE) Conference Series, Vol. 8445, Optical and Infrared Interferometry III, ed. F. Delplancke, J. K. Rajagopal, & F. Malbet, 844502. <https://ui.adsabs.harvard.edu/abs/2012SPIE.8445E..02T>
- Virtanen, P., Gommers, R., Oliphant, T. E., et al. 2020, Nature Methods, 17, 261. <https://ui.adsabs.harvard.edu/abs/2020NatMe..17..261V>
- Wallace, A. L., Kammerer, J., Ireland, M. J., et al. 2020, MNRAS, 498, 1382. <https://ui.adsabs.harvard.edu/abs/2020MNRAS.498.1382W>
- West, A. A., Hawley, S. L., Bochanski, J. J., et al. 2008, AJ, 135, 785. <https://ui.adsabs.harvard.edu/abs/2008AJ....135..785W>

**Table 4.** Individual  $5\sigma$  Contrast Ratio Limits in F110W

Source	Contrast Limit in F110W at Sep. [mas]						
	55–65	75–85	90–110	160–200	250–300	350–400	450–500
2M 0004-4044	$2.3 \pm 0.6, 2.1 \pm 0.5$	$3.35 \pm 0.26$	$4.43 \pm 0.30$	$2.42 \pm 0.24$	$3.7 \pm 0.7$	$4.6 \pm 0.8$	$3.9 \pm 0.5$
2M 0024-0158	$63 \pm 7$	$115 \pm 5$	$138 \pm 6$	$66 \pm 4$	$126 \pm 5$	$138 \pm 12$	$100 \pm 5$
2M 0025+4759		$1.5 \pm 0.4$	$1.59 \pm 0.13$		$1.52 \pm 0.16$	$2.01 \pm 0.21$	$2.8 \pm 0.5$
2M 0036+1821	$34.5 \pm 3.2$	$65.8 \pm 2.8$	$79.2 \pm 3.1$	$41.3 \pm 1.7$	$75.7 \pm 3.5$	$87.0 \pm 3.3$	$55 \pm 5$
2M 0045+1634	$55 \pm 6$	$95 \pm 4$	$115 \pm 9$	$62.9 \pm 2.9$	$110 \pm 9$	$126 \pm 5$	$83 \pm 4$
2M 0107+0041	$32.8 \pm 3.4$	$60 \pm 5$	$72 \pm 7$	$37.6 \pm 2.4$	$72 \pm 7$	$72.2 \pm 3.0$	$50 \pm 9$
2M 0109+2949	$55 \pm 10$	$95 \pm 11$	$115 \pm 8$	$63 \pm 10$	$105 \pm 4$	$121 \pm 9$	$80 \pm 7$
2M 0123-4240	$6.1 \pm 1.7$	$12.3 \pm 1.4$	$17.9 \pm 2.4$	$9.3 \pm 2.2$	$13.5 \pm 1.9$	$16.3 \pm 1.6$	$13.6 \pm 1.3$
2M 0144-0716	$43 \pm 5$	$72 \pm 11$	$87 \pm 9$	$48 \pm 4$	$76 \pm 6$	$100 \pm 7$	$60 \pm 11$
2M 0147-4954	$4.5 \pm 0.8, 1.4 \pm 0.5$	$7.7 \pm 0.4$	$9.3 \pm 0.9$	$3.9 \pm 0.6$	$9.8 \pm 1.5$	$8.9 \pm 0.7$	$6.74 \pm 0.31$
2M 0151+1244	$38 \pm 5$	$59.9 \pm 2.8$	$79 \pm 10$	$39 \pm 4$	$72 \pm 6$	$95 \pm 4$	$60 \pm 11$
2M 0155+0950	$4.04 \pm 0.27, 1.4 \pm 0.4$	$13.5 \pm 2.7$	$11.2 \pm 0.8$	$5.9 \pm 1.7$	$11.9 \pm 2.4$	$12.9 \pm 1.0$	$7.40 \pm 0.34$
2M 0205-1159	$1.0 \pm 0$	$2.8 \pm 0.4$	$4.0 \pm 0.4$	$2.01 \pm 0.24$	$3.5 \pm 0.4$	$4.23 \pm 0.31$	$4.65 \pm 0.22$
2M 0207+0000	$7.1 \pm 1.6, 1.00 \pm 0.20$	$13.5 \pm 2.9$	$19.6 \pm 1.9$	$10.7 \pm 1.2$	$16.3 \pm 1.8$	$19.6 \pm 0.8$	$15.6 \pm 0.7$
2M 0213+4444	$79 \pm 7$	$138 \pm 11$	$183 \pm 22$	$91 \pm 9$	$183 \pm 13$	$192 \pm 9$	$111 \pm 15$
2M 0228+1639	$25 \pm 4$	$45.3 \pm 3.5$	$54.6 \pm 2.1$	$27.2 \pm 3.2$	$52.2 \pm 2.4$	$57.3 \pm 2.7$	$36.0 \pm 1.7$
2M 0243-2453	$13.6 \pm 2.6$	$26 \pm 9$	$26 \pm 4$	$18 \pm 4$	$24.8 \pm 3.1$	$29 \pm 4$	$19.7 \pm 1.8$
2M 0251-0352	$2.8 \pm 0.6, 1.0 \pm 0.6$	$9.3 \pm 1.9$	$7.7 \pm 0.5$	$3.9 \pm 1.3$	$8.2 \pm 1.7$	$8.5 \pm 0.6$	$5.4 \pm 0.5$
2M 0255-4700	$73 \pm 12$	$105 \pm 10$	$152 \pm 11$	$76 \pm 8$	$121 \pm 15$	$167 \pm 6$	$105 \pm 10$
2M 0257-3105	$34.3 \pm 3.3$	$60 \pm 9$	$72.2 \pm 3.1$	$36.0 \pm 2.4$	$60 \pm 8$	$72.2 \pm 3.0$	$52.2 \pm 2.4$
2M 0314+1603	$41 \pm 4$	$72 \pm 11$	$95 \pm 4$	$50 \pm 6$	$83 \pm 7$	$105 \pm 4$	$72 \pm 14$
2M 0318-3421	$24.8 \pm 3.3$	$41.3 \pm 1.7$	$55 \pm 4$	$26.0 \pm 2.4$	$46 \pm 6$	$57 \pm 4$	$36.0 \pm 1.7$
2M 0348-6022	$46 \pm 7$	$87 \pm 7$	$95 \pm 8$	$49.8 \pm 2.1$	$91 \pm 7$	$110 \pm 8$	$76 \pm 11$
2M 0355+1133	$16.3 \pm 1.8$	$28 \pm 4$	$34 \pm 5$	$21 \pm 4$	$31.3 \pm 3.4$	$36 \pm 4$	$26 \pm 5$
2M 0415-0935	$6.4 \pm 2.2, 1.00 \pm 0.32$	$13.5 \pm 2.1$	$21.5 \pm 2.3$	$11.2 \pm 2.4$	$15.6 \pm 2.3$	$17.9 \pm 1.7$	$15.7 \pm 2.2$
2M 0423-0414	$3.1 \pm 0.7, 1.00 \pm 0.15$	$5.9 \pm 0.6$	$8.5 \pm 1.0$	$4.2 \pm 0.5$	$7.1 \pm 0.5$	$7.4 \pm 0.9$	$6.74 \pm 0.31$
2M 0423-0414	$3.05 \pm 0.34, 1.0 \pm 0.6$	$5.9 \pm 1.0$	$7.7 \pm 0.8$	$3.05 \pm 0.34$	$6.43 \pm 0.25$	$7.4 \pm 0.6$	$4.9 \pm 0.8$
2M 0429-3123			$1.39 \pm 0.14$	$1.10 \pm 0.10$	$1.52 \pm 0.16$	$2.10 \pm 0.09$	$2.66 \pm 0.12$
2M 0439-2353	$55 \pm 5$	$95 \pm 14$	$126 \pm 12$	$59.9 \pm 2.8$	$121 \pm 13$	$145 \pm 11$	$95 \pm 18$
2M 0443+0002	$66 \pm 6$	$105 \pm 8$	$152 \pm 13$	$69 \pm 8$	$132 \pm 11$	$152 \pm 21$	$105 \pm 20$
2M 0445-3048	$4.6 \pm 2.0, 1.00 \pm 0.26$	$9.3 \pm 2.2$	$13.5 \pm 1.3$	$6.1 \pm 0.9$	$11.2 \pm 0.7$	$12.9 \pm 1.0$	$8.9 \pm 0.4$
2M 0500+0330	$45 \pm 6$	$79 \pm 6$	$79 \pm 14$	$48 \pm 7$	$96 \pm 14$	$105 \pm 20$	$60 \pm 11$
2M 0518-2828	$6.7 \pm 1.0, 1.00 \pm 0.20$	$12.3 \pm 1.4$	$14.8 \pm 1.2$	$8.5 \pm 0.5$	$14.8 \pm 0.6$	$17.9 \pm 1.9$	$10.7 \pm 0.5$
2M 0518-2828	$5.1 \pm 1.1, 1.00 \pm 0.32$	$10.2 \pm 1.5$	$12.3 \pm 0.9$	$6.1 \pm 0.5$	$11.8 \pm 0.9$	$14.2 \pm 1.0$	$9.8 \pm 0.5$
2M 0523-1403	$57 \pm 4$	$95 \pm 4$	$138 \pm 14$	$63 \pm 8$	$121 \pm 6$	$100 \pm 13$	$91 \pm 4$
2M 0624-4521	$52 \pm 5$	$87 \pm 11$	$95 \pm 7$	$48 \pm 6$	$83 \pm 15$	$100 \pm 10$	$83 \pm 4$
2M 0652+4710	$9.8 \pm 0.7, 1.00 \pm 0.04$	$17.9 \pm 0.8$	$26.0 \pm 2.2$	$11.2 \pm 1.1$	$22.6 \pm 3.3$	$27.2 \pm 2.0$	$17.9 \pm 3.3$
2M 0700+3157	$13.6 \pm 3.0$	$17.9 \pm 2.7$	$26 \pm 4$	$11.8 \pm 1.4$	$23.6 \pm 3.1$	$27 \pm 5$	$17.9 \pm 3.3$
2M 0727+1710	$8.9 \pm 1.2, 1.00 \pm 0.09$	$16.3 \pm 0.7$	$19.6 \pm 1.3$	$9.8 \pm 0.7$	$17.9 \pm 1.9$	$19.6 \pm 0.8$	$12.9 \pm 0.6$
2M 0755+2212	$55 \pm 6$	$95 \pm 7$	$105 \pm 16$	$60 \pm 6$	$105 \pm 4$	$121 \pm 16$	$95 \pm 18$
2M 0825+2115	$14.2 \pm 2.1$	$24 \pm 4$	$26 \pm 4$	$18 \pm 4$	$24.8 \pm 2.6$	$26 \pm 4$	$20 \pm 4$
2M 0830+4828	$48 \pm 11$	$72 \pm 5$	$105 \pm 9$	$50 \pm 6$	$96 \pm 9$	$115 \pm 16$	$57.3 \pm 2.7$
2M 0835-0819	$50 \pm 8$	$72.2 \pm 3.3$	$95 \pm 10$	$50 \pm 5$	$87 \pm 11$	$115 \pm 11$	$75.7 \pm 3.5$

*Table 4 continued on next page*

Table 4 (continued)

Source	Contrast Limit in F110W at Sep. [mas]						
	55–65	75–85	90–110	160–200	250–300	350–400	450–500
2M 0847-1532	45 ± 9	87 ± 13	105 ± 6	55 ± 9	100 ± 5	115 ± 13	75.7 ± 3.5
2M 0850+1057	3.68 ± 0.33, 1.4 ± 0.4	10.2 ± 2.2	13.5 ± 1.1	4.9 ± 0.7	10.7 ± 1.1	11.8 ± 1.5	8.5 ± 0.8
2M 0859-1949	45.3 ± 3.0	87 ± 4	105 ± 9	52.2 ± 3.5	105 ± 7	115 ± 11	73 ± 7
2M 0908+5032	49.8 ± 3.3	72 ± 13	87 ± 10	48 ± 6	95 ± 4	100 ± 7	69.0 ± 3.2
2M 0911+7401	49.8 ± 2.1	95 ± 4	126 ± 11	63 ± 6	115 ± 16	132 ± 6	83 ± 4
2M 0915+0422		1.00 ± 0.15	1.59 ± 0.31	1.10 ± 0.08	1.67 ± 0.17	2.42 ± 0.20	3.1 ± 0.5
2M 0921-2104	47.6 ± 2.2	79 ± 12	105 ± 12	52 ± 7	95 ± 13	100 ± 10	76 ± 11
2M 0926+5847	6.1 ± 1.4, 1.00 ± 0.32	18 ± 4	19.6 ± 1.4	9.8 ± 1.4	19.6 ± 2.1	21 ± 4	12.4 ± 1.1
2M 1021-0304		3.05 ± 0.29	3.7 ± 0.4	1.45 ± 0.34	2.32 ± 0.22	3.4 ± 0.4	3.20 ± 0.15
2M 1022+5825	63 ± 5	95 ± 9	126 ± 14	69 ± 8	121 ± 6	138 ± 5	95 ± 18
2M 1025+3212	20 ± 4	31 ± 7	45.3 ± 3.1	20.6 ± 2.1	38 ± 5	45 ± 6	32 ± 6
2M 1043+2225	36 ± 6	59.9 ± 2.8	79 ± 8	38 ± 5	76 ± 8	83 ± 9	55 ± 10
2M 1045-0149	33 ± 4	55 ± 8	72 ± 5	34 ± 4	66 ± 6	79 ± 5	43.3 ± 2.0
2M 1048+0111	11.8 ± 2.1	20 ± 4	24 ± 4	15.6 ± 3.4	21.5 ± 3.4	24 ± 5	18.8 ± 0.9
2M 1051+5613	43 ± 5	72 ± 5	95 ± 10	52 ± 9	95 ± 13	105 ± 7	75.7 ± 3.5
2M 1058-1548	76 ± 11	152 ± 12	183 ± 18	87 ± 16	183 ± 18	183 ± 18	126 ± 24
2M 1104+1959	26 ± 4	60 ± 7	66 ± 4	34 ± 4	63 ± 7	76 ± 6	47.6 ± 2.2
2M 1108+6830	52 ± 7	95 ± 4	126 ± 7	66 ± 9	115 ± 16	132 ± 10	91 ± 4
2M 1110+0116	34 ± 5	65.8 ± 2.8	87 ± 4	45 ± 4	76 ± 13	91 ± 7	55 ± 5
2M 1155-3727	55 ± 4	87 ± 11	115 ± 14	60 ± 9	110 ± 11	121 ± 6	91 ± 4
2M 1203+0015	69 ± 7	115 ± 5	138 ± 7	79 ± 9	138 ± 13	152 ± 6	105 ± 10
2M 1213-0432	48 ± 8	79 ± 12	95 ± 15	55 ± 10	100 ± 5	110 ± 15	70 ± 10
2M 1217-0311	53 ± 8	79 ± 4	105 ± 12	57 ± 7	110 ± 5	115 ± 12	80 ± 7
2M 1221+0257	83 ± 9	138 ± 6	167 ± 7	91 ± 8	159 ± 13	183 ± 18	126 ± 24
2M 1254-0122	6.1 ± 2.0, 1.00 ± 0.32	12.3 ± 2.9	19.6 ± 2.1	10.3 ± 2.3	14.2 ± 1.8	17.1 ± 1.8	13.6 ± 1.3
2M 1300+1912	48 ± 7	79 ± 8	105 ± 11	52 ± 10	105 ± 9	100 ± 10	73 ± 7
2M 1421+1827	62.9 ± 2.9	105 ± 4	138 ± 10	65.8 ± 3.0	121 ± 15	138 ± 6	95 ± 18
2M 1425-3650	92 ± 15	138 ± 13	183 ± 8	83 ± 12	159 ± 13	192 ± 14	115 ± 22
2M 1428+5923	52 ± 4	87 ± 4	115 ± 14	55 ± 5	97 ± 20	115 ± 4	75.7 ± 3.5
2M 1439+1929	73 ± 9	138 ± 15	167 ± 20	80 ± 11	159 ± 12	175 ± 18	105 ± 20
2M 1448+1031	60 ± 8	105 ± 13	126 ± 4	66 ± 4	121 ± 10	126 ± 5	100 ± 5
2M 1503+2525	6.5 ± 2.0, 1.00 ± 0.32	14.8 ± 2.7	19.6 ± 2.5	10.7 ± 1.8	14.2 ± 2.5	17.9 ± 1.2	14.2 ± 0.7
2M 1503+2525	16.3 ± 1.7	19.6 ± 2.4	34 ± 5	14 ± 4	24.8 ± 3.1	26 ± 4	19.7 ± 1.8
2M 1506+1321	49.8 ± 3.3	87 ± 8	115 ± 10	52 ± 6	101 ± 16	115 ± 5	80 ± 7
2M 1507-1627	9.8 ± 1.0	12.3 ± 1.9	19.6 ± 0.9	11.2 ± 0.5	21.5 ± 1.6	20.6 ± 1.7	14.9 ± 1.4
2M 1515+4847	39 ± 5	72 ± 8	87 ± 10	50 ± 8	83 ± 12	95 ± 7	57.3 ± 2.7
2M 1534+1615		3.05 ± 0.29	4.43 ± 0.30	2.10 ± 0.35	3.9 ± 0.4	5.3 ± 0.6	5.10 ± 0.24
2M 1539-0520	7.1 ± 1.1, 1.00 ± 0.32	13.5 ± 2.0	16.3 ± 2.2	8.1 ± 0.9	16.3 ± 1.6	18.8 ± 2.5	12.4 ± 1.1
2M 1552+2948	22.8 ± 3.2	41 ± 5	49.8 ± 2.2	23.6 ± 3.1	48 ± 8	60 ± 6	39.5 ± 1.8
2M 1553+1532		1.60 ± 0.15	1.59 ± 0.27	1.10 ± 0.30	1.60 ± 0.20	2.21 ± 0.10	2.8 ± 0.5
2M 1624+0029	36 ± 6	72 ± 7	95 ± 10	52 ± 8	80 ± 12	100 ± 13	73 ± 7
2M 1658+7027	60 ± 10	105 ± 4	115 ± 9	66 ± 10	121 ± 9	126 ± 8	91 ± 4
2M 1705-0516	2.78 ± 0.34, 2.1 ± 0.6	5.3 ± 1.0	5.9 ± 1.0	2.4 ± 0.4	5.6 ± 0.5	5.6 ± 0.6	4.23 ± 0.20
2M 1707-0558		1.7 ± 0.5	2.31 ± 0.29	1.20 ± 0.16	2.31 ± 0.22	3.05 ± 0.12	3.51 ± 0.16
2M 1721+3344	57 ± 6	105 ± 12	115 ± 5	63 ± 6	115 ± 10	126 ± 8	87 ± 17
2M 1728+3948	3.7 ± 0.6, 1.6 ± 0.6	5.9 ± 0.4	7.1 ± 0.9	2.8 ± 0.5	6.4 ± 0.4	7.7 ± 1.4	4.23 ± 0.20

Table 4 continued on next page

**Table 4** (*continued*)

Source	Contrast Limit in F110W at Sep. [mas]						
	55–65	75–85	90–110	160–200	250–300	350–400	450–500
2M 1731+2721	52 ± 7	95 ± 9	126 ± 9	69 ± 13	126 ± 5	132 ± 6	87 ± 8
2M 1750+1759	6.5 ± 1.9, 1.00 ± 0.26	13.5 ± 1.3	19.6 ± 1.8	9.3 ± 1.5	14.2 ± 1.8	17.9 ± 1.7	13.5 ± 2.4
2M 1753-6559	76 ± 8	105 ± 8	138 ± 17	76 ± 8	121 ± 15	167 ± 16	101 ± 14
2M 1807+5015	60 ± 7	95 ± 7	115 ± 9	69 ± 12	115 ± 4	115 ± 16	87 ± 8
2M 1936-5502	39 ± 6	59.9 ± 2.8	72 ± 9	39 ± 8	80 ± 11	83 ± 4	57.3 ± 2.7
2M 2002-0521	60 ± 10	105 ± 8	115 ± 10	60 ± 7	115 ± 12	138 ± 10	83 ± 4
2M 2028+0052	50 ± 6	87 ± 10	105 ± 7	52 ± 7	91 ± 7	100 ± 5	62.9 ± 2.9
2M 2036+1051	43 ± 5	79 ± 10	105 ± 7	52 ± 7	100 ± 13	105 ± 4	66 ± 12
2M 2057-0252	9.8 ± 0.5	19.6 ± 2.9	26.0 ± 1.8	12.3 ± 1.4	23.6 ± 3.1	27.2 ± 2.0	17.9 ± 3.3
2M 2104-1037	24.8 ± 3.3	37.6 ± 2.9	55 ± 5	28 ± 4	46 ± 6	55 ± 5	34.5 ± 3.2
2M 2139+0220	38 ± 4	72 ± 10	87 ± 8	38 ± 6	87.0 ± 3.3	95 ± 17	69.0 ± 3.2
2M 2148+4003	7.1 ± 0.9, 1.0 ± 0.4	13.5 ± 2.0	16.3 ± 2.2	7.7 ± 0.8	16.3 ± 1.1	18.8 ± 2.5	11.8 ± 0.5
2M 2152+0937		1.59 ± 0.34	2.54 ± 0.25	1.00 ± 0.23	2.01 ± 0.16	2.78 ± 0.11	3.4 ± 0.6
2M 2204-5646		2.31 ± 0.35	3.4 ± 0.5	1.59 ± 0.32	3.35 ± 0.25	3.7 ± 0.7	3.4 ± 0.6
2M 2224-0158	36 ± 4	59.9 ± 2.5	72 ± 6	37.6 ± 3.1	69 ± 5	79 ± 11	52.2 ± 2.4
2M 2228-4310	50 ± 11	79 ± 16	115 ± 10	60 ± 8	100 ± 10	115 ± 5	80 ± 7
2M 2237+3922	79.2 ± 3.0	138 ± 11	167 ± 6	87 ± 6	145 ± 15	183 ± 7	132 ± 6
2M 2249+3205	18.8 ± 2.7	37.6 ± 3.0	45 ± 4	21.5 ± 1.8	41 ± 4	45 ± 6	32.8 ± 1.5
2M 2252-1730	3.86 ± 0.18, 1.7 ± 0.7	7.1 ± 0.5	8.5 ± 1.2	4.4 ± 0.7	8.5 ± 0.8	9.8 ± 1.3	7.1 ± 1.2
2M 2252-1730	3.37 ± 0.31	5.86 ± 0.25	7.74 ± 0.34	3.7 ± 0.5	6.7 ± 0.7	7.7 ± 0.5	6.5 ± 0.6
2M 2254+3123	39 ± 5	72 ± 6	95 ± 5	49.8 ± 3.2	91 ± 10	95 ± 6	66 ± 6
2M 2255-5713	14.2 ± 2.9	21.5 ± 2.6	31.3 ± 2.1	15.6 ± 1.5	28.5 ± 3.1	31 ± 4	22 ± 4
2M 2325+4251	38 ± 7	65.8 ± 3.0	95 ± 7	45 ± 5	83 ± 4	100 ± 5	66 ± 12
2M 2339+1352	55 ± 7	87 ± 4	115 ± 12	60 ± 8	115 ± 8	126 ± 12	87 ± 8
2M 2351-2537	8.6 ± 1.6	17.9 ± 1.4	17.9 ± 2.4	8.1 ± 1.9	16.3 ± 1.1	18.8 ± 1.5	12.3 ± 2.2
SDSS 0837-0000	8.5 ± 1.9, 1.0 ± 0	16 ± 4	19.6 ± 3.2	10.7 ± 1.6	18.8 ± 3.0	18.8 ± 2.0	10.7 ± 0.5
SDSS 2052-1609		3.35 ± 0.15	4.43 ± 0.21	2.54 ± 0.29	4.6 ± 0.4	5.34 ± 0.35	5.10 ± 0.24

NOTE—Median  $5\sigma$  contrast (within the stated separation range) in 4 of 5 calibrators. No entry indicates no significant detection at that separation is possible. Two entries (at tight separations) is caused by a reduction in sensitivity to equal brightness targets and indicates a significant detection is possible *between* the two values. The diffraction limit ( $\lambda/D$ ) is roughly 95 and 147 mas in F110W and F170M, respectively.

**Table 5.** Individual  $5\sigma$  Contrast Ratio Limits in F170M

Source	Contrast Limit in F170M at Sep. [mas]						
	55–65	75–85	90–110	160–200	250–300	350–400	450–500
2M 0004-4044	6.3 ± 2.6, 2.01 ± 0.21	16.3 ± 2.5, 1.32 ± 0.15	28 ± 5	60 ± 5	26.1 ± 3.0	54.6 ± 2.1	55 ± 10
2M 0024-0158	33 ± 7, 1.59 ± 0.20	66 ± 8, 1.20 ± 0.10	95 ± 13	201 ± 34	105 ± 14	201 ± 22	167 ± 32
2M 0025+4759			1.9 ± 0.5	3.7 ± 0.6	1.39 ± 0.11	3.9 ± 0.4	2.92 ± 0.14
2M 0036+1821	16 ± 4, 1.83 ± 0.09	31 ± 4, 1.45 ± 0.06	60 ± 9	95 ± 6	48 ± 8	105 ± 4	87 ± 17
2M 0045+1634	20.6 ± 1.5, 1.83 ± 0.09	45 ± 7, 1.45 ± 0.16	79 ± 14	126 ± 6	63 ± 5	138 ± 5	115 ± 11
2M 0107+0041	17.1 ± 1.8, 1.75 ± 0.07	38 ± 4, 1.45 ± 0.17	66 ± 7	115 ± 5	54.6 ± 2.3	115 ± 8	100 ± 5
2M 0109+2949	33 ± 7, 1.59 ± 0.10	66 ± 8, 1.20 ± 0.13	138 ± 9	211 ± 33	110 ± 11	231 ± 11	220 ± 40
2M 0123-4240	9.3 ± 1.0, 2.01 ± 0.09	23.6 ± 2.7, 1.59 ± 0.07	38 ± 8	69 ± 5	33 ± 4	72 ± 10	60 ± 11
2M 0144-0716	26 ± 4, 1.59 ± 0.20	55 ± 4, 1.20 ± 0.13	105 ± 15	175 ± 16	83 ± 6	183 ± 7	145 ± 7

*Table 5 continued on next page*

Table 5 (continued)

Source	Contrast Limit in F170M at Sep. [mas]						
	55–65	75–85	90–110	160–200	250–300	350–400	450–500
2M 0147-4954			4.9 ± 1.2, 1.0 ± 0.4	8.5 ± 1.8	4.2 ± 0.8	8.5 ± 2.5	10.4 ± 1.9
2M 0151+1244	18 ± 4, 1.59 ± 0.06	41 ± 5, 1.20 ± 0.10	66 ± 7	126 ± 18	57 ± 7	126 ± 12	115 ± 11
2M 0155+0950		7.1 ± 2.6, 1.75 ± 0.13	12.3 ± 1.9	23.6 ± 1.3	11.2 ± 0.4	24.8 ± 1.2	22.6 ± 1.1
2M 0205-1159			2.66 ± 0.12	5.1 ± 0.8	2.66 ± 0.28	5.6 ± 0.4	5.3 ± 0.9
2M 0207+0000	7.5 ± 1.6, 2.01 ± 0.16	17.9 ± 0.7, 1.59 ± 0.07	31 ± 4	52 ± 5	24.8 ± 2.0	54.6 ± 2.3	52.2 ± 2.4
2M 0213+4444	50 ± 7, 1.59 ± 0.20	115 ± 9, 1.20 ± 0.10	201 ± 29	351 ± 12	167 ± 6	368 ± 27	336 ± 16
2M 0228+1639	7.4 ± 0.6, 2.10 ± 0.08	17.9 ± 1.4, 1.59 ± 0.07	28 ± 6	54.6 ± 2.5	26 ± 4	57 ± 4	50 ± 9
2M 0243-2453	7.7 ± 1.2, 2.10 ± 0.08	20 ± 4, 1.59 ± 0.07	34 ± 4	55 ± 4	23.6 ± 1.7	57 ± 6	47.6 ± 2.2
2M 0251-0352	4.9 ± 0.4, 2.10 ± 0.26	12.3 ± 1.4, 1.59 ± 0.18	21.5 ± 3.3	39.5 ± 3.5	17.9 ± 1.7	41.3 ± 1.6	35 ± 6
2M 0255-4700	14.9 ± 3.3, 1.75 ± 0.07	38 ± 4, 1.32 ± 0.15	60 ± 4	110 ± 5	54.6 ± 2.1	110 ± 5	100 ± 5
2M 0257-3105	23 ± 4, 1.75 ± 0.21	49.8 ± 2.3, 1.45 ± 0.21	87 ± 11	152 ± 14	72.2 ± 3.0	152 ± 15	132 ± 6
2M 0314+1603	34 ± 4, 1.59 ± 0.06	66 ± 10, 1.32 ± 0.15	105 ± 16	183 ± 14	100 ± 7	201 ± 13	167 ± 32
2M 0318-3421	21.5 ± 3.4, 1.75 ± 0.21	45 ± 4, 1.32 ± 0.13	79 ± 5	126 ± 15	63 ± 5	145 ± 15	126 ± 24
2M 0348-6022	20.6 ± 3.3, 1.59 ± 0.07	50 ± 6, 1.20 ± 0.13	72 ± 10	138 ± 7	63 ± 5	139 ± 20	132 ± 6
2M 0355+1133	8.5 ± 1.3, 2.01 ± 0.09	19.6 ± 2.3, 1.45 ± 0.07	34.3 ± 3.1	60 ± 7	29.9 ± 1.4	60 ± 7	57.3 ± 2.7
2M 0415-0935	5.6 ± 1.5, 2.21 ± 0.32	13.5 ± 0.6, 1.59 ± 0.07	24 ± 5	45.3 ± 1.6	22.6 ± 2.4	47.6 ± 3.5	43.3 ± 2.0
2M 0423-0414	4.23 ± 0.20, 2.42 ± 0.11	12.3 ± 2.8, 1.59 ± 0.12	18 ± 4	37.6 ± 3.1	15.6 ± 1.3	34 ± 5	29.9 ± 1.4
2M 0423-0414			3.4 ± 0.7, 1.0 ± 0.4	6.7 ± 1.4	3.5 ± 0.6	7.4 ± 0.8	7.7 ± 1.4
2M 0429-3123				1.75 ± 0.09	1.10 ± 0.10	1.83 ± 0.14	2.21 ± 0.10
2M 0439-2353	46 ± 8, 1.52 ± 0.07	95 ± 4, 1.00 ± 0.15	167 ± 16	292 ± 22	138 ± 13	306 ± 14	280 ± 40
2M 0443+0002	43 ± 6, 1.52 ± 0.07	87 ± 10, 1.10 ± 0.08	138 ± 21	266 ± 17	126 ± 17	279 ± 21	240 ± 50
2M 0445-3048	12 ± 4, 1.83 ± 0.15	31 ± 7, 1.32 ± 0.10	50 ± 6	91 ± 6	34.3 ± 1.4	91 ± 14	83 ± 4
2M 0500+0330	38 ± 4, 1.59 ± 0.06	72 ± 7, 1.20 ± 0.10	115 ± 16	242 ± 20	105 ± 10	231 ± 19	254 ± 12
2M 0518-2828	6.1 ± 1.1, 2.21 ± 0.10	16.3 ± 2.4, 1.59 ± 0.07	28 ± 4	54.6 ± 3.5	26.0 ± 1.7	52.2 ± 2.4	50 ± 9
2M 0518-2828	5.1 ± 1.5, 2.21 ± 0.32	14.8 ± 1.8, 1.59 ± 0.12	28 ± 5	54.6 ± 1.8	26.0 ± 2.7	54.6 ± 2.1	44 ± 6
2M 0523-1403	36 ± 5, 1.59 ± 0.06	72 ± 13, 1.20 ± 0.13	126 ± 18	231 ± 15	105 ± 12	221 ± 9	231 ± 11
2M 0624+2325	7.4 ± 1.4, 2.21 ± 0.16	17.9 ± 2.6, 1.59 ± 0.12	24 ± 4	50 ± 7	24.8 ± 1.2	45 ± 6	41 ± 8
2M 0624-4521	31 ± 7, 1.59 ± 0.06	72 ± 5, 1.32 ± 0.15	95 ± 15	201 ± 7	87 ± 9	192 ± 9	183 ± 35
2M 0652+4710	13.6 ± 2.0, 1.75 ± 0.07	31.3 ± 3.0, 1.45 ± 0.06	55 ± 8	95 ± 6	50 ± 5	100 ± 5	91 ± 4
2M 0700+3157		2.92 ± 0.14, 2.23 ± 0.31	5.9 ± 2.1	14.2 ± 2.3	5.9 ± 1.5	12.9 ± 1.3	9.8 ± 0.5
2M 0727+1710		3.1 ± 0.7, 2.1 ± 0.5	5.9 ± 0.9	10.2 ± 0.7	4.43 ± 0.29	10.2 ± 0.7	9.3 ± 1.6
2M 0755+2212	9.8 ± 2.1, 1.83 ± 0.15	23.6 ± 1.8, 1.45 ± 0.11	34 ± 5	66 ± 6	34.3 ± 2.3	66 ± 8	62.9 ± 2.9
2M 0825+2115	7.1 ± 0.8, 2.10 ± 0.08	17.9 ± 2.0, 1.59 ± 0.07	31 ± 5	60 ± 4	27 ± 6	59.9 ± 2.3	50 ± 9
2M 0830+4828	33 ± 6, 1.67 ± 0.08	66 ± 6, 1.20 ± 0.18	115 ± 22	183 ± 22	100 ± 7	221 ± 8	194 ± 27
2M 0835-0819	27.2 ± 2.8, 1.59 ± 0.20	72 ± 6, 1.32 ± 0.15	105 ± 13	192 ± 18	87 ± 6	183 ± 16	183 ± 35
2M 0847-1532	27.2 ± 2.8, 1.59 ± 0.07	55 ± 12, 1.45 ± 0.12	105 ± 7	175 ± 13	83 ± 7	202 ± 34	175 ± 8
2M 0850+1057		3.6 ± 0.8, 2.42 ± 0.11	5.3 ± 1.1	10.2 ± 0.4	4.1 ± 0.5	11.2 ± 0.7	11.8 ± 0.5
2M 0859-1949	18.8 ± 2.5, 1.75 ± 0.07	37.6 ± 3.0, 1.32 ± 0.15	66 ± 11	115 ± 5	60 ± 4	132 ± 14	110 ± 5
2M 0908+5032	6.7 ± 1.2, 2.01 ± 0.25	14.8 ± 1.1, 1.45 ± 0.06	28 ± 4	45.3 ± 3.5	24.8 ± 1.2	49.8 ± 3.3	47.6 ± 2.2
2M 0911+7401	43 ± 6, 1.59 ± 0.06	87 ± 4, 1.20 ± 0.10	138 ± 18	254 ± 17	121 ± 10	266 ± 10	243 ± 23
2M 0915+0422				1.92 ± 0.18		1.75 ± 0.07	2.03 ± 0.28
2M 0921-2104	23.6 ± 2.5, 1.67 ± 0.08	50 ± 4, 1.32 ± 0.19	87 ± 13	152 ± 14	69 ± 6	167 ± 12	121 ± 6
2M 0926+5847	7.4 ± 1.4, 1.83 ± 0.15	17.9 ± 2.7, 1.20 ± 0.12	34 ± 4	55 ± 7	24.8 ± 1.2	53 ± 7	55 ± 10
2M 1021-0304		2.5 ± 0.6, 2.1 ± 0.5	4.9 ± 0.8	8.9 ± 2.4	4.1 ± 0.6	10.2 ± 0.8	10.2 ± 1.8
2M 1022+5825	22.6 ± 2.4, 1.67 ± 0.08	45 ± 6, 1.32 ± 0.11	79 ± 10	138 ± 14	66 ± 6	159 ± 12	145 ± 7
2M 1025+3212	12.3 ± 2.3, 1.92 ± 0.08	24 ± 7, 1.45 ± 0.11	45 ± 6	79 ± 6	37.6 ± 2.5	79.2 ± 3.3	75.7 ± 3.5

Table 5 continued on next page



Table 5 (continued)

Source	Contrast Limit in F170M at Sep. [mas]						
	55–65	75–85	90–110	160–200	250–300	350–400	450–500
2M 1043+2225	27 ± 4, 1.67 ± 0.08	66 ± 7, 1.32 ± 0.15	105 ± 16	183 ± 10	83 ± 7	192 ± 14	153 ± 14
2M 1045-0149	23.6 ± 3.2, 1.75 ± 0.12	45.3 ± 3.5, 1.45 ± 0.06	66 ± 12	138 ± 7	72.2 ± 2.8	145 ± 11	126 ± 24
2M 1048+0111	18.0 ± 2.6, 1.52 ± 0.07	50 ± 7, 1.10 ± 0.08	66 ± 12	138 ± 14	57 ± 5	138 ± 5	133 ± 19
2M 1051+5613	20.6 ± 2.1, 1.75 ± 0.21	45 ± 4, 1.32 ± 0.06	72 ± 9	121 ± 6	62.9 ± 2.9	126 ± 9	115 ± 11
2M 1058-1548	48 ± 6, 1.67 ± 0.08	105 ± 12, 1.32 ± 0.15	167 ± 22	292 ± 27	138 ± 15	306 ± 32	279 ± 13
2M 1104+1959	14.2 ± 2.4, 1.67 ± 0.08	34.3 ± 1.6, 1.20 ± 0.06	55 ± 11	95.5 ± 3.2	45 ± 5	100 ± 10	92 ± 13
2M 1108+6830	12.3 ± 1.2, 1.75 ± 0.21	23.6 ± 2.9, 1.45 ± 0.12	50 ± 8	79 ± 4	39.5 ± 2.9	87 ± 4	75.7 ± 3.5
2M 1110+0116	5.1 ± 1.6, 2.1 ± 0.5	13.5 ± 1.3, 1.45 ± 0.11	28 ± 4	45 ± 5	21.5 ± 2.1	45.3 ± 1.7	45 ± 9
2M 1155-3727	31 ± 6, 1.59 ± 0.06	66 ± 8, 1.10 ± 0.08	105 ± 13	211 ± 21	105 ± 12	192 ± 14	192 ± 9
2M 1203+0015	16.4 ± 2.0, 1.67 ± 0.08	34.3 ± 2.6, 1.32 ± 0.11	60 ± 10	105 ± 7	52 ± 4	110 ± 11	100 ± 5
2M 1213-0432	7.8 ± 2.0, 1.8 ± 0.4	16.3 ± 2.0, 1.20 ± 0.09	28.5 ± 2.4	55 ± 4	27.2 ± 2.2	57 ± 4	57.3 ± 2.7
2M 1217-0311	5.9 ± 1.4, 1.92 ± 0.15	16.3 ± 1.9, 1.45 ± 0.06	26 ± 4	50 ± 4	23.6 ± 0.9	50 ± 7	48 ± 7
2M 1221+0257	55 ± 10, 1.59 ± 0.06	115 ± 5, 1.10 ± 0.08	201 ± 17	351 ± 12	175 ± 8	368 ± 27	336 ± 16
2M 1254-0122	8.9 ± 1.3, 1.83 ± 0.09	21.5 ± 3.2, 1.45 ± 0.17	38 ± 5	66 ± 5	31.3 ± 2.8	66 ± 4	62.9 ± 2.9
2M 1300+1912	31 ± 5, 1.59 ± 0.07	66 ± 12, 1.32 ± 0.15	105 ± 18	192 ± 23	96 ± 9	183 ± 12	184 ± 17
2M 1421+1827	39.5 ± 2.9, 1.67 ± 0.08	87 ± 14, 1.32 ± 0.10	138 ± 10	266 ± 17	126 ± 12	254 ± 12	240 ± 50
2M 1425-3650	60 ± 9, 1.59 ± 0.06	115 ± 9, 1.20 ± 0.13	201 ± 14	351 ± 12	183 ± 7	368 ± 27	320 ± 60
2M 1428+5923	30 ± 6, 1.67 ± 0.08	79 ± 9, 1.20 ± 0.09	105 ± 12	221 ± 21	100 ± 15	211 ± 10	200 ± 40
2M 1439+1929	42 ± 9, 1.59 ± 0.07	79 ± 8, 1.32 ± 0.15	138 ± 10	254 ± 23	126 ± 8	266 ± 18	243 ± 23
2M 1448+1031	17.1 ± 2.5, 1.59 ± 0.07	37.6 ± 2.9, 1.32 ± 0.15	66 ± 5	110 ± 10	55 ± 4	115 ± 8	105 ± 20
2M 1503+2525	10.2 ± 1.4, 1.75 ± 0.07	21.5 ± 2.6, 1.45 ± 0.06	38 ± 6	66 ± 4	29 ± 5	72 ± 5	63 ± 9
2M 1503+2525	13.6 ± 1.9, 1.83 ± 0.14	28.5 ± 2.2, 1.32 ± 0.10	50 ± 6	87 ± 6	39.5 ± 1.8	83 ± 9	73 ± 7
2M 1506+1321	39 ± 6, 1.75 ± 0.07	87 ± 12, 1.32 ± 0.10	138 ± 16	266 ± 21	121 ± 13	243 ± 23	240 ± 50
2M 1507-1627	13.5 ± 2.1, 1.67 ± 0.08	28 ± 4, 1.32 ± 0.11	55 ± 10	100 ± 9	47.6 ± 3.5	96 ± 11	100 ± 5
2M 1515+4847	20.6 ± 3.5, 1.67 ± 0.08	45 ± 5, 1.32 ± 0.19	79 ± 7	138 ± 22	63 ± 5	139 ± 13	132 ± 6
2M 1534+1615			4.9 ± 0.6	9.3 ± 0.6	4.0 ± 0.5	9.3 ± 0.4	8.9 ± 0.4
2M 1539-0520	7.4 ± 1.3, 2.10 ± 0.09	17.9 ± 2.6, 1.59 ± 0.07	31.3 ± 2.8	57 ± 6	26.0 ± 1.1	55 ± 6	52.2 ± 2.4
2M 1552+2948	5.9 ± 0.7, 2.10 ± 0.16	12.3 ± 1.5, 1.59 ± 0.07	23.6 ± 2.5	43.3 ± 3.1	20.6 ± 2.1	45.3 ± 1.7	41 ± 8
2M 1553+1532			2.03 ± 0.28	4.2 ± 0.5	1.45 ± 0.31	4.9 ± 0.7	4.65 ± 0.22
2M 1624+0029	5.9 ± 0.9, 2.10 ± 0.14	13.5 ± 0.6, 1.45 ± 0.11	28 ± 5	49.8 ± 2.1	21.5 ± 2.3	45.3 ± 1.9	50 ± 5
2M 1658+7027	55 ± 5, 1.59 ± 0.20	105 ± 16, 1.32 ± 0.15	201 ± 19	351 ± 15	167 ± 23	336 ± 27	321 ± 30
2M 1705-0516	10.7 ± 2.1, 1.92 ± 0.08	26.0 ± 2.1, 1.45 ± 0.07	45 ± 5	79.2 ± 3.3	38 ± 5	79 ± 6	69.0 ± 3.2
2M 1707-0558				1.83 ± 0.22	1.05 ± 0.05	1.83 ± 0.09	2.11 ± 0.20
2M 1721+3344	33 ± 4, 1.67 ± 0.08	79 ± 6, 1.20 ± 0.09	115 ± 20	221 ± 17	100 ± 8	211 ± 10	202 ± 19
2M 1728+3948			2.1 ± 0.4	4.4 ± 0.9	1.68 ± 0.32	4.6 ± 0.7	3.37 ± 0.31
2M 1731+2721	48 ± 9, 1.52 ± 0.07	115 ± 5, 1.10 ± 0.08	201 ± 21	320 ± 13	145 ± 7	351 ± 26	306 ± 14
2M 1750+1759	7.4 ± 0.5, 1.92 ± 0.08	16.3 ± 1.6, 1.59 ± 0.07	31 ± 7	54.6 ± 2.9	24.8 ± 3.1	63 ± 10	56 ± 10
2M 1753-6559	38 ± 8, 1.59 ± 0.07	87 ± 7, 1.20 ± 0.13	138 ± 23	242 ± 16	110 ± 11	242 ± 10	220 ± 40
2M 1807+5015	44 ± 8, 1.59 ± 0.20	95 ± 7, 1.32 ± 0.11	167 ± 29	266 ± 35	139 ± 17	306 ± 32	280 ± 40
2M 1936-5502	22.8 ± 3.2, 1.75 ± 0.07	50 ± 6, 1.32 ± 0.06	79 ± 12	152 ± 10	73 ± 8	152 ± 10	127 ± 12
2M 2002-0521	34 ± 4, 1.75 ± 0.07	79 ± 6, 1.45 ± 0.17	115 ± 15	221 ± 14	105 ± 14	221 ± 8	200 ± 40
2M 2028+0052	43 ± 5, 1.59 ± 0.20	87 ± 10, 1.32 ± 0.15	138 ± 16	242 ± 16	126 ± 5	279 ± 21	240 ± 50
2M 2036+1051	41 ± 4, 1.59 ± 0.20	87 ± 10, 1.10 ± 0.13	138 ± 10	242 ± 27	126 ± 5	254 ± 19	240 ± 50
2M 2057-0252	11.8 ± 1.7, 1.92 ± 0.13	24 ± 4, 1.59 ± 0.07	50 ± 8	91 ± 6	43.3 ± 2.0	91 ± 7	91 ± 4
2M 2104-1037	14.2 ± 3.4, 1.83 ± 0.15	34 ± 4, 1.45 ± 0.07	54.6 ± 3.2	105 ± 9	45 ± 4	105 ± 14	83 ± 4
2M 2139+0220	9.9 ± 2.0, 2.01 ± 0.15	23.6 ± 2.9, 1.45 ± 0.11	38 ± 6	72 ± 5	34.3 ± 1.4	73 ± 7	69.0 ± 3.2

Table 5 continued on next page

**Table 5** (*continued*)

Source	Contrast Limit in F170M at Sep. [mas]						
	55–65	75–85	90–110	160–200	250–300	350–400	450–500
2M 2148+4003	$7.1 \pm 1.7, 2.10 \pm 0.15$	$19.6 \pm 2.3, 1.45 \pm 0.11$	$31.3 \pm 3.5$	$55 \pm 5$	$28.5 \pm 2.1$	$63 \pm 5$	$53 \pm 7$
2M 2152+0937			$2.1 \pm 0.4$	$3.7 \pm 0.6$	$1.5 \pm 0.5$	$4.4 \pm 0.8$	$3.86 \pm 0.18$
2M 2204-5646			$4.9 \pm 0.8$	$10.2 \pm 0.8$	$5.1 \pm 0.9$	$11.2 \pm 2.3$	$9.8 \pm 0.5$
2M 2224-0158	$30 \pm 5, 1.59 \pm 0.07$	$60 \pm 6, 1.32 \pm 0.11$	$95 \pm 10$	$167 \pm 18$	$79 \pm 12$	$159 \pm 7$	$159 \pm 7$
2M 2228-4310	$6.5 \pm 1.5, 2.21 \pm 0.32$	$16.3 \pm 0.7, 1.59 \pm 0.07$	$28 \pm 4$	$49.8 \pm 1.8$	$24.8 \pm 1.8$	$47.6 \pm 2.2$	$50 \pm 9$
2M 2237+3922	$57 \pm 6, 1.59 \pm 0.06$	$115 \pm 9, 1.20 \pm 0.13$	$183 \pm 28$	$351 \pm 15$	$167 \pm 23$	$368 \pm 27$	$320 \pm 60$
2M 2249+3205	$15.6 \pm 2.5, 1.75 \pm 0.07$	$34.3 \pm 2.7, 1.45 \pm 0.06$	$55 \pm 7$	$87 \pm 8$	$45.3 \pm 3.0$	$91 \pm 7$	$91 \pm 4$
2M 2252-1730		$4.4 \pm 0.8, 2.31 \pm 0.26$	$7.7 \pm 2.2$	$12.3 \pm 2.3$	$7.4 \pm 0.8$	$14.2 \pm 2.5$	$14.8 \pm 2.7$
2M 2252-1730	$4.9 \pm 1.2, 2.3 \pm 0.6$	$11.2 \pm 2.4, 1.45 \pm 0.30$	$18 \pm 4$	$34.3 \pm 1.8$	$14.2 \pm 0.7$	$33 \pm 4$	$29.9 \pm 1.4$
2M 2254+3123	$5.6 \pm 1.5, 2.21 \pm 0.29$	$14.8 \pm 1.4, 1.45 \pm 0.06$	$28 \pm 6$	$52 \pm 4$	$22.6 \pm 1.8$	$50 \pm 5$	$50 \pm 5$
2M 2255-5713		$3.7 \pm 0.6, 2.01 \pm 0.09$	$7.7 \pm 2.8$	$17.1 \pm 2.8$	$7.1 \pm 2.1$	$16.4 \pm 1.9$	$12.9 \pm 0.6$
2M 2325+4251	$5.3 \pm 0.8, 2.31 \pm 0.18$	$12.3 \pm 0.6, 1.45 \pm 0.14$	$21.5 \pm 2.9$	$37.6 \pm 3.5$	$18.8 \pm 1.5$	$43.3 \pm 2.0$	$36.0 \pm 1.7$
2M 2339+1352	$7.9 \pm 1.7, 2.21 \pm 0.10$	$17.9 \pm 0.8, 1.75 \pm 0.07$	$31.3 \pm 3.3$	$54.6 \pm 3.5$	$27.2 \pm 2.0$	$60 \pm 6$	$48 \pm 7$
2M 2351-2537	$6.4 \pm 1.6, 2.01 \pm 0.15$	$14.8 \pm 2.6, 1.45 \pm 0.11$	$26 \pm 6$	$55 \pm 5$	$26.1 \pm 3.0$	$52 \pm 4$	$52.2 \pm 2.4$
SDSS 0837-0000	$11.2 \pm 1.5, 1.92 \pm 0.07$	$26 \pm 5, 1.45 \pm 0.11$	$41 \pm 9$	$83 \pm 7$	$38 \pm 4$	$87 \pm 6$	$83 \pm 4$
SDSS 2052-1609		$4.0 \pm 0.7, 2.42 \pm 0.11$	$7.1 \pm 0.9$	$12.9 \pm 1.5$	$5.1 \pm 0.4$	$13.6 \pm 1.6$	$10.7 \pm 0.5$

NOTE—Median  $5\sigma$  contrast (within the stated separation range) in 4 of 5 calibrators. No entry indicates no significant detection at that separation is possible. Two entries (at tight separations) is caused by a reduction in sensitivity to equal brightness targets and indicates a significant detection is possible *between* the two values. The diffraction limit ( $\lambda/D$ ) is roughly 95 and 147 mas in F110W and F170M, respectively.

**Table 6.** Individual  $5\sigma$  Contrast Ratio Limits at Tight Separations

Source	F110W Limit at Sep. [mas]			F170M Limit at Sep. [mas]	
	15–25	25–35	35–45	25–35	35–45
2M 0024-0158	$4.4 \pm 1.1, 3.1 \pm 0.7$	$8 \pm 4, 2.1 \pm 0.4$	$24 \pm 6, 1.67 \pm 0.08$	$5.9 \pm 1.4, 2.5 \pm 0.6$	$8.9 \pm 2.3, 2.10 \pm 0.30$
2M 0036+1821		$5.3 \pm 2.2, 2.54 \pm 0.27$	$12 \pm 4, 1.92 \pm 0.08$		$4.4 \pm 0.4, 2.92 \pm 0.14$
2M 0045+1634	$4.0 \pm 1.0, 3.7 \pm 0.9$	$9 \pm 4, 2.1 \pm 0.4$	$20.6 \pm 3.5, 1.75 \pm 0.09$		$5.9 \pm 1.0, 2.54 \pm 0.11$
2M 0107+0041		$6.4 \pm 1.0, 2.31 \pm 0.19$	$12.3 \pm 3.2, 2.01 \pm 0.14$		$5.9 \pm 0.9, 2.54 \pm 0.12$
2M 0109+2949		$7.7 \pm 3.2, 2.31 \pm 0.28$	$20 \pm 6, 1.67 \pm 0.08$	$4.9 \pm 1.2, 2.9 \pm 0.4$	$9.9 \pm 3.2, 2.21 \pm 0.18$
2M 0123-4240			$3.7 \pm 0.9, 2.5 \pm 0.6$		
2M 0144-0716		$7.7 \pm 1.8, 2.1 \pm 0.4$	$14 \pm 4, 1.75 \pm 0.11$		$7.1 \pm 1.8, 2.10 \pm 0.12$
2M 0151+1244		$6.2 \pm 1.8, 2.42 \pm 0.25$	$13.5 \pm 3.1, 1.83 \pm 0.09$		$7.1 \pm 1.2, 2.21 \pm 0.10$
2M 0207+0000			$2.8 \pm 0.7, 2.5 \pm 0.6$		
2M 0213+4444	$6.3 \pm 1.8, 2.55 \pm 0.32$	$14 \pm 5, 1.92 \pm 0.19$	$31 \pm 7, 1.59 \pm 0.06$	$8.5 \pm 3.2, 2.3 \pm 0.4$	$18 \pm 4, 1.92 \pm 0.09$
2M 0228+1639		$4.4 \pm 0.5, 2.54 \pm 0.19$	$9.3 \pm 2.8, 2.10 \pm 0.16$		
2M 0243-2453			$4.0 \pm 1.6, 2.31 \pm 0.21$		
2M 0255-4700		$10.2 \pm 3.1, 2.10 \pm 0.22$	$24 \pm 4, 1.67 \pm 0.08$		$4.65 \pm 0.22, 2.5 \pm 0.4$
2M 0257-3105		$5.3 \pm 0.9, 2.31 \pm 0.35$	$10.7 \pm 2.9, 1.92 \pm 0.10$		$6.4 \pm 1.0, 2.31 \pm 0.22$
2M 0314+1603		$7.7 \pm 2.2, 2.31 \pm 0.21$	$16 \pm 4, 1.75 \pm 0.09$	$4.4 \pm 1.1, 2.8 \pm 0.7$	$7.7 \pm 3.4, 2.1 \pm 0.4$
2M 0318-3421		$3.7 \pm 0.9, 3.1 \pm 0.7$	$8.5 \pm 2.7, 2.01 \pm 0.24$		$5.9 \pm 0.9, 2.31 \pm 0.11$
2M 0348-6022		$9.3 \pm 1.5, 2.10 \pm 0.09$	$16 \pm 4, 1.75 \pm 0.07$		$6.4 \pm 0.9, 2.54 \pm 0.23$
2M 0355+1133			$5.9 \pm 1.9, 2.21 \pm 0.23$		
2M 0415-0935			$4.23 \pm 0.20, 2.8 \pm 0.5$		
2M 0423-0414			$18 \pm 5, 12.3 \pm 3.1$		

*Table 6 continued on next page*

Table 6 (continued)

Source	F110W Limit at Sep. [mas]			F170M Limit at Sep. [mas]	
	15–25	25–35	35–45	25–35	35–45
2M 0439-2353		$9.3 \pm 3.4, 2.01 \pm 0.31$	$23 \pm 4, 1.59 \pm 0.07$	$8.9 \pm 1.4, 2.21 \pm 0.18$	$14 \pm 5, 1.92 \pm 0.12$
2M 0443+0002	$3.4 \pm 0.8, 3.1 \pm 0.7$	$9 \pm 4, 2.10 \pm 0.20$	$25 \pm 6, 1.75 \pm 0.07$	$5.6 \pm 1.1, 2.66 \pm 0.28$	$13.6 \pm 2.6, 1.92 \pm 0.18$
2M 0500+0330		$6.4 \pm 2.7, 2.54 \pm 0.35$	$20 \pm 5, 1.75 \pm 0.09$	$4.4 \pm 0.9, 2.78 \pm 0.31$	$11.8 \pm 3.1, 2.01 \pm 0.22$
2M 0523-1403		$9 \pm 4, 2.10 \pm 0.29$	$21 \pm 4, 1.67 \pm 0.08$	$4.6 \pm 1.0, 2.79 \pm 0.35$	$10.7 \pm 2.0, 2.10 \pm 0.09$
2M 0624-4521		$8.5 \pm 2.3, 2.1 \pm 0.4$	$18 \pm 4, 1.67 \pm 0.12$	$4.43 \pm 0.19, 3.05 \pm 0.13$	$10.2 \pm 1.9, 2.10 \pm 0.20$
2M 0652+4710			$4.1 \pm 0.8, 2.32 \pm 0.22$		$4.9 \pm 0.9, 2.8 \pm 0.5$
2M 0700+3157			$4.0 \pm 0.6, 2.54 \pm 0.11$		
2M 0727+1710			$3.4 \pm 0.8, 2.5 \pm 0.6$		
2M 0755+2212		$8 \pm 4, 2.10 \pm 0.27$	$20.6 \pm 3.4, 1.75 \pm 0.11$		
2M 0825+2115			$4.4 \pm 1.6, 2.54 \pm 0.29$		
2M 0830+4828		$7.7 \pm 2.0, 2.3 \pm 0.4$	$16 \pm 4, 1.75 \pm 0.09$	$5.9 \pm 1.4, 2.5 \pm 0.6$	$9.3 \pm 1.6, 2.21 \pm 0.15$
2M 0835-0819		$6.4 \pm 2.2, 2.31 \pm 0.24$	$16 \pm 4, 1.83 \pm 0.12$		$8.5 \pm 2.1, 2.10 \pm 0.14$
2M 0847-1532		$7.8 \pm 3.0, 2.01 \pm 0.27$	$16 \pm 5, 1.59 \pm 0.10$		$8.1 \pm 1.7, 2.10 \pm 0.23$
2M 0859-1949		$7.7 \pm 2.2, 2.10 \pm 0.24$	$16.3 \pm 3.4, 1.75 \pm 0.06$		$5.9 \pm 1.4, 2.54 \pm 0.19$
2M 0908+5032		$8.2 \pm 2.1, 2.01 \pm 0.24$	$16 \pm 4, 1.67 \pm 0.08$		
2M 0911+7401		$8.5 \pm 3.2, 2.10 \pm 0.21$	$23 \pm 4, 1.75 \pm 0.11$	$6.1 \pm 0.5, 2.5 \pm 0.4$	$12.3 \pm 3.1, 2.01 \pm 0.14$
2M 0921-2104		$6 \pm 4, 2.31 \pm 0.26$	$18 \pm 5, 1.75 \pm 0.11$		$7.7 \pm 1.9, 2.10 \pm 0.32$
2M 1022+5825		$10.3 \pm 2.5, 2.10 \pm 0.20$	$24 \pm 7, 1.67 \pm 0.12$		$6.4 \pm 1.5, 2.31 \pm 0.18$
2M 1025+3212			$6.7 \pm 1.5, 2.10 \pm 0.29$		$3.7 \pm 0.9, 3.1 \pm 0.7$
2M 1043+2225		$6.5 \pm 1.1, 2.21 \pm 0.18$	$14 \pm 5, 1.83 \pm 0.13$	$4.0 \pm 1.0, 3.1 \pm 0.7$	$8.9 \pm 2.1, 2.21 \pm 0.27$
2M 1045-0149		$4.9 \pm 0.7, 2.54 \pm 0.18$	$11 \pm 4, 1.92 \pm 0.25$		$6.5 \pm 1.7, 2.42 \pm 0.35$
2M 1048+0111			$4.4 \pm 1.9, 2.54 \pm 0.25$		$5.6 \pm 1.8, 2.4 \pm 0.4$
2M 1051+5613		$7.8 \pm 3.1, 2.3 \pm 0.4$	$17 \pm 5, 1.75 \pm 0.08$		$5.9 \pm 1.5, 2.54 \pm 0.28$
2M 1058-1548	$4.4 \pm 1.7, 3.05 \pm 0.35$	$12 \pm 5, 2.10 \pm 0.24$	$34 \pm 8, 1.59 \pm 0.07$	$7.7 \pm 2.2, 2.54 \pm 0.21$	$15 \pm 4, 2.10 \pm 0.13$
2M 1104+1959		$5.3 \pm 0.7, 2.21 \pm 0.10$	$11 \pm 4, 1.75 \pm 0.13$		$5.1 \pm 0.7, 2.55 \pm 0.24$
2M 1108+6830		$8 \pm 4, 2.10 \pm 0.27$	$22 \pm 5, 1.67 \pm 0.08$		
2M 1110+0116		$5.3 \pm 2.1, 2.54 \pm 0.34$	$13.5 \pm 2.5, 2.01 \pm 0.09$		
2M 1155-3727	$3.7 \pm 0.9, 3.4 \pm 0.8$	$9.3 \pm 2.3, 2.10 \pm 0.33$	$19 \pm 5, 1.75 \pm 0.07$	$4.9 \pm 0.5, 2.92 \pm 0.14$	$9.8 \pm 1.9, 2.10 \pm 0.13$
2M 1203+0015	$4.4 \pm 1.1, 3.1 \pm 0.7$	$11 \pm 4, 2.10 \pm 0.15$	$26 \pm 7, 1.67 \pm 0.08$		$4.4 \pm 0.5, 2.78 \pm 0.21$
2M 1213-0432		$8.5 \pm 2.3, 2.1 \pm 0.4$	$18.8 \pm 2.8, 1.75 \pm 0.07$		
2M 1217-0311		$8 \pm 4, 2.3 \pm 0.4$	$21.5 \pm 2.5, 1.75 \pm 0.08$		
2M 1221+0257	$5.9 \pm 0.9, 2.54 \pm 0.12$	$14 \pm 4, 1.92 \pm 0.15$	$29 \pm 8, 1.75 \pm 0.07$	$7.7 \pm 2.4, 2.5 \pm 0.4$	$19 \pm 4, 1.92 \pm 0.07$
2M 1254-0122			$4.1 \pm 0.4, 2.92 \pm 0.14$		
2M 1300+1912		$9.3 \pm 2.8, 2.1 \pm 0.4$	$18 \pm 6, 1.75 \pm 0.11$	$5.3 \pm 1.3, 2.8 \pm 0.7$	$8.1 \pm 1.2, 2.31 \pm 0.19$
2M 1421+1827		$10.2 \pm 3.2, 2.10 \pm 0.26$	$22 \pm 4, 1.75 \pm 0.07$	$5.3 \pm 1.0, 2.78 \pm 0.21$	$13 \pm 4, 2.10 \pm 0.14$
2M 1425-3650	$5.9 \pm 1.9, 2.78 \pm 0.22$	$14 \pm 5, 1.92 \pm 0.31$	$34 \pm 7, 1.67 \pm 0.08$	$8.5 \pm 2.4, 2.31 \pm 0.16$	$21 \pm 5, 1.92 \pm 0.18$
2M 1428+5923		$7.7 \pm 2.7, 2.10 \pm 0.20$	$19 \pm 5, 1.67 \pm 0.08$	$5.3 \pm 1.3, 2.8 \pm 0.7$	$9.9 \pm 3.5, 2.10 \pm 0.30$
2M 1439+1929	$5.4 \pm 1.0, 2.66 \pm 0.12$	$12 \pm 5, 1.92 \pm 0.22$	$27 \pm 6, 1.59 \pm 0.10$	$5.9 \pm 1.4, 2.66 \pm 0.28$	$13 \pm 4, 2.01 \pm 0.14$
2M 1448+1031		$10.2 \pm 3.4, 2.10 \pm 0.29$	$25 \pm 6, 1.75 \pm 0.07$		$5.4 \pm 0.5, 2.42 \pm 0.11$
2M 1503+2525			$3.69 \pm 0.34, 2.92 \pm 0.14$		
2M 1503+2525			$4.0 \pm 1.2, 1.92 \pm 0.26$		
2M 1506+1321		$8.5 \pm 2.0, 1.92 \pm 0.17$	$17 \pm 4, 1.75 \pm 0.07$	$5.4 \pm 0.5, 2.66 \pm 0.12$	$14 \pm 4, 2.10 \pm 0.13$
2M 1507-1627			$4.4 \pm 1.1, 2.3 \pm 0.6$		
2M 1515+4847		$5.9 \pm 2.0, 2.31 \pm 0.30$	$14 \pm 5, 1.75 \pm 0.11$		$6.4 \pm 2.1, 2.54 \pm 0.27$
2M 1552+2948		$4.0 \pm 1.0, 2.5 \pm 0.6$	$8.9 \pm 2.4, 2.01 \pm 0.33$		
2M 1624+0029		$9.3 \pm 2.3, 2.10 \pm 0.35$	$16.4 \pm 3.2, 1.75 \pm 0.08$		

Table 6 continued on next page

Table 6 (*continued*)

Source	F110W Limit at Sep. [mas]			F170M Limit at Sep. [mas]	
	15–25	25–35	35–45	25–35	35–45
2M 1658+7027		9.3 ± 3.0, 2.10 ± 0.35	22 ± 6, 1.75 ± 0.07	7.4 ± 1.5, 2.54 ± 0.16	16 ± 4, 2.01 ± 0.14
2M 1721+3344		10.4 ± 3.4, 2.10 ± 0.25	21 ± 4, 1.75 ± 0.06	5.1 ± 1.0, 2.7 ± 0.5	10 ± 4, 2.21 ± 0.18
2M 1731+2721		12 ± 4, 2.10 ± 0.25	24 ± 5, 1.67 ± 0.08	7.1 ± 0.6, 2.31 ± 0.11	16 ± 4, 1.92 ± 0.06
2M 1753-6559	5.60 ± 0.26, 2.5 ± 0.4	11.2 ± 3.4, 2.10 ± 0.14	26 ± 7, 1.75 ± 0.07	5.86 ± 0.27, 2.54 ± 0.24	11.8 ± 2.5, 2.10 ± 0.09
2M 1807+5015		10.2 ± 2.4, 2.10 ± 0.21	21 ± 5, 1.75 ± 0.09	6.1 ± 1.5, 2.66 ± 0.18	15.6 ± 2.4, 1.92 ± 0.07
2M 1936-5502		5.9 ± 1.3, 2.31 ± 0.31	12.9 ± 1.9, 1.92 ± 0.12		6.5 ± 1.5, 2.42 ± 0.18
2M 2002-0521	5.3 ± 1.3, 2.5 ± 0.6	8.5 ± 3.4, 2.10 ± 0.30	21 ± 7, 1.75 ± 0.06	5.10 ± 0.24, 2.79 ± 0.26	10.2 ± 2.8, 2.21 ± 0.20
2M 2028+0052		8.3 ± 2.9, 2.2 ± 0.4	18 ± 4, 1.75 ± 0.09	6.1 ± 0.6, 2.54 ± 0.17	11.2 ± 2.5, 2.10 ± 0.13
2M 2036+1051		6.9 ± 3.4, 2.4 ± 0.6	16.3 ± 3.4, 1.75 ± 0.07	5.9 ± 1.2, 2.5 ± 0.5	11.9 ± 3.3, 2.01 ± 0.14
2M 2057-0252			4.3 ± 1.0, 2.32 ± 0.22		4.9 ± 1.2, 2.5 ± 0.6
2M 2104-1037		3.7 ± 0.9, 2.5 ± 0.6	8.2 ± 2.3, 1.9 ± 0.4		4.9 ± 0.6, 2.78 ± 0.11
2M 2139+0220		8.2 ± 1.9, 2.10 ± 0.23	11.8 ± 3.1, 1.75 ± 0.11		
2M 2224-0158		7.4 ± 1.2, 2.31 ± 0.10	12.9 ± 2.1, 1.83 ± 0.09		7.1 ± 2.1, 2.31 ± 0.15
2M 2228-4310		10.2 ± 2.4, 2.10 ± 0.22	17.1 ± 3.2, 1.92 ± 0.08		
2M 2237+3922	7.1 ± 1.0, 2.31 ± 0.11	14 ± 4, 1.92 ± 0.18	31 ± 7, 1.52 ± 0.11	7.1 ± 2.3, 2.54 ± 0.31	18 ± 4, 1.92 ± 0.12
2M 2249+3205		4.4 ± 1.1, 2.8 ± 0.7	5.1 ± 1.7, 2.42 ± 0.19		5.3 ± 1.3, 2.5 ± 0.6
2M 2254+3123		7.1 ± 1.8, 2.10 ± 0.14	16.3 ± 2.1, 1.75 ± 0.09		
2M 2255-5713			5.3 ± 1.1, 2.31 ± 0.35		
2M 2325+4251		6.1 ± 1.2, 2.31 ± 0.28	15 ± 4, 1.75 ± 0.09		
2M 2339+1352		10.2 ± 3.0, 2.10 ± 0.28	21 ± 4, 1.75 ± 0.11		
2M 2351-2537			4.3 ± 0.6, 2.92 ± 0.14		
SDSS 0837-0000			3.4 ± 0.8, 2.8 ± 0.7		

NOTE—Median  $5\sigma$  contrast (within the stated separation range) in 4 of 5 calibrators. No entry indicates no significant detection at that separation is possible. Two entries (at tight separations) is caused by a reduction in sensitivity to equal brightness targets and indicates a significant detection is possible *between* the two values. The diffraction limit ( $\lambda/D$ ) is roughly 95 and 147 mas in F110W and F170M, respectively.